TU Delft

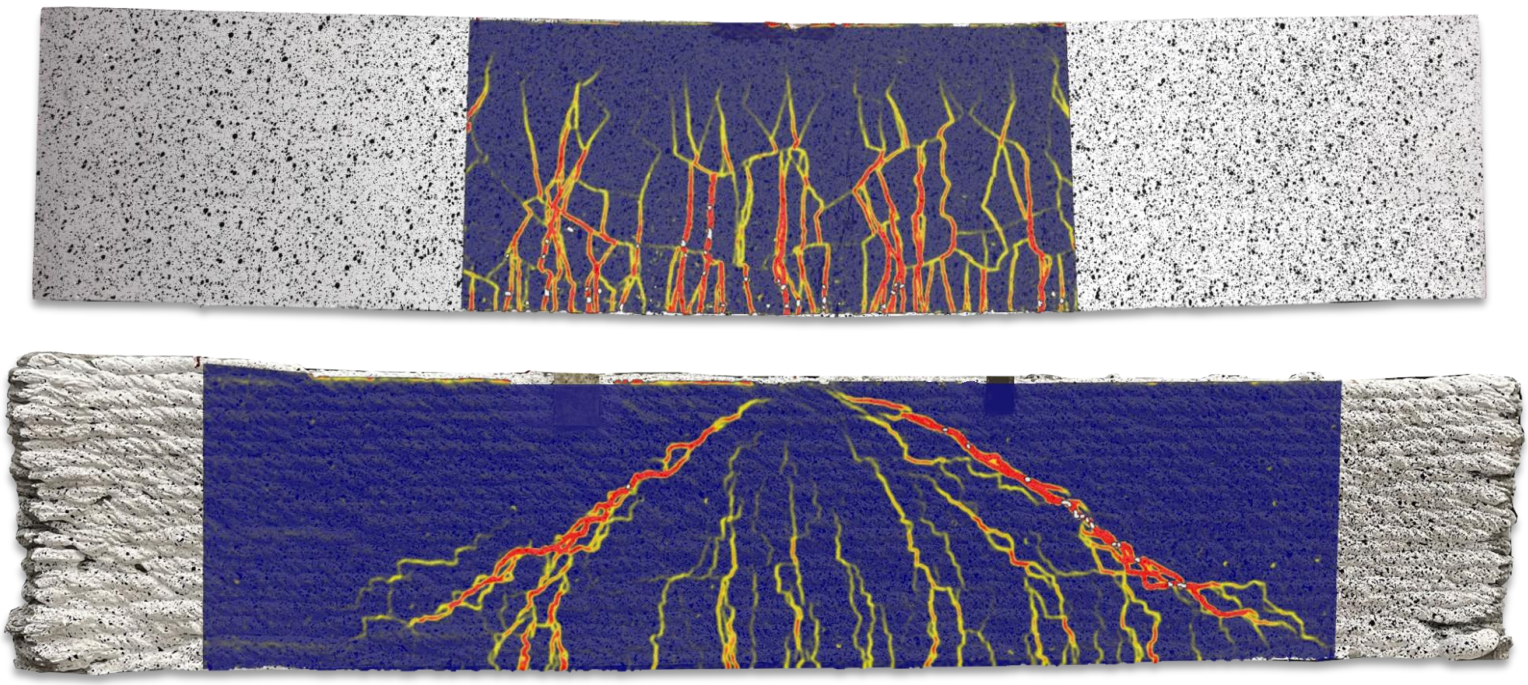

Strain-Hardening Cementitious Composite as Lost Formwork for Reinforced Concrete Beams

S.M. Nuri

Strain-Hardening Cementitious Composite as Lost Formwork for Reinforced Concrete Beams

By

S.M. Nuri

in partial fulfilment of the requirements for the degree of

Master of Science

in Civil Engineering

at the Delft University of Technology,

to be defended publicly on 25-09-23

Thesis committee

Mrs. Dr. Ir. M. Lukovic	(Chair)	Concrete Structures, Tu Delft
Ir. S. He	(Daily supervisor)	Materials and Environment, Tu Delft
Dr. B. Šavija		Materials and Environment, Tu Delft

Acknowledgements

I would like to express my sincere gratitude and appreciation to all those who have contributed to the completion of this thesis. Without their support, guidance, and encouragement, this work would not have been possible.

First and foremost, I would like to thank the chair of my thesis committee, Mladena, for giving me the opportunity to do this research. Mladena's thorough review of my work and constructive suggestions have immensely enriched the quality of this thesis. Also, I want to thank Branko for being part of the committee and sharing his insightful expertise in concrete durability.

I am deeply grateful to my daily supervisor, Shan, for his invaluable guidance, expertise, and unwavering support throughout the whole research journey. I am truly fortunate to have had such a knowledgeable and inspiring mentor.

I am indebted to the faculty of civil engineering and its staff for providing the necessary resources and equipment to facilitate my research. I want to thank Ton for a great time in the lab and his support. I also want to thank Maiko for his assistance in acquiring the materials to conduct this research. In addition, I want to thank the three technicians: Jakob, Albert and Fred for their help with using the equipment in the lab.

I want to thank Yitao and Shozab for sharing their expertise on experimental research and their support during the experiments. Special thanks to Yu, for helping me use the 3D printer.

I am deeply appreciative of my colleagues and friends who have supported me throughout this journey. Their encouragement, discussions, and exchange of ideas have been invaluable in shaping my understanding and approach to the subject matter. Special thanks go to Bartosz, Jurre, Amir and Firas for their support and interesting discussions.

I would like to express my heartfelt gratitude to my family for their unwavering love, encouragement, and understanding. Their belief in my abilities and their unwavering support have been a constant source of motivation. I am forever grateful for their sacrifices and for always being there for me.

I am deeply grateful to everyone who has played a part, no matter how big or small, in the completion of this thesis. Your support, guidance, and encouragement have been instrumental in this achievement, and I am truly honoured and humbled by your contributions.

Thank you all.

Masi Nuri

Abstract

Large cracks in concrete as a result of tensile stresses will lead to corrosion of embedded reinforcing steel, which is the leading cause of deterioration in concrete. It is common to apply additional reinforcement simply to limit the crack width in concrete. Another solution could be to partly replace concrete with other materials. Strain-hardening cementitious composites (SHCC) exhibit ductile behaviour with multiple fine cracks under tension, which possibly makes them suitable to be utilised in combination with traditional concrete. This study aims to investigate the flexural behaviour of SHCC-RC hybrid beams and shear behaviour of SHCC-RC hybrid beams without transverse reinforcement. This includes the load bearing capacity, cracking pattern, crack width control and post-cracking shear ductility.

The SHCC-RC hybrid beams consist of a SHCC U-shaped lost formwork with low quality concrete cast inside. The possibility of 3D printing the stay-in-place formwork is also investigated. Two types of experiments were conducted to study the structural response of the SHCC-RC hybrid members: a four-point bending test for the flexural behaviour and a three-point bending test for the shear behaviour. The cracking pattern and crack width are evaluated with digital image correlation (DIC). The measurements of the DIC are verified with linear variable differential transformers (LVDTs).

Four specimens were tested in bending: a control beam, a hybrid beam with a transverse profiled interface, a hybrid beam with a transverse and longitudinal profiled interface and a hybrid beam with a 3D printed SHCC formwork. The experimental results of the bending test show that the SHCC-RC hybrid beams have a significantly higher bending capacity compared to the control beam. The control beam reached a capacity of 98.3 kN, whilst the hybrid beam with a transverse profiled interface, the hybrid beam with a transverse and longitudinal profiled interface and the hybrid beam with a printed SHCC lost formwork have a capacity of 145.1 kN, 159.1 kN and 152.4 kN, respectively. The interfacial properties between the SHCC and concrete were strong enough to prevent complete delamination of the SHCC formwork. Additionally, the hybrid beams show better crack width control. The hybrid beam with a precast SHCC U-shaped formwork with and without longitudinal profiled interface exceeded the maximum crack width of 0.3 mm at 85.9% and 86.3% of the capacity, after yielding of the reinforcing steel, respectively. In case of a printed SHCC formwork, the maximum crack width exceeded 0.3 mm at 78.1% of the capacity. For the control beam this happened at 49% of the capacity, way before the yield point of the reinforcement.

Furthermore, four specimens without transverse reinforcement were tested in shear: a control beam, a hybrid beam with a transverse profiled interface, a hybrid beam with a transverse and longitudinal profiled interface and a hybrid beam with a 3D printed SHCC formwork. The experimental results of the shear test indicate that a stay-in-place formwork can slightly improve the shear capacity of a RC beam. The control beam and the hybrid beam with a transverse profiled interface have a capacity of 103.7 kN, whilst the hybrid beam with a transverse and longitudinal profiled interface has a capacity of 113.5 kN. The composite beam with a printed SHCC lost formwork reached a capacity of 124.5 kN, probably as a result of the unintended larger SHCC formwork thickness. All the hybrid beams exhibited a larger energy absorption capacity and superior post-cracking shear ductility compared to the control beam. The energy absorption capacity of the hybrid beam without a longitudinal profiled interface, with a longitudinal profiled interface and 3D printed formwork was 26.7%, 106.5% and 160.5%, respectively.

Two models were adopted and used to predict the capacity of the beams in bending and shear. The bending capacity of the control beam could be predicted accurately with the multi-layer model (MLM), but not the midspan deflection at peak load. The experimental load was overestimated by 4.0%. The failure load of the hybrid beam was underestimated by 17.0%. The shear capacity could be predicted accurately with a strut-and-tie model, despite the fact that the interfacial properties of the SHCC-concrete interface were not considered in the model. The failure load of the control beam was overestimated by 3.0% and the failure load of the hybrid beam was overestimated by 6.7%.

In conclusion, a SHCC U-shaped lost formwork is an effective measure to improve the bending as well as the shear response of a RC beam. Casting an U-shaped formwork will be a challenge, but 3D printing can solve this issue. However, the effect of 3D-printed SHCC as formwork on the structural response of a hybrid beam is not well understood yet. In addition, the effect of interface conditions on the structural response was not investigated, whilst literature shows that interfacial properties have a huge impact on the effectiveness of SHCC-RC hybrid structures. It will be recommended to further investigate how material properties, 3D-printing, interfacial properties, formwork thickness, beam size and reinforcement layout affect the structural response of SHCC-RC hybrid beams.

Contents

List of figures

List of tables

Symbols

General symbols	
$\bar{s}_{cr}$	Average crack spacing
h_c	Height inner concrete
A_{sl}	Longitudinal reinforcement area
A_{sw}	Shear reinforcement area
$E_{c,s}$	Concrete stabilized secant modulus of elasticity
E_c	Concrete elastic modulus
E_{cm}	Mean concrete elastic modulus
E_s	Steel elastic modulus
$F_{0.3}$	Load corresponding to maximum crack width of 0.3 mm
F_a	Upper bound force
F_b	Bending resistance
F_{b1}	Lower bound force
F_c	Compressive force in diagonal strut
F_{cal}	Predicted ultimate load
F_{exp}	Experimental ultimate load
F_{max}	Peak load
F_p	Preload force
F_s	Reinforcing steel tensile force
F_{shcc}	SHCC tensile force
F_w	Shear resistance
$M_{cr,c}$	Concrete cracking moment
M_r	Bending moment resistance
M_y	Bending moment at yielding of reinforcing steel
N_c	Concrete compressive force
N_{shcc}	SHCC compressive force
T_s	Tie force
$V_{d,max}$	Maximum dowel force
V_e	Shear force midspan
V_n	Ultimate shear capacity
V_{rc}	Characteristic concrete shear resistance
V_{rkc}	Concrete characteristic shear resistance
V_{rks}	Reinforcing steel characteristic shear resistance
V_{rmax}	Maximum concrete shear resistance
a_v	Shear span

b_c	Width inner concrete
b_w	Total beam width
c_c	Concrete cover
c_t	Total cover
f_1	Principal compressive stress at bottom nodal zone
f_2	Principal tensile stress at bottom nodal zone
f_{ht}	SHCC contribution to tensile capacity
f_c	Concrete strength
f_c	Compressive capacity of the diagonal strut
f_c'	Concrete compressive strength
f_{ce}	Effective concrete compressive strength
$f_{ck,cube}$	Concrete characteristic cube compressive strength
f_{ck}	Concrete characteristic cylinder compressive strength
f_{cm}	Concrete mean cylinder compressive strength
f_{ct}	Tensile strength of cracked concrete
$f_{ctm,fl}$	Mean concrete flexural tensile strength
$f_{s,u}$	Reinforcing steel ultimate tensile strength
$f_{s,y}$	Reinforcing steel yield strength
$f_{shcc,e}$	SHCC effective compressive strength
$f_{shcc,k}$	SHCC characteristic cylinder compressive strength
$f_{shcc,m}$	SHCC mean cylinder compressive strength
$f_{shcc,t}$	SHCC tensile strength
$f_{shcc,tu}$	SHCC ultimate tensile strength
f_{shcc}'	SHCC compressive strength
f_{sl}	Longitudinal reinforcement contribution to tensile capacity
f_t	Tensile capacity of the diagonal strut
l_b	Width loading and support plate
n_{cr}	Number of cracks within constant moment region at peak load
$s_{w,max}$	Maximum shear reinforcement spacing
s_w	Shear reinforcement spacing
t_f	SHCC flange thickness
t_w	SHCC web thickness
u_{max}	Midspan deflection at peak load
w_b	Width compressive diagonal strut
w_t	Width tie
$w_{t,max}$	Maximum width tie
x_u	Concrete compressive zone height

x_u	Height compression zone at maximum flexural capacity
h	Height beam
CW	Maximum crack width at peak load
W	Moment of resistance
d	Effective height cross section
k	Size effect factor
l	Total beam length
n	Number of longitudinal bars
z	Lever arm
Greek letters	
α	Concrete resultant compressive force coefficient
α_{shcc}	SHCC resultant compressive force coefficient
β	Compression zone coefficient
$\varepsilon_{c,1}$	Concrete compressive yield strain
$\varepsilon_{c,3}$	Ultimate concrete compressive strain
ε_{cr}	Cracking stress
$\varepsilon_{s,u}$	Reinforcing steel ultimate tensile strain
$\varepsilon_{s,y}$	Reinforcing steel yield strain
ε_s	Reinforcing steel strain
$\varepsilon_{shcc,t}$	SHCC tensile yield strain
$\varepsilon_{shcc,tu}$	SHCC ultimate tensile strain
ε_{tp}	Tensile peak strain
ε_{tu}	Ultimate tensile strain
θ	Shear crack angle
θ_s	Inclined angle compressive diagonal strut
$\emptyset_l$	Longitudinal reinforcement diameter
$\emptyset_{sw}$	Shear reinforcement diameter
ρ_l	Longitudinal reinforcement ratio
σ_{cr}	Cracking stress
σ_s	Reinforcing steel stress
σ_{tp}	Tensile peak stress

List of abbreviations

3DCMP	3D cementitious printing
3DCP	3D concrete printing
3DP-SHCC	3D printable strain-hardening cementitious composites
3DHB	Hybrid beam with 3D printed formwork
3DP-SHGC	3D printable strain-hardening geopolymer composite
3P	Three-point
4P	Four-point
C3P	Concrete mix used in the shear test
C4P	Concrete mix used in the bending test
CB	Control beam
CFRP	Carbon fibre reinforced polymer
DIC	Digital image correlation
DSTM	Direct strut-and-tie model
ECC	Engineered cementitious composites
EPS	Expanded polystyrene
FRP	Fibre reinforced polymer
HBT	Hybrid beam with only transverse shear keys
HBTL	Hybrid beam with transverse and longitudinal shear keys
HCP	Hybrid composite plate
HPMC	Hydroxypropyl methylcellulose
HS-SHCC	High strength strain-hardening cementitious composites
LVDT	Linear variable displacement transducer
MLM	Multi-layer model
PE	Polyethene
PVA	Polyvinyl alcohol
RC	Reinforced concrete
RH	Relative humidity
SF	Silica fume
SHCC	Strain-hardening cementitious composites
SLS	Serviceability limit state
SP	Superplasticizers
ULS	Ultimate limit state
VMA	Viscosity modifying agents
XPS	Extruded polystyrene

1. Introduction

Reinforced concrete (RC) is the mostly used material in the construction industry. RC has many advantages under which the high compressive strength, availability of ingredients, low maintenance and temperature resistance. Concrete alone lacks the ability to withstand tensile stresses. For this reason, steel is introduced inside the concrete in form of bars or mesh to provide sufficient tensile strength. The design of RC structures consists of two fundamental performance criteria. In the ultimate limit state (ULS), a structure is designed to prevent collapse and failure, whilst the serviceability limit state (SLS) refers to the conditions under which a structure is considered functional. An important aspect in SLS for designing concrete structures is crack control. The Eurocode specifies limitations of the maximum allowable crack width for different load combinations and exposure classes [1]. Limiting the allowable crack width in concrete structure benefits the durability of the concrete through preventing deteriorating processes such as corrosion, ingress of chlorides and freeze-thaw cycles. The maximum crack width and crack pattern in concrete structures mainly depend on the thickness of the concrete cover, stresses in the reinforcement, distribution of reinforcement and shape of the rebar. Reinforcement plays an important role in reducing the crack width in the tensile zone of RC structures. However, designing the reinforcement to control the crack width in SLS, generally results in excessive capacity in ULS due to the permittance of large cracks, making such policy uneconomical.

A possible solution is to alter the properties of concrete in order to improve the structural performance and create a favourable crack pattern under tensile loads. Strain-hardening cementitious composites (SHCC) are composites with mechanical properties which offer promising applications in new and existing structures. The presence of well-distributed fibres in SHCC, also known as engineered cementitious composites (ECC) in literature, provides ductile behaviour up to and beyond 3% tensile strain due to the bridging of multiple fine cracks instead of one big crack (Figure 1). SHCC provides better crack width control and improved tensile strain capacity [2] compared to traditional concrete.

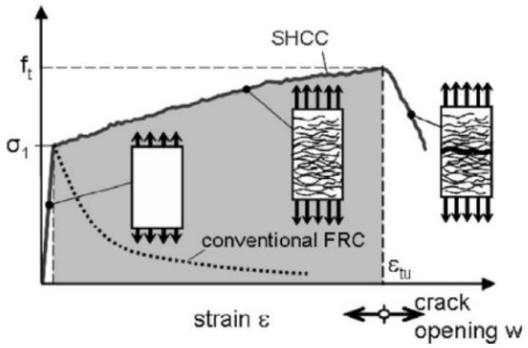

Figure 1. Stress-strain relation of SHCC specimen under monotonic tensile loading [3].

The utilization of SHCC can potentially decrease the required amount of reinforcement for crack width control, thus leading to cost savings. In the past, some studies were carried out to investigate the structural performance of SHCC and their possible application in new and existing RC structures. An example of the first case is an experimental study on the flexural behaviour of composite concrete beams with a layer of SHCC in the tension zone [4]. The composite beams show better cracking behaviour and have a higher bending capacity compared to reference beams consisting of only concrete. The benefits in terms of bending moment capacity and crack control were better for a higher height of the SHCC layer. SHCC can also be used in retrofitting of existing structures. An example is the application of a SHCC overlay on an existing RC beam to improve the structural performance. Wei [5] conducted a study on the shear capacity of reinforced concrete beams strengthened with high strength strain-hardening cementitious composites (HS-SHCC) vertical panels on both sides. The strengthening method successfully enhanced the shear capacity of the RC beams. In addition, the shear failure of the reference beams was accompanied with large diagonal cracks whilst the cracks on the HS-SHCC panels of the strengthened beams were restrained to a fine width.

1.1 Problem statement

Although SHCC seem to be promising, completely replacing concrete with SHCC is not economical due to the high binder content of SHCC. Combining concrete with SHCC may be a more effective and economical way. Most previous studies carried out on SHCC are limited to experimental research, which focus on the strengthening of existing concrete beams with SHCC [6, 7]. The research is usually limited to one specific shape of the overlay with SHCC panels only on the sides. The disadvantage of this wrapping method is that both the SHCC and concrete require a separate mould to be cast, thus increasing casting times and costs. In this regard, SHCC seems to be promising, however integrating SHCC in new reinforced concrete structures may be more beneficial and improve durability, hence reducing maintenance costs [8]. Applying SHCC in advance before casting reinforced concrete, brings forth opportunities to reduce casting times, for instance by creating an U-shaped permanent formwork made of SHCC [9]. The special shape of the SHCC can function as lost formwork for concrete, which reduces the time required to prepare a SHCC-RC hybrid beam. Implementing methods such as 3D concrete printing (3DCP) can result in any formwork being completely redundant [10]. However, there is a lack of knowledge of printable SHCC mixtures and not much experimental research is available on SHCC-RC hybrid beams, especially with an U-shaped permanent formwork.

For this reason, it is of interest to carry out experimental research on SHCC-RC hybrid members with an U-shaped SHCC lost formwork to understand its effects on the cracking behaviour, failure mechanism and load bearing capacity.

1.2 Research objective

The objective of this study is to demonstrate how SHCC and 3D printing can be used to improve the structural response of a SHCC-RC hybrid beam. An experimental study is conducted is to investigate how a SHCC U-shaped lost formwork influences the bending capacity, shear capacity, cracking pattern and crack control of a reinforced concrete beam.

1.3 Research question

The main research question to be answered in this thesis is:

How does a SHCC U-shaped lost formwork in a hybrid SHCC-RC beam influence the flexural and shear behaviour?

The question is divided into multiple sub-questions:

1) What parameters influence the flexural and shear capacity of a hybrid SHCC-RC beam?
2) How will the beams be manufactured and tested?
3) How to make a printable SHCC mixture?

1.4 Scope of research

In this thesis, an experimental study is carried out on SHCC-RC hybrid beams with an SHCC U-shaped lost formwork. The reference and hybrid beams are tested in an experimental study to investigate their structural behaviour in flexure and shear. The reinforcing steel is fully embedded in the concrete. The beam specimens tested in shear do not possess stirrups. Two different fabrication methods are used to create the SHCC formwork: conventional casting and 3D printing. 3D printing is only an extension of the research and not the main focus.

The influence of parameters affecting the flexural and shear behaviour of SHCC-RC hybrid beams, such as the shear span ratio, amount of reinforcement, SHCC-concrete interface conditions and dimensions of the SHCC formwork are not investigated in this research. Furthermore, it is known that the interface conditions between a concrete substrate and SHCC affect the shear properties of the interface, hence affecting the cracking behaviour and failure mechanism of SHCC-retrofitted beams [11] as well as hybrid beams [12]. However, the effect of interfacial properties on the structural response was not examined in this research. All the hybrid beams with a precast U-shaped SHCC formwork have similar interfacial properties, which consists of a profiled interface with circular shear keys.

1.5 Research methodology

This is an experimental-based research. A bending and shear test are carried out on reference beams and hybrid beams to investigate the influence of a precast or 3D printed SHCC U-shaped lost formwork on the structural response, including bending capacity, shear capacity, cracking pattern, crack control and post-cracking shear ductility. To achieve this objective, the research is divided in phases.

To begin with, a literature study is carried out to provide insight in the current knowledge of material properties of SHCC, 3D printable strain-hardening cementitious composites (3DP-SHCC) and structural performance of SHCC-RC hybrid beams, including retrofitted SHCC-RC beams.

Afterwards, a bending and shear experiment are designed to study the flexural and shear behaviour of SHCC-RC hybrid beams. A four-point bending test is designed to analyse the flexural behaviour of a reference beam, two SHCC-RC hybrid beams with a precast SHCC permanent formwork and a SHCC-RC hybrid beam with a 3D printed SHCC permanent formwork. Similarly, a shear test is designed to analyse the shear behaviour of the same beams. In the shear test, the beams are subjected to three-point bending. For both experiments, the longitudinal and transverse reinforcement are designed such that the reference specimens fail in bending in the bending test and fail in shear in the shear test.

At the same time, a suitable and printable SHCC mix design is designed, with small-scale experiments in the lab, including uniaxial tensile tests, uniaxial compressive tests and slump flow tests. The same mix design is used for all the hybrid beam specimens, except some minor adjustments due to the difference in rheology requirement of casting SHCC and printing SHCC.

The beams are fabricated and tested when a suitable SHCC mix composition is found. A bending and shear test are carried out. One control beam, one SHCC-RC hybrid beam with precast SHCC formwork and transverse shear keys, one SHCC-RC hybrid beam with precast SHCC formwork including transverse and longitudinal shear keys, and one SHCC-RC hybrid beam with a 3D printed SHCC formwork will be tested in each test. The height and width of the beams are adopted from a previous study by Huang [13].

In the next step, the crack pattern of the beam specimens are analysed with digital image correlation (DIC). MATLAB is used to calculate the crack width of the cracks in the beams tested in the bending test. The results of the experiments are compared and discussed. The results of the research should provide insight in how SHCC can be effectively used to improve the structural response of reinforced concrete structures.

Finally, two models are implemented to predict the bending and shear capacity of the beams. An analytical model proposed by previous studies [14-16] is implemented to predict the shear carrying capacity of the beams tested in the shear test and a multi-layer model (MLM) [9] is used to predict the capacity of the beams tested in bending.

1.6 Thesis structure

The structure of the thesis is discussed in this section. The thesis paper starts with a literature review in Chapter 2. The design of the experimental programme is discussed in Chapter 3. The material properties and test preparation are mentioned in Chapter 4. The results of all experiments are summarized in Chapter 5. In Chapter 6, the prediction model is discussed which is used to predict the shear capacity. The discussion and conclusion of the research can be found in Chapters 7 and 8, respectively.

2. Literature review

2.1 Strain-hardening cementitious composites

SHCC belong to a class of fibre-reinforced cementitious materials with a microstructure which exhibit pseudo strain-hardening, instead of softening, after the first crack (Figure 2). SHCC are characterized by their ultimate tensile strain which can exceed 4%, keeping the fibre volume content less than 2% [17]. When SHCC are subject to tensile stresses, multiple fine cracks are observed with a crack width less than 100 μm. In the last two decades, a lot of research has been carried out on SHCC. This includes material properties of SHCC [17], prediction models of tensile stress-strain curves [18], flexure and shear properties [19], durability [8] and temperature load effects [20]. Different kinds of fibre types can be employed in SHCC, including steel fibres, polyethene (PE) fibres and polyvinyl alcohol (PVA) fibres. PVA fibres are commonly used to produce SHCC, due to their interface properties and good dispersibility [21]. The interfacial bond strength of PVA is very high, unlike many other common fibre types. It needs to be lowered to produce a composite with strain-hardening behaviour, instead of quasi-brittle. To reduce the bond strength between fibre and matrix, an oil coating is introduced on the surface of the fibres. The fibre type also influences the ultimate tensile capacity of SHCC. It was found that PE fibres are more suitable to produce a high strength and high ductile cementitious composite [22]. Comparatively, the crack widths of SHCC with PE fibres under tension are wider than PVA-based SHCC (with identical fibre volume fraction) [23].

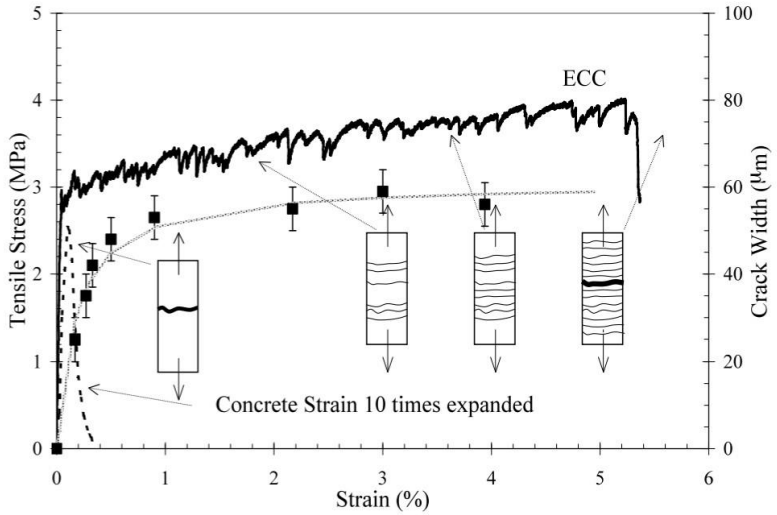

Figure 2. Tensile-strain curve of SHCC [24].

Concerning other matrix ingredients, SHCC are usually composed of fine silica sand with a mean grain size of 110 μm to maintain volume stability and adequate stiffness. The source of the material's ductility in tension comes mainly from three factors: the absence of coarse aggregates, coated fibre reinforcement and mineral admixtures. Coarse aggregates are generally not used in a standard SHCC mixtures, because the presence of relatively large aggregates tends to increase fibre dispersion and fracture toughness. This is not favourable to achieve multiple fine cracks and strain-hardening behaviour when SHCC are subjected to loading [25]. The absence of coarse aggregates requires SHCC mixtures to have a higher cement content than conventional concrete mixtures. To keep the cement content at a minimum for sustainability reasons, adding mineral admixtures, like fly ash, has been reported to bring a lot of benefits [26, 27]. These studies have shown that increasing the content of fly ash in SHCC mixtures improves the tensile ductility. This is attributed to the reduction of the fibre-matrix chemical bond, whilst increasing the interface frictional bond.

2.1.1 Curing and shrinkage

According to a study by Li and Lepech [28], evidence was found that SHCC become more brittle with aging. The results of direct tensile tests showed a decrease in strain capacity of SHCC of approximately

2% between a specimen with a curing age of 10 days and 180 days, due to the hydration process. It was found that after 80 days, the strain capacity reached a steady state.

Wang, et al. [29] studied the shrinkage properties of SHCC-repaired concrete beams. With increasing drying time in an indoor environment, the free shrinkage of SHCC increases due to loss of internal water in the hydration process (autogenous shrinkage) and loss of internal water to the environment (drying shrinkage). The shrinkage value of SHCC is a lot larger than traditional concrete (Figure 3). This can be attributed to the high binder content and lack of coarse aggregates of SHCC. Hence, SHCC have a higher water requirement per cubic volume than concrete. In a concrete beam

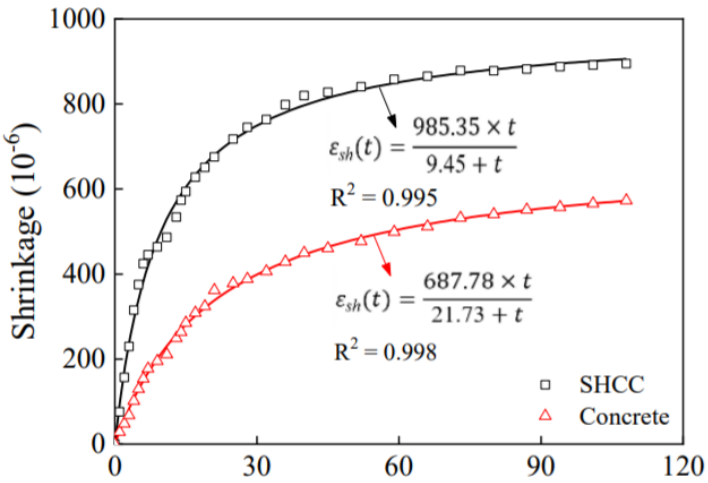

Figure 3. Free shrinkage of concrete and SHCC in an indoor environment (T = 25°, RH = 60%) [29].

with a SHCC repair layer, the free shrinkage of the SHCC overlay is restrained and it will introduce tensile stresses in the repair layer. The repair layer is prone to cracking and interfacial delamination if the tensile stress exceeds the tensile strength of SHCC. Depending on the interface bond strength, different failure modes due to restrained shrinkage can occur (Figure 4).

Figure 4. Failure modes of SHCC-repaired beams due to shrinkage [29].

2.1.2 SHCC-concrete interface

Wang, et al. [29] also studied the influence of interface conditions on the crack pattern and failure mechanism of SHCC-repaired beams due to shrinkage. A total of six repaired specimens with different interface roughness were tested. Three different interface surfaces were compared: smooth, artificial chiselled and groove. The results showed that an artificial chiselled and a groove surface reduce the amount of surface cracks and delamination length due to shrinkage. The effect of the surface roughness on the delamination length seems to be more significant than on the amount of surface cracks and the maximum crack width. In addition, the effect of the repair layer thickness on the delamination length and

crack pattern is examined for a groove surface. The trend is a reduction in delamination length for increasing thickness of the SHCC overlay.

Lukovic [30] compared the crack pattern of old concrete beams with a smooth and groove surface, repaired with SHCC, due to mechanical loading. Due to the relative low bond strength of a smooth SHCC overlay interface, a large debonding length of the repair layer and an uniformly distributed crack pattern was observed. Cracks did not propagate directly into the concrete substrate and remained localised in the substrate due to lack of mechanical interlock. In contrast, the beams with a groove interface showed relative larger localised cracks in the repair layer and a smaller debonding length. Numerical experiments show similar results [31]. The presence of an interface with a low bond strength or roughness results in a longer debonding length, more distributed cracking in the SHCC repair layer, and localised cracking in the concrete substrate. Thus, the bond strength of a SHCC repair layer and concrete has a large impact on the crack pattern of a repaired beam. A low bond strength seems to be favourable due to the presence of a distributed crack pattern over a longer length in the SHCC layer. However, a minimum bond strength is required to fulfil structural integrity and prevent delamination. In the case of differential drying shrinkage, for instance, a low bond strength may result in delamination of the repair layer already before the strain-hardening behaviour of the repair layer can be utilized [32].

Singh [33] studied the influence of interface conditions on the crack control of SHCC-concrete hybrid beams. In the hybrid beam, the concrete in the tensile zone is replaced with SHCC. All beam specimens with varying interface profiles (in the constant moment region) were tested in a four-point bending setup. It was observed that all beam specimens with different interface roughness had a similar load bearing capacity. The results of the four-point bending tests indicated that when the interface property changes, a different cracking pattern is observed. The bond strength of a smooth surface was sufficient to prevent complete delamination. A roughened smooth surface with wire brush also exhibited sufficient bonding and a shorter delamination length compared to a smooth surface, allowing cracks to be redistributed throughout the SHCC layer. However, a few cracks propagated into the concrete substrate due to the roughening. The beam specimen with a profiled interface exhibited an even smaller debonding length of the SHCC layer, due to mechanical interlock. Furthermore, a pronounced monolithic behaviour of the beam specimen was observed with through cracks penetrating the concrete substrate.

2.1.3 Applications SHCC

SHCC have been used in a number of applications in Japan, Korea, Switzerland and USA. For instance, SHCC has been used in the composite deck of a cable-stayed bridge (Figure 5). An estimated of 800 m^3 of SHCC has been used to replace an asphalt overlay on the steel deck with a 38 mm thick SHCC layer to increase the load bearing capacity [34]. However, due to unexpected deterioration which soon followed, the SHCC layer had to be removed [35].

Figure 5. Mihara bridge with SHCC/steel composite deck (Hokkaido, Japan, 2004).

SHCC have also been successfully used on the surface of cracked concrete. A concrete retaining wall in Gifu (Japan) build in the 1970s with a width of 18 m and a height of 5 m, suffered from

alkali-aggregate induced cracks. These cracks were injected with epoxy resin and the concrete surface was coated with an organic material. Few years later, cracks were observed in the surface repair material, so nine years later it was decided to spray SHCC on the wall surface (Figure 6). To study the performance of SHCC, the wall was divided in nine repaired sections and one unrepaired section. In each section a different combination of SHCC, reinforcement and sealing was used. No cracking was observed after seven months. The difference in the crack pattern is clearly visible between sections repaired with SHCC (No.1 - No.8) and normal repair mortar (No.9) (Figure 7). The sections repaired with SHCC did not develop a crack width more than 0.05 and 0.12 mm, 12 and 24 months after repair, respectively. In contrast, a crack width of 0.3 mm was observed 24 months after repair in the section repaired with normal repair mortar. To verify the durability of SHCC, a section of a deteriorated bridge deck in Michigan was repaired using SHCC in 2002 [36]. Other parts of the bridge deck were repaired using conventional concrete patching. After five years it was found that the crack width in the SHCC patched section was limited to 50 µm, whilst the cracks in the conventional repair material widened up to 2 mm.

Figure 6. Surface repair with SHCC of a concrete retaining wall in Gifu [37].

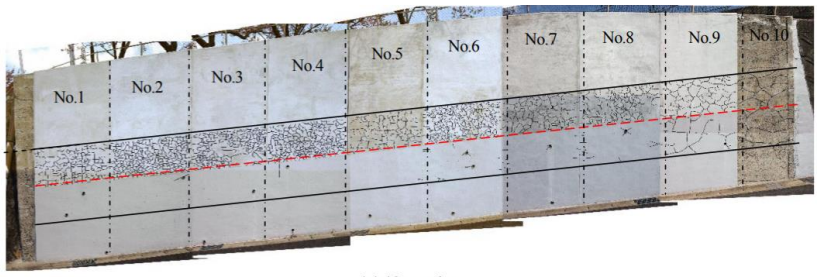

(a) 12 months

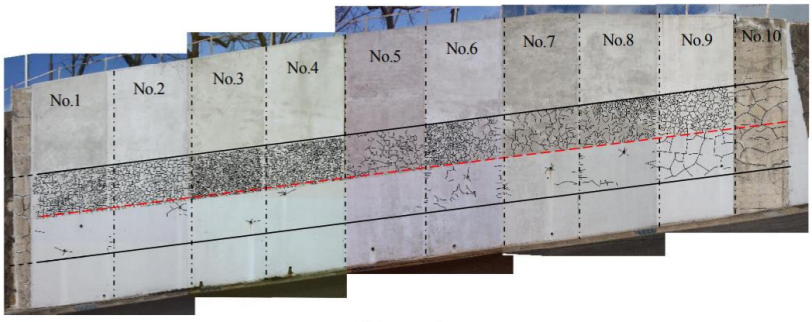

(b) 24 months

Figure 7. Observed crack patterns at 12 and 24 months after repair [37].

2.2 Extrusion-based 3D cementitious printing

Extrusion-based 3D concrete printing (3DCP) is an emerging technology to construct concrete elements without formwork. In 3DCP, fresh concrete is extruded at controlled volumes to deposit layers in sequential manner. The use of 3DCP can provide many benefits in the construction industry. The elimination of formwork reduces the construction time, cost and waste generation which in turn leads to

lower environmental impact [38, 39]. Formwork can amount up to half of the construction costs [40], especially for constructions which require formwork with a complex geometry. However, the binder content of 3D printed cementitious materials is typically higher than conventional cast cementitious mixtures [41]. In general, Portland cement accounts for 15%-45% of the total concrete mix proportion [42]. The production of Portland cement has a large contribution to the global CO_2 emissions (around 8%) [43]. As a result, the usage of binders such as Portland cement may nullify the environmental benefits of 3DCP. Many studies attempted therefore, to develop more sustainable printable cementitious materials using extrusion-based methods, for instance by substituting the natural aggregate by recycled aggregates [44] or adopting a more sustainable binder, such as geopolymer [45, 46]. Using cementitious materials instead of concrete for 3D printing is referred to as 3D cementitious printing (3DCMP).

A typical extrusion-based 3DCP and 3DCMP process consists of four stages: mixing, pumping, extrusion and building. Each stage in the process demands different rheological properties of the fresh material. Extrusion and pumping processes demand a low yield strength and viscosity, whilst during building, the extruded fresh material should exhibit a high yield strength to sustain the load from subsequent layers [47]. Conventional cementitious mixtures do not meet the rheological requirements for 3D printing, hence the fresh state properties of cementitious materials need to be optimized to become printable. Some of the important rheological parameters to characterize the fresh-state behaviour and printability of a cement-based mix are *flowability, pumpability, extrudability* and *buildability* [48].

2.2.1 Flowability

Printable cementitious materials require a high flowability during printing to be pumpable. Common methods to measure the flowability of cementitious materials are the slump test, V-tunnel test and L-box test [49]. The slump flow test is probably the most appropriate test to assess the flowability of a mixture [50]. According to Tay, et al. [51], cementitious mixtures tested according to ASTM C1437-15 [52] with a slump value between 4 and 8 mm, and a slump flow between 150 and 190 mm showed desired properties for extrusion-based 3DCMP.

2.2.2 Pumpability

The pumpability of a cementitious mixture refers to ease with which fresh cementitious material is delivered from the pump to the printhead [53]. Many problems can occur during the pumping process, such as particle segregation, bleeding and blockage of the hose. The pumpability of a mix design with suitable pumping rate can be determined with a pumpability test. However, a standard test protocol for evaluating the pumpability of cementitious materials is not available. Many researchers use trial-based methods to assess the pumpability of their material and pumping setup [51, 54].

2.2.3 Extrudability

The extrudability of a mixture describes “the ability to continuously print the material through a nozzle with an acceptable printing quality” [50]. The extrudability depends on the mixture’s rheological properties, printer nozzle and extrusion system. A ram extruder (Figure 8) can be used as a tool to assess and examine the extrudability of materials [55]. The fresh mixture is filled in a barrel and afterwards a ram connected to a compression device is pushing the material towards a gradually narrowing die. However, the extrudability of a cementitious mixture should also be assessed in combination with a 3DCMP setup. Many extrudability measurements so far have been qualitative only [56], for instance through visual inspection [57, 58].

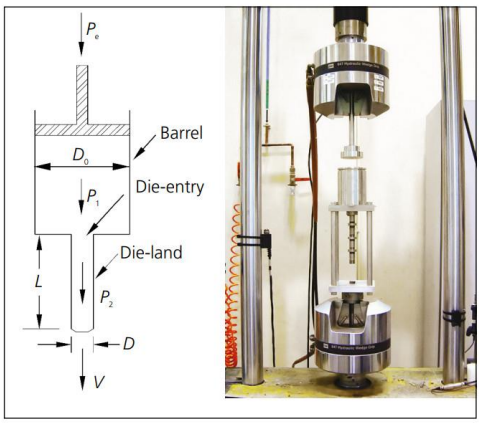

Figure 8. Ram extruder [59].

2.2.4 Buildability

Buildability or shape stability of a mixture describes the capacity to print multiple layers on top of each other. The yield stress is the most important parameter defining the stability of a flowable mixture. It is defined as the stress that must be applied to initiate flow. The yield stress determines the stability, shape and size of the printed filaments. Each filament needs to support the following ones, thus high yield stresses are desired for a printable mixture. A relative easy method to monitor the (static) yield stress is to perform a shear growth test [60], which involves applying a constantly increasing strain whilst monitoring the stress increase. Other examples of test methods to assess the shape stability of printing cementitious materials, are the “layer settlement” test and “cylinder stability” test [57]. In the layer settlement test, two or more filaments are printed on top of each other with a specific time gap between consecutive filaments. After printing all the filaments, the settlement and strain of the filaments are measured and evaluated. Increasing the time gap between successive layers increases the stiffness of the deposited layer and may improve the buildability of cementitious materials, but results in a weaker bond strength between the filaments [61]. Ma and Wang [49] used a layer settlement test containing 20 filaments to assess the stability of cementitious mixtures containing copper tailings. In the cylinder stability test, two cylinders are cast on top of each other (with two semi-cylinder shells) and the resulting deformations of the cylinder due to a specific load are measured.

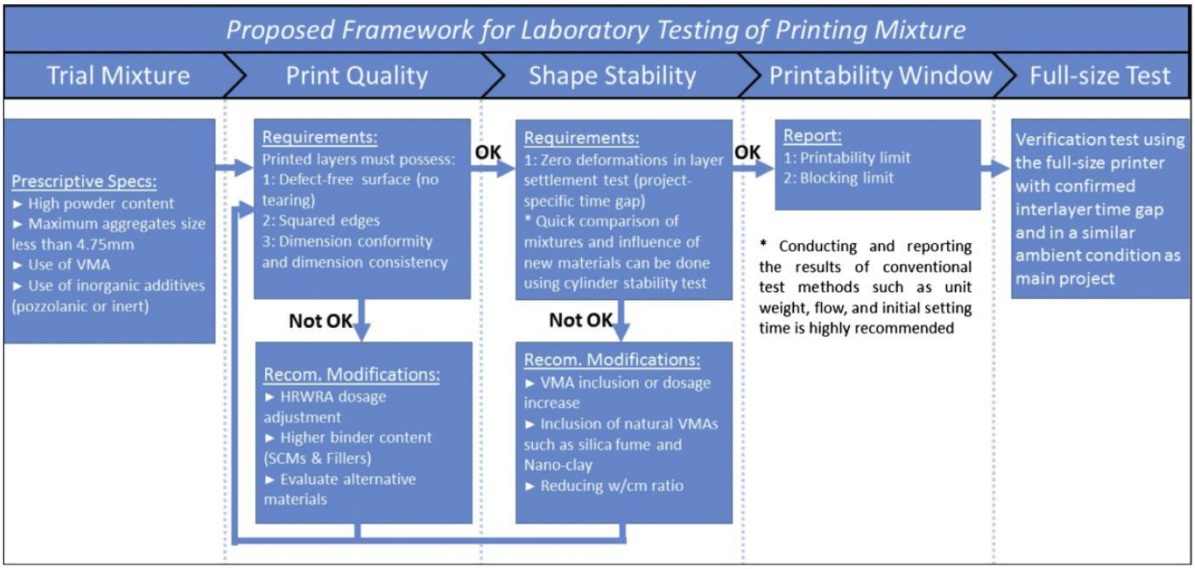

Figure 9. Proposed framework for laboratory testing of printing mixtures in fresh state [57].

There is no general accepted framework to assess the printing quality of 3DCMP. Some studies evaluate the printing quality (at different printing speeds) through visual inspection [45, 58]. Kazemian,

et al. [57] has proposed a framework for performance-based laboratory testing of 3D printed cementitious mixtures (Figure 9). In the framework, the print quality, shape stability and printability window are studied of fresh cementitious printed mixtures. The printability window is defined as the operation window for extrusion of printable cementitious material. The printability window is limited due to cement hydration. The yield stress of cementitious materials increases with time during hydration. Therefore, a printable mixture at the start of the printing process may not be printable anymore after a period of time. This also means that at a predefined printing speed, filaments are extruded at different material ages. Hence, the material properties of the mixture should be assessed at different ages as well in order to determine the printability window. The printability window depends on the rheological properties of the fresh mixture. To improve the rheological properties of fresh cementitious materials, chemical admixtures such as super plasticizers (SP), viscosity modifying agents (VMA) and setting retarders may be introduced in the mixture. Superplasticizers are commonly used in cementitious mixtures to enhance the workability during mixing and casting, making the mixture more fluid. However, SP do not always prevent segregation and bleeding of the cementitious material [62]. The use of VMA is recommended in such cases to increase the cohesion and stability of the cementitious mixture [63]. VMA also enhance the fibre dispersion of strain-hardening cementitious composites [54] and water retention of cement-based mortars [64]. Moreover, the benefits of using VMA in 3DCP and 3DCMP have been acknowledged by many studies [54, 65]. Hydroxypropyl methylcellulose (HPMC) is one of the most used VMA. Furthermore, setting retarders can be used to delay the hydration evolution of cement-based mixtures and increase the open time for printing.

Another chemical admixture used in cementitious materials is silica fume (SF). Silica fume can increase the packing density and improve the cohesion of cementitious material due to its fine particle size. Certain studies showed that the addition of silica fume can increase the yield stress and plastic viscosity [66-68], whereas in other studies the opposite was observed [69, 70]. The difference in results is due to different physical characteristics and volume fraction of silica fume used in the studies [50]. In addition, the influence of silica fume on the rheology is also related to the water to binder ratio and type of SP.

2.2.5 3D-SHCC printing

The use of fibres can bring a lot of benefits to 3D printing of cementitious materials. Most fibres enhance the mechanical properties of a composite mixture. The usage of fibres can also help compensate the relative high shrinkage of 3D printable cementitious materials. However, the challenge of meeting the requirements of pumpability and shape stability are magnified by the introduction of fibres. The findings of many studies on the development of printable SHCC indicate a lack of sufficient stability resulting in premature collapse failure during the printing process [54, 71, 72]. Research on 3D printable strain-hardening cementitious composites (3DP-SHCC) reported an increase in tensile strength and ductility of printed SHCC compared to conventional cast SHCC due to the enhanced fibre alignment during mixing and filament extrusion processes [71, 73], whilst other studies found inferior tensile properties [54, 74].

Felekoglu, et al. [75] investigated the influence of rheological properties on the mechanical performance of SHCC. They concluded that mixtures with a high workability are not ideal for SHCC as they led to a poor fibre distribution. Moreover, Li and Li [76] found that adding VMA to control the viscosity of a SHCC mixture resulted in a good fibre dispersion. From research it has also been reported that the extrusion process has a vital impact on the final fibre dispersion in the filaments. Fibres tend to orientate in the longitudinal direction of the filament, however it seems that reality is more complex [77]. Highly flexible fibres seem to orientate diagonally in a V-shape behind the nozzle [78].

2.2.6 Printing parameters

There are certain printing parameters affecting the printability of cementitious materials, besides the mix composition. It includes the nozzle travelling speed, nozzle shape and size, material extrusion rate and nozzle standoff distance, i.e., the height of the nozzle above the upper surface of the previous layer [53]. These parameters have a substantial impact on the stability and print quality. To give an example, the flow rate of extruded material should be synchronized with the movement of the nozzle to prevent discontinuity in printed filaments [79]. Furthermore, research suggest that proper choice of nozzle standoff distance can relieve the problem of insufficient interface bonding [80]. Reducing the standoff distance to approximately the filament thickness reduces the occurrence of large voids at the interface and causes more horizontal fibre alignment which brings about excellent in-plane tensile characteristics [81]. A greater nozzle standoff distance generally leads to stronger inter-layer bonding ,which is related

to the amount of fibres bridging adjacent layers, at the expense of significant cross-sectional deformation due to the expansion of contact area of adjacent layers [74].

2.3 Structural behaviour of SHCC

The strengthening of existing reinforced concrete beams is not a new concept. For instance researchers have tried to investigate the use of fibre reinforced polymers (FRP) to strengthen reinforced structures [82]. The FRP layer can be applied in different configurations: complete wrap, U-wrap or side wrap (Figure 10). This method has become popular due to the advantages of FRP composites, such as high corrosion resistance and flexibility in the forming process. Nevertheless, deficiencies correlated to the resin-based adhesives as bonding agent made the FRP strengthening method vulnerable to environmental exposure [83] and wet/dry cycles [84]. The benefits of using SHCC in strengthening RC beams was noticed and promoted further research on utilising SHCC in retrofitting applications.

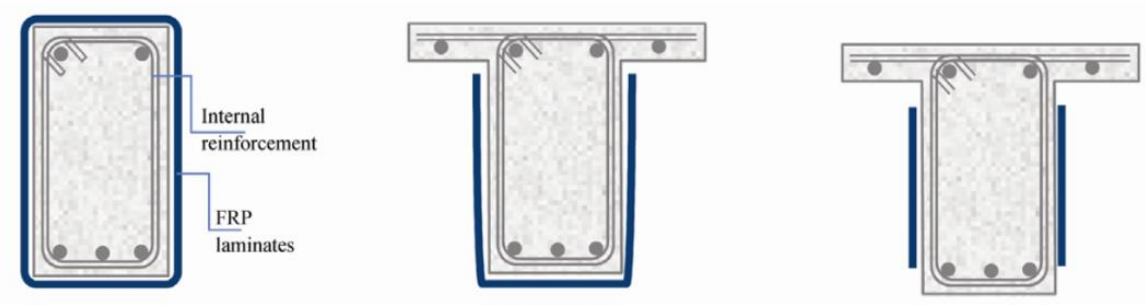

Figure 10. Wrapping configurations of FRP laminates: complete wrapping (a), U-wrap (b) and side wrap (c) [85].

2.3.1 SHCC-RC retrofitted beams

An experimental investigation is conducted into the advantage of a strengthened RC member without transverse reinforcement using SHCC panels [7]. Four specimens were prepared, two of which were strengthened with SHCC with a thickness of 5 mm (SHCC-5) and 10 mm (SHCC-10), and two reference beams: a concrete and SHCC beam. All specimens were subjected to a three-point bending test to measure displacements and evaluate the crack pattern (Figure 11). The difference in crack pattern between the SHCC member and strengthened RC beam was clearly visible. The amount of multiple fine cracks in the strengthened situation decreased significantly and both SHCC-5 and SHCC-10 showed a similar localised diagonal crack (Figure 12). This observation indicated a reduction in ductility of the SHCC strengthening layer compared to a full SHCC member [86]. The shear load capacity of the RC member was notably increased with increasing thickness of the SHCC layer (Figure 13a). The shear contribution of the SHCC panels could be determined analytically fairly accurately (Figure 13b).

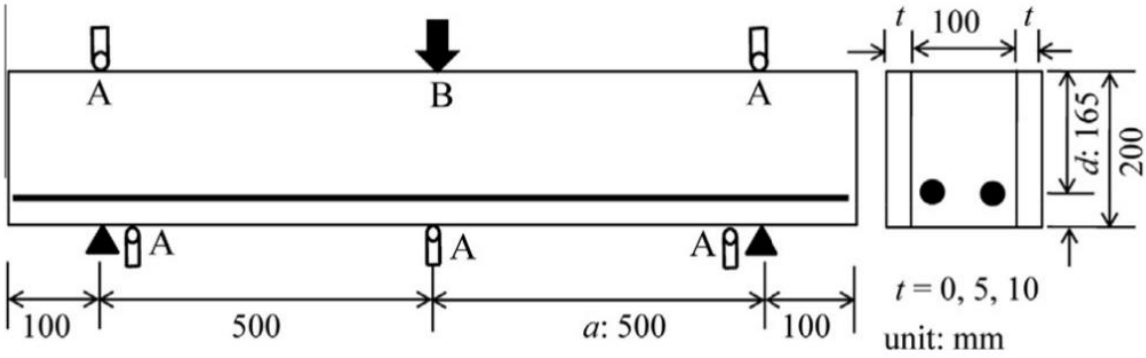

Figure 11. Experimental setup of strengthened concrete beam with SHCC [7].

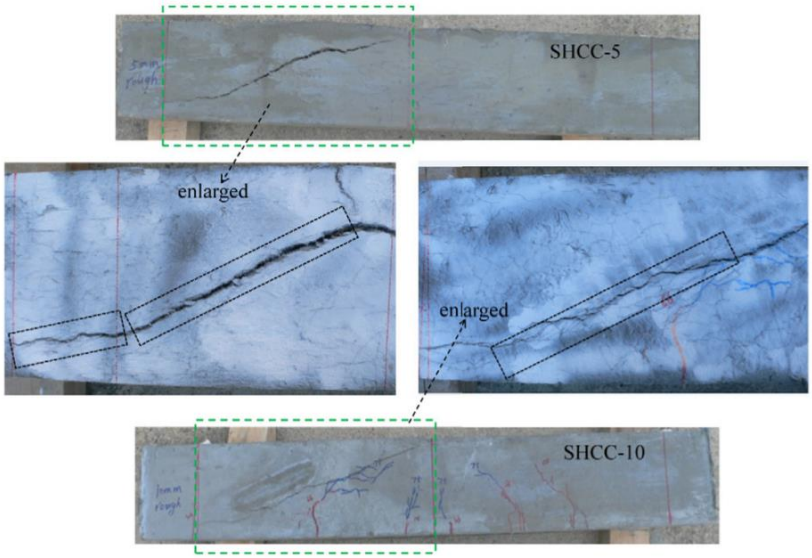

Figure 12. Cracking behaviour of SHCC-5 and SHCC-10 [7].

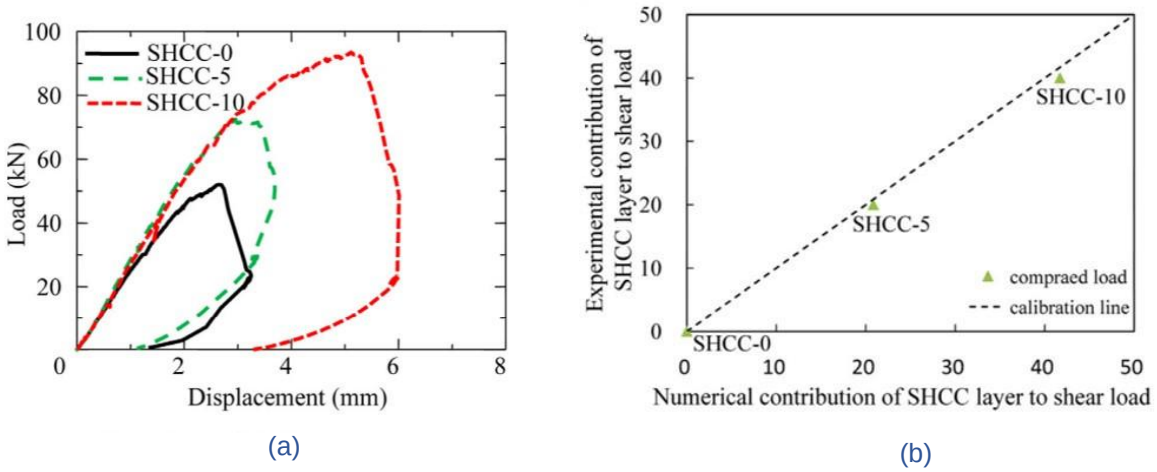

Figure 13. Shear load displacement curve with varying thickness (a) and comparison of experimental and analytical calculated shear contribution of SHCC (b) [7].

Similar studies also considered the effect of reinforcement and shear span ratio on the strengthening treatment with SHCC. Wang, et al. [6] evaluated the shear behaviour of RC beams externally strengthened with a SHCC layer thickness of 20 mm and 40 mm. A series of four-point bending tests were conducted to analyse the load response and failure mode. Two different longitudinal reinforcement ratios (ρ_l = 0.89; 2.18%) and two shear span-to-depth ratios (a_v/d = 2; 3) were used. In general, it was concluded that RC beams with a side SHCC jacket is an effective measure to increase the shear bearing capacity. The research indicates that a strengthening layer with a higher thickness does not necessarily result in a higher ultimate load. The increment of the shear bearing capacity was not sensitive to the increment of the SHCC thickness for specimens with a_v/d = 3. The results also indicate that side strengthening was more effective for specimens with ρ_l = 2.18%. All strengthened specimens showed shear failure, accompanied with more distributed and narrow cracks compared to the control specimens. The failure mode for specimens strengthened with 20 mm SHCC layer was either tensile rupture (ρ_l = 0.89%, a_v/d = 3) or debonding of the SHCC layer (ρ_l = 0.89%, a_v/d = 2; ρ_l = 2.18%, a_v/d = 3). For specimen strengthened with 40 mm SHCC layer, the typical failure was debonding of the strengthening layer.

2.3.2 SHCC-concrete composite beams

Several studies have been carried out to study the structural performance of (reinforced) concrete beams with a permanent formwork made of SHCC. Li, et al. [87] utilised precast PVA-SHCC panels as permanent formwork for concrete beams to evaluate their performance on crack dispersion. Seven hybrid beams with flat panels (400 x 100 x 100 mm) with different top surface conditions and three beams with U-shaped formwork with different inner surface forms were investigated (Figure 14). Small SHCC-concrete composite beams were cast and tested mechanically in four-point bending. The test results showed that using precast SHCC panels as permanent formwork can significantly improve the load capacity and toughness of a RC beam. The peak load of a concrete member increased between 63% and 93%, and the mid span deflection at the critical failure load became 5.35 to 23.40 times larger when a PVA-SHCC permanent formwork was introduced, depending on the shape and surface condition.

Four different failure modes could be identified in the experiments (Figure 15). The concrete beam had one major crack up to final failure (Figure 15a). Six out of the seven composite beams with a flat SHCC panel exhibited a ductile failure mode which is typical for a perfect interface bond (Figure 15b), including the SHCC panel with a smooth interface. A single main crack in the concrete dispersed into multiple fine cracks in the SHCC. The remaining composite beam with a flat SHCC panel had a ductile failure mode accompanied with a partially debonding zone, longer cracking zone in SHCC and larger ultimate deflections (Figure 15c). It appears that some debonding between the SHCC and concrete can provide high improvement in ductility. The failure mode of the three composite beams with an U-shaped panel corresponds to strain-hardening behaviour, with the formation of many fine vertical cracks along the whole constant moment region (Figure 15d). The width of the cracks was controlled over the full depth of the beam.

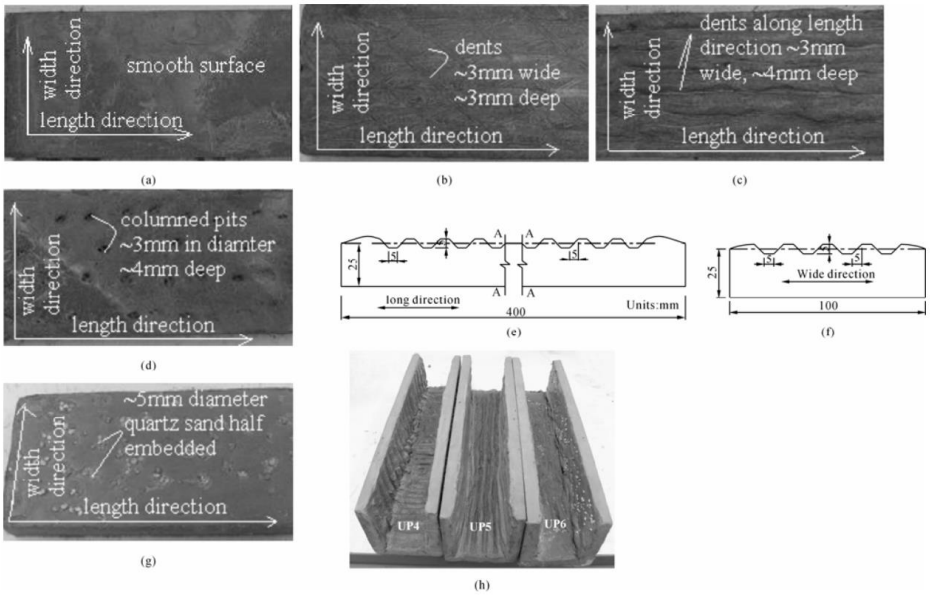

Figure 14. Schematic illustration on surface conditions of PVA-SHCC panels [87].

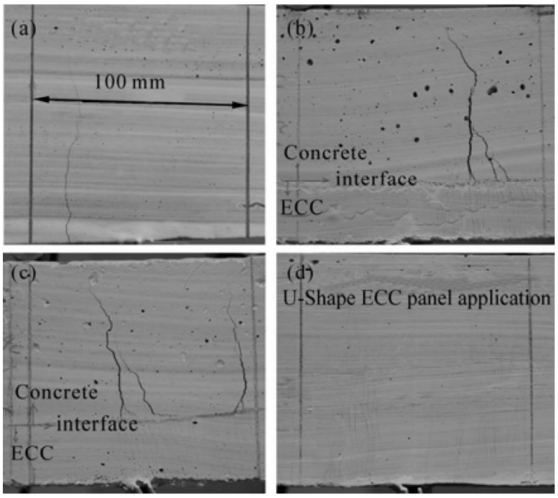

Figure 15. Cracking modes of SHCC-concrete composite beams [87].

Qiao, et al. [88] investigated the flexural performance of SHCC-RC composite beams with a SHCC U-shaped permanent formwork. The U-shaped formwork was cast in two steps. The two side plates are prepared first with embedded L-shaped reinforcement at intervals (Figure 16a). To study the bond properties of the SHCC-concrete interface, different surface treatments were used on the SHCC bottom plate surface before initial setting: a smooth surface (N), surface with grooves (T) and surface with partially embedded sand particles (S) (Figure 16b). The thickness of the bottom plate is larger than the side plates (Figure 17).

A total of eight beam specimens (2 RC beams, 2xN, 2xT, 2xS) were subjected to four-point bending with a span of 1200 mm and a constant bending moment region of 400 mm. All the composite specimens behaved ductile and exhibited flexural failure, instead of debonding failure before crushing of the concrete. One of the RC beams failed in combined flexural-shear. This indicates that a SHCC U-shaped formwork can improve the shear strength of RC members due to the fibres bridging cracks. In the load-deflection curve of the composite beams, a softening behaviour was observed due to debonding between SHCC and concrete, especially after peak load. Although debonding resulted in

(a) (b)

Figure 16. Fabrication of SHCC U-shaped permanent formwork; before casting the bottom plate (a) and after demoulding (b) [88].

loss of load, all composite beams failed by localization of flexural cracks rather than debonding cracks. Eventually, all the composite beams failed by crushing of the concrete. The improvement in ductility and load-carrying capacity of the composite beams was limited compared to the RC beams, since they were bounded by the ultimate compressive strain of concrete. Additionally, the contribution of SHCC in the tension zone to the flexural capacity is relatively low when the longitudinal reinforcement ratio (1.5%) is high. The RC beam had a load bearing capacity of 75.7 kN (73.8), whilst the hybrid beams with grooves had the highest capacity of 87.2 kN (82.9 kN).

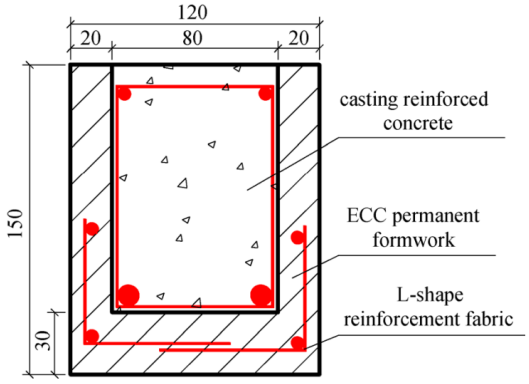

Figure 17. Cross section SHCC-RC composite beams [88].

The surface condition of the SHCC U-shaped formwork had hardly any influence on the peak load, but it did have an influence on the ductility of the composite beams. The composite beam with transverse grooves had the largest ultimate midspan deflection and hence, the best performance in terms of ductility due to the relatively good interfacial bond between SHCC and concrete. Moreover, the crack width of the SHCC did not exceed 100 μm when the applied load was 80% or lower than the peak load. This aspect of SHCC-RC composite beams is very beneficial when considering durability.

Leung and Cao [89] investigated the flexural performance of small-scale concrete beams with a span of 300 mm and cross section of 100x100 mm constructed utilising PVA-SHCC as a precast U-shaped permanent formwork with different surface treatment. The results indicated that composite beams with transverse grooves exhibited a higher flexural capacity compared to a smooth surface (Figure 18).

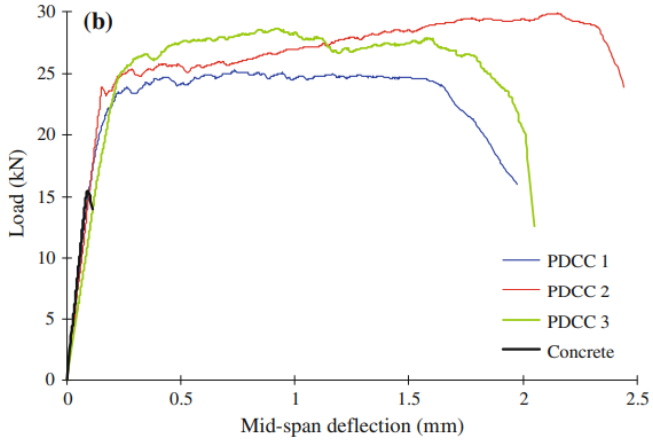

Figure 18. Load-deflection response of small-scale hybrid beams with SHCC U-shaped formwork and different surface treatment [89].

Zhang, et al. [12] investigated the shear behaviour of RC slender beams without shear reinforcement with a precast U-shaped SHCC permanent formwork by conducting a four-point bending test with a span of 1300 mm. The beams had fixed height of 200 mm and fixed width of 150 mm. SHCC formwork with different thicknesses, that is, 15, 20 and 25 mm, were cast. With each thickness, three different interface conditions: smooth, anchored and rugged, were prepared to investigate the influence of interfacial properties on the shear behaviour and failure mechanism. The U-shaped SHCC permanent formwork were cast using an external steel formwork and inner foamed cuboid (Figure 19). After casting the SHCC formwork, the inner foamed cuboid was demolished. By changing the surface of the foamed cuboid, different interface conditions were realized (Figure 20).

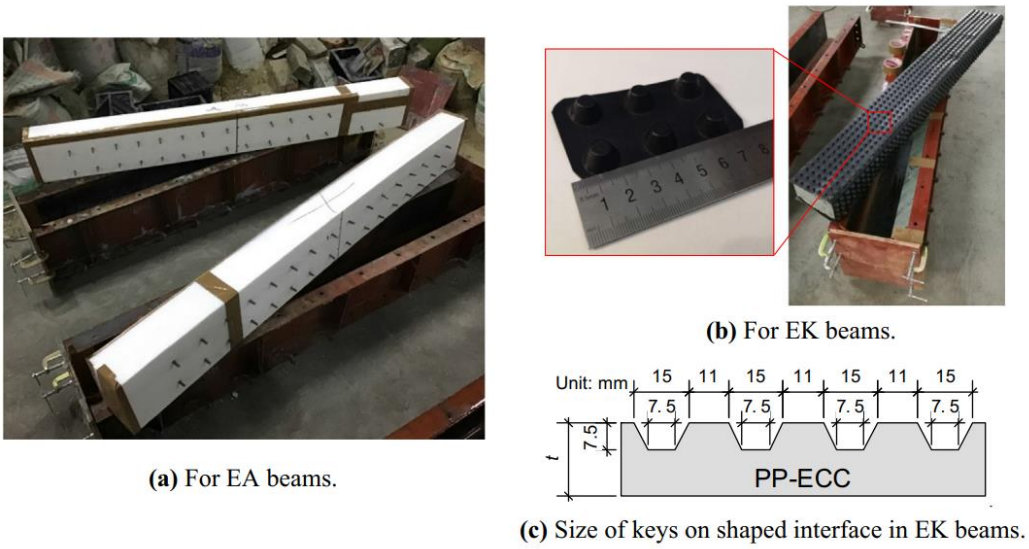

Figure 19. Prepared inner formwork to cast U-shaped SHCC formwork with different interface conditions [12].

(a) (b) (c)

Figure 20. Precast U-shaped SHCC permanent formwork with different surface treatment: smooth (a), anchored (b) and keys (c) [3, 12].

Four-point bending tests were carried out to analyse the shear capacity and cracking behaviour of the reference and composite beams. The results showed that the composite beams with a formwork thickness of 20 mm exhibited the highest shear capacity (Figure 22). The interface with the uniformly shaped keys displayed the strongest interfacial bond. The interface condition showed low correlation to the absolute shear capacity, but a strong interface resulted in a low variation of shear capacities (Figure 22a) and low variation of deformation capacities (Figure 22b) for different values of the SHCC formwork thickness.

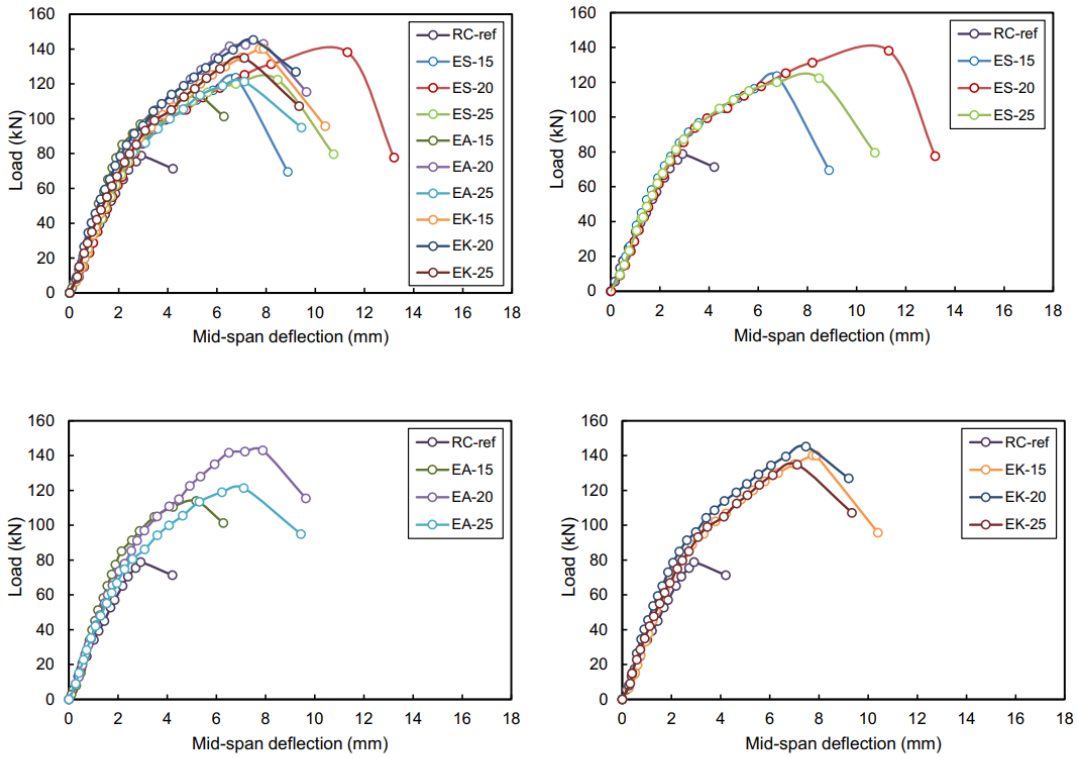

Figure 21. Load vs. midspan deflection [12].

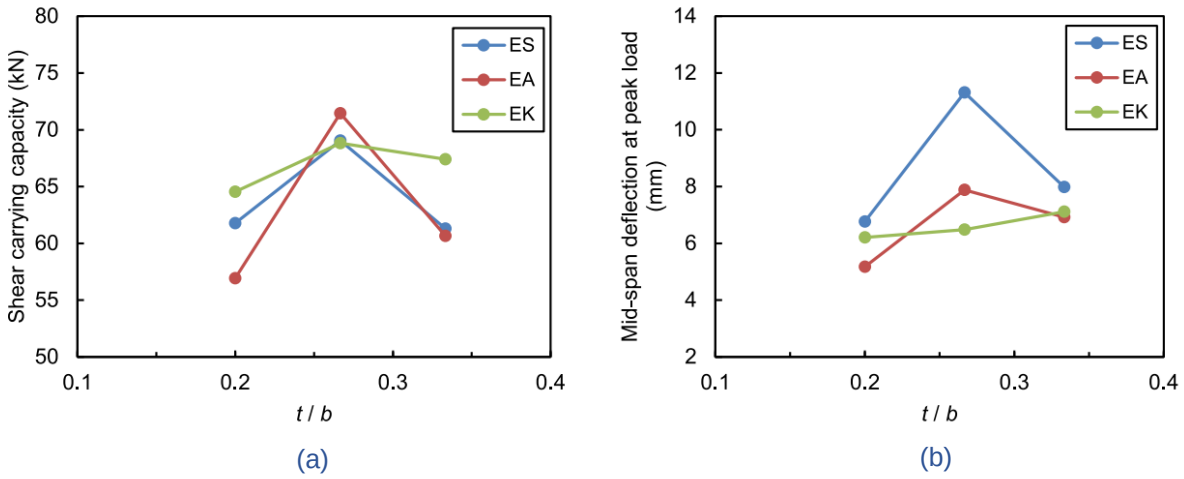

Figure 22. Influence of thickness of U-shaped permanent formwork on shear capacity and mid-span deflection [12].

Bong, et al. [10] investigated the performance of RC beams constructed using permanent formwork made of 3D printable strain-hardening geopolymer composite (3DP-SHGC). The environmental footprint of 3DP-SHGC is significantly lower than of 3DP-SHCC, because the binder consists of geopolymers. Utilising geopolymers, such as fly ash or blast-furnace slag can reduce carbon emissions of cementitious mixtures by as much as 80% [90]. In the study, two permanent formwork systems were manufactured with different printing strategies for the soffit (tension zone): printing in lateral direction and in length direction (Figure 23), to investigate the influence of printing strategy on the flexural performance of the RC beam with 3DP-SHGC formwork. The flexural performance was evaluated by conducting four-point bending tests. The results were compared with a conventionally mould-cast RC beam (control beam). The strain-hardening behaviour introduced through the

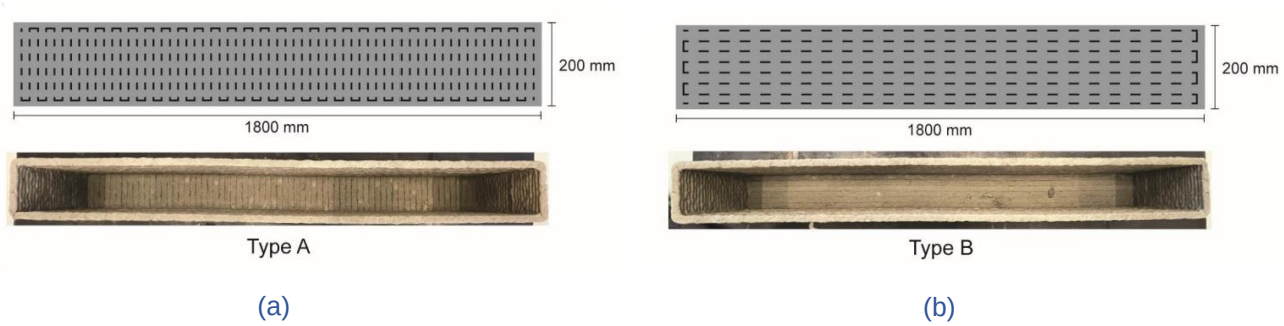

Figure 23. Printing patterns for the soffit of 3DP-SHGC permanent formwork: lateral (a) and longitudinal (b) [10].

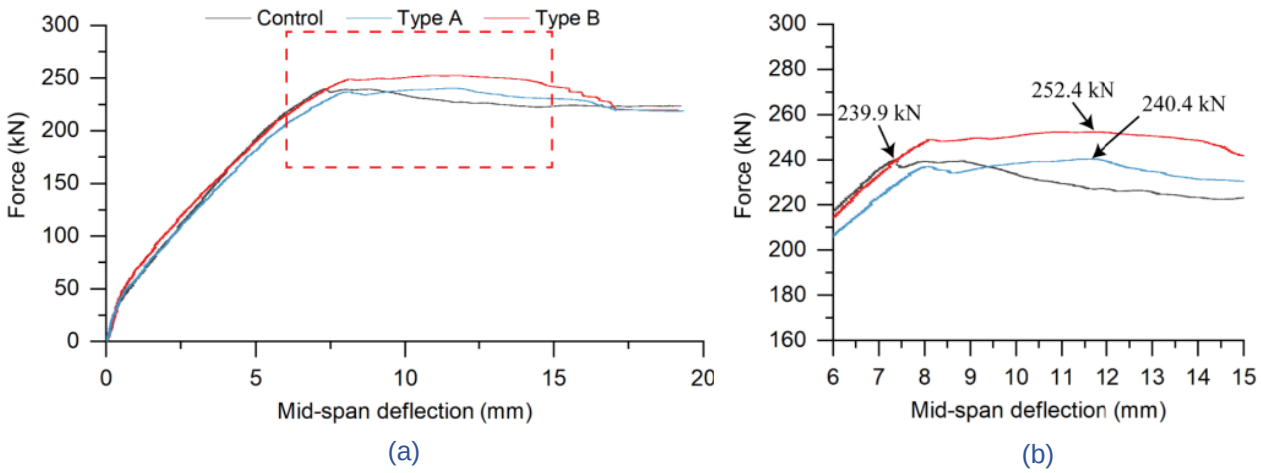

Figure 24. Force-displacement curve of control and hybrid beams (a), and enlargement of red rectangle (b) [10].

3DP-SHGC permanent formwork is visible in the force-displacement curve (Figure 24). The RC beams produced with 3DP-SHGC formwork exhibited superior flexural performance. Type A and Type B beams had a higher cracking load (up to 43%) and mid-span deflection at ultimate load (up to 60%). However, the ultimate load capacity of the hybrid beams was not much higher than of the control beam. In addition, it was found that the printing strategy at the soffit of the permanent formwork had a significant influence on the flexural performance of the hybrid beam. For beam Type A, the cracking initiated at the interface of the printed filaments and was accompanied by multiple fine cracks. In beam Type B, a number of fine cracks were observed in the tension region which propagated towards the concrete compression zone as the deflection increased.

3. Design of the experiments

A bending and shear test were designed according to the Eurocode [1]. A four-point (4P) bending test (Figure 25) is used to study the flexural behaviour of the beam specimens whilst the shear behaviour is analysed in a three-point (3P) bending test (Figure 26). A total of eight beam specimens with a cross section of 200 x 150 mm are tested. For each of the two experiments, a control beam (CB), two hybrid beams with a precast U-shaped SHCC formwork: one with only transverse shear keys (HBT) and one with transverse as well as longitudinal shear keys (HBTL), and a hybrid beam with a printed SHCC formwork (3DHB) were tested. The designation of the beams is displayed in Table 1. The control beam consists of only concrete. The experiments are designed to promote flexural failure of the control beam in the 4P bending test and shear failure of the control beam in the 3P bending test. Stirrups are only applied in the 4P bending test.

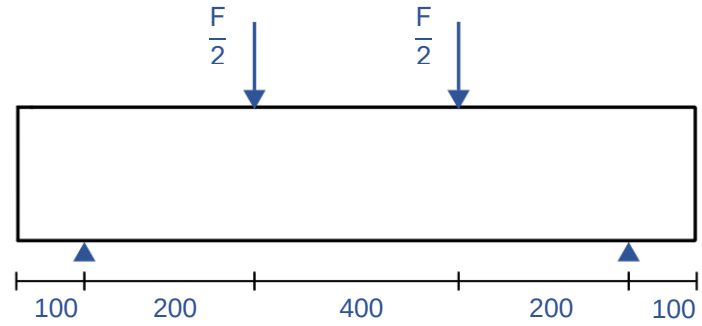

Figure 25. Dimensions four-point bending test.

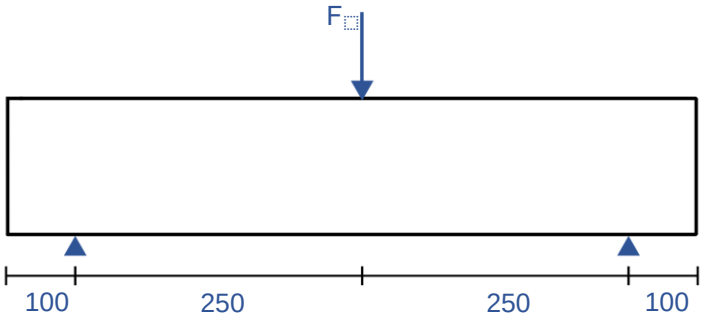

Figure 26. Dimensions three-point bending test.

Bending	l (mm)	h (mm)	b (mm)	$\emptyset_l$ (mm)	$\emptyset_{sw}$ (mm)
CB1	800	200	150	2x8	2x8
HBT1					
HBTL1					
3DHB1					
Shear	l (mm)	h (mm)	b (mm)	$\emptyset_l$ (mm)	$\emptyset_{sw}$ (mm)
CB2	800	200	150	2x12	-
HBT2					
HBTL2					
3DHB2					

Table 1. Tested beam specimens.

3.1 SHCC mix design

To be able to print SHCC, a proper mix design is required. Generally, SHCC are optimized in terms of mechanical properties such as the tensile strain capacity. However, 3D printing of SHCC poses extra conditions on the rheology of the material. Thus, in this thesis the SHCC will be optimized regarding its printability. The goal is to obtain a mix composition of SHCC with the right fresh properties in terms of flowability, pumpability, extrudability and buildability. Small-scale tests, such as slump flow tests, uniaxial tensile tests and compressive tests are conducted on several SHCC mixtures with different mix compositions to evaluate the fresh and mechanical material properties.

3.2 Beam cross section

The material properties are shown in Table 2. In the design of the beam cross section, the following assumptions are made:

- A bi-linear stress-strain relationship is assumed for concrete (Figure 27a).
- Linear strain-hardening behaviour of steel is incorporated in the stress-strain curve of reinforcing steel (Figure 27b).
- Partial material safety factors for all materials in ULS are neglected.

The objective of the experiments is to investigate the influence of a SHCC U-shaped permanent formwork on the flexural and shear behaviour of a hybrid beam. This includes the load bearing capacity, failure mechanism, crack width and crack pattern. To reach this objective, some boundary conditions are set for the experiments to make the results comparable as much as possible.

1) Two reinforcement cages are designed, one for the 4P bending test and one for the 3P bending test.
2) The same mix design for concrete is used in all experiments.
3) All beams should have the same dimensions.

The experiments are designed with analytical calculations performed in Maple. The background and details of the calculation are summarized in Appendix A. Some of the important intermediate results are displayed in this section. With manual iteration, a suitable diameter of the longitudinal $\emptyset_l$ and shear reinforcement $\emptyset_{sw}$ was determined. The elastic modulus of concrete is determined with an analytical expression from the Eurocode [1].

Concrete			Reinforcing steel		
f_{ck}	30	MPa	$f_{s,y}$	550	MPa
f_{cm}	38	MPa	$f_{s,u}$	600	MPa
$f_{ctm,fl}$	4.06	MPa	E_s	200	GPa
$\varepsilon_{c,1}$	1.75	‰	$\varepsilon_{s,y}$	0.275	%
$\varepsilon_{c,3}$	3.50	‰	$\varepsilon_{s,u}$	5	%

Table 2. Material properties used for the design of the experiments.

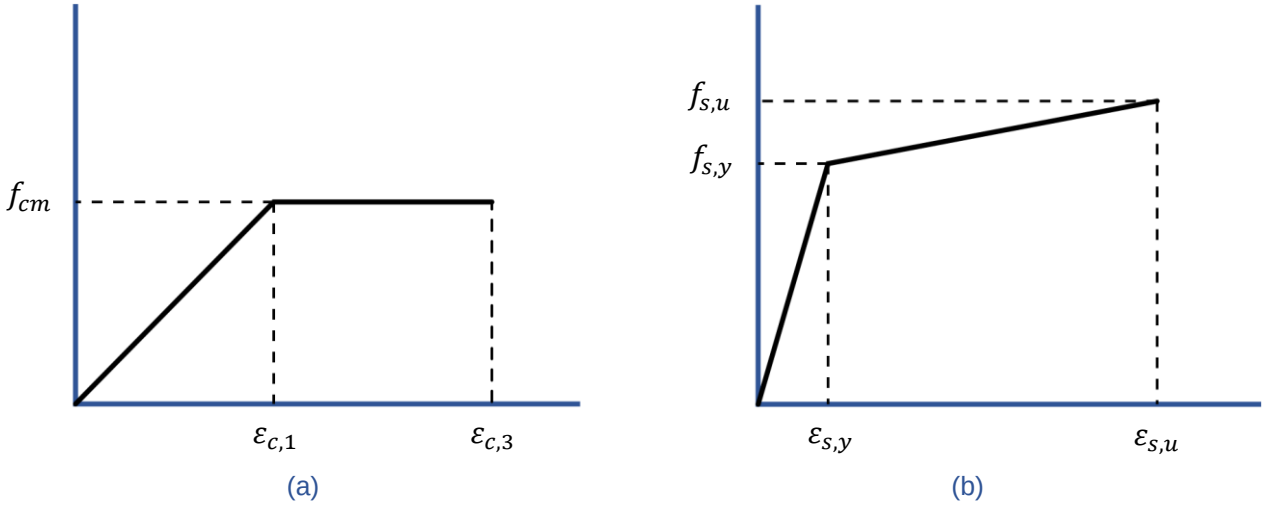

Figure 27. Stress-strain curves of concrete in compression (a) and reinforcing steel (b).

3.2.1 Bending test

The reinforcement layout used in the 4P bending test is designed to prevent shear failure and promote flexural failure in the control beam (Figure 28). The bending resistance and shear resistance of the control beam are determined with the input parameters mentioned in the previous section.

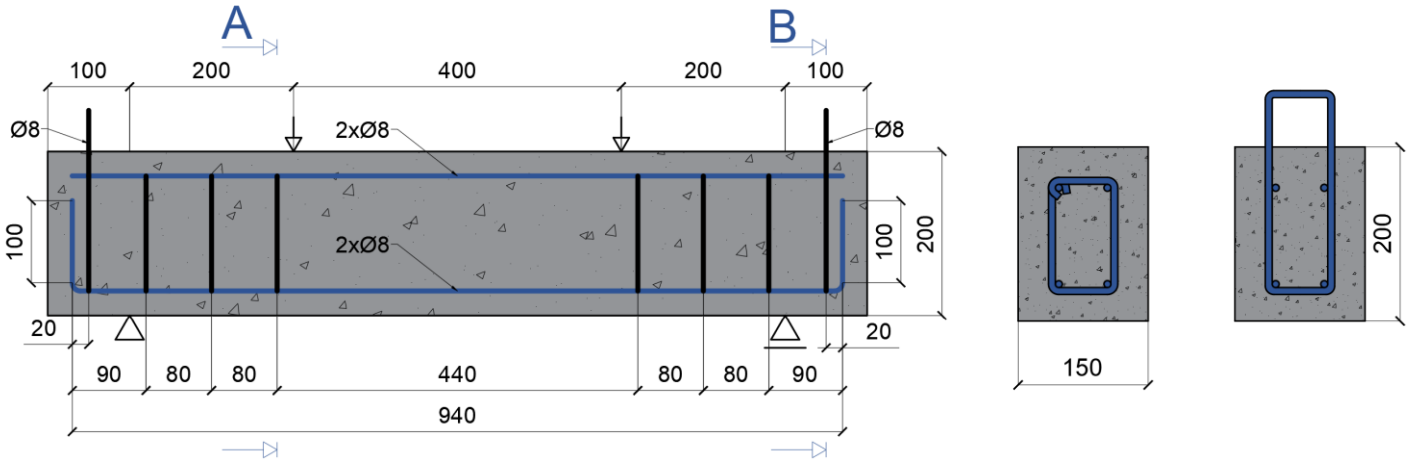

Figure 28. Reinforcement layout in the 4P bending test.

Control beam (CB1)					
Bending resistance			Shear resistance		
d	158	mm	V_e	45.0	kN
x_u	13.8	mm	k	2	-
α	0.75	-	ρ_l	0.43	%
β	0.38	-	V_{rkc}	19.9	kN
N_c	58.9	kN	θ	45	°
F_s	58.9	kN	z	152.6	mm
A_{sl}	100.5	mm^2/m	V_{rmax}	206.1	kN
σ_s	585.9	N/mm^2	$s_{w,max}$	170.7	mm
W	1x10^6	mm^3	s_w	80	mm
$M_{cr,c}$	4.1	kNm	F_w	191.8	kN
M_y	8.5	kNm			
z	152.6	mm			
M_r	9.0	kNm			
F_b	89.9	kN			

Table 3. Calculation of the bending and shear resistance for the 4P bending test.

The control beam is designed to fail in bending at a load F_b of 89.9 kN (Table 3). The shear resistance of the beam needs to be sufficient to permit failure in flexure. Therefore, the characteristic value of the shear resistance should be higher than the occurring shear force V_e when the load is equal to F_b. Shear reinforcement is required as the occurring shear force is lower than the characteristic shear strength of concrete: $V_e > V_{rkc}$. In that case, it is assumed that only the shear reinforcement contributes to the shear capacity, according to the Eurocode [1]. It was calculated that the spacing of the stirrups s_w can have a maximum value of 170.7 mm (Table 3), assuming two-legged stirrups with a diameter $\emptyset_{sw}$ of 8 mm.

The shear reinforcement needs to be placed within both shear spans a_v of the beam, which is 200 mm. Thus, it is opted to use a spacing s_w of 80 mm, so a total of 6 double-legged stirrups are placed in all the beams for the 4P bending test (Figure 28). The characteristic shear resistance F_w becomes 191.8 kN, which is sufficient to prevent shear failure of the control beam. At the ends of the beams in the unloaded zone, double-legged stirrups are protruding from the top of the beam to facilitate the displacement of the beams with a crane. The position of the reinforcement in the cross section is the same for all four beams (Figure 29 until Figure 32). The final experimental setup is displayed in Figure 47.

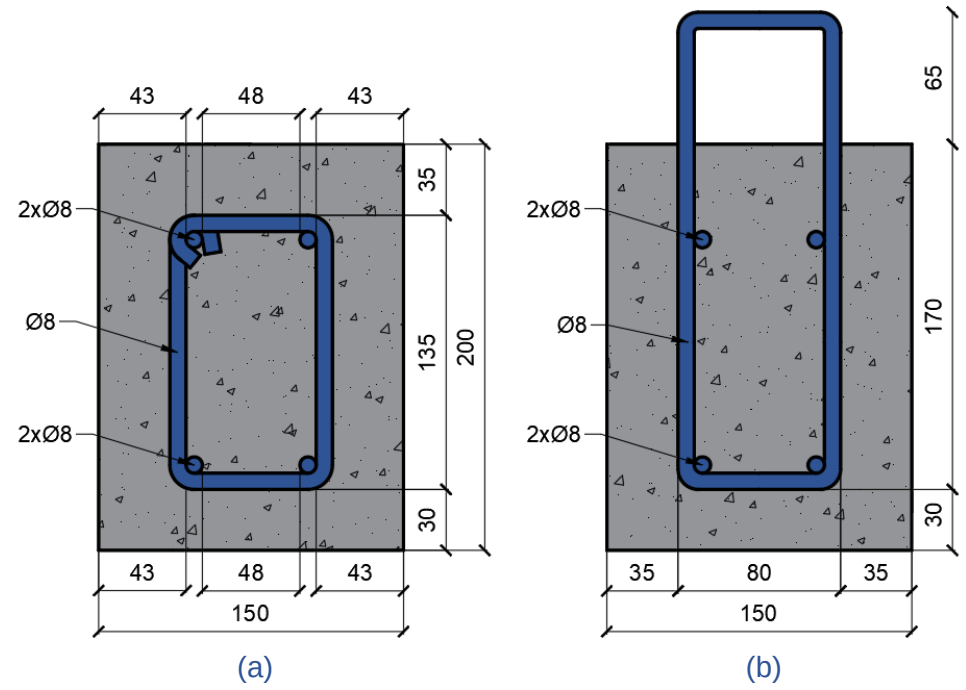

Figure 29. Cross section A (a) and B (b) of CB1.

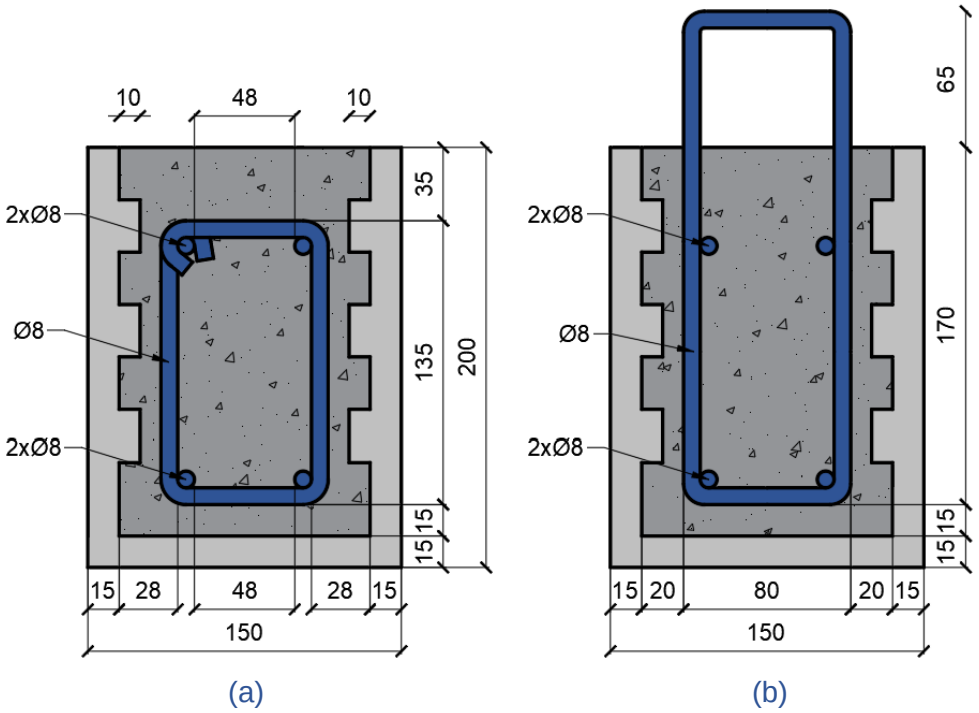

Figure 30. Cross section A (a) and B (b) of HBT1.

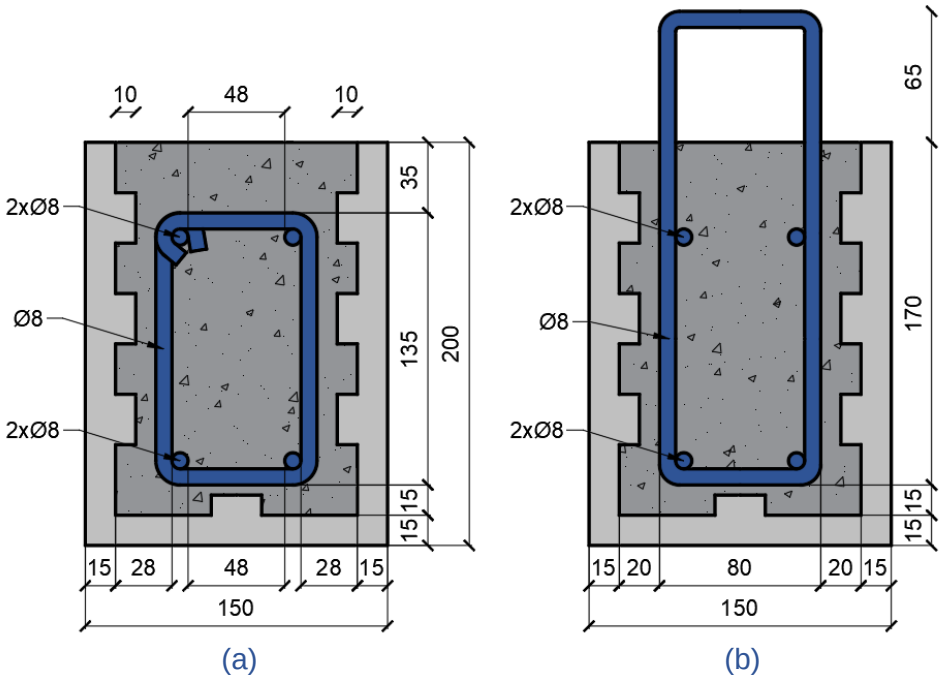

Figure 31. Cross section A (a) and B (b) of HBTL1.

Figure 32. Cross section of 3DHB1/3DHB2.

3.2.2 Shear test

The reinforcement layout for the shear test is designed to prevent flexural failure and promote shear failure (Figure 33). The input parameters for the calculations can be found in the same tables as for the 4P bending test (Table 2).

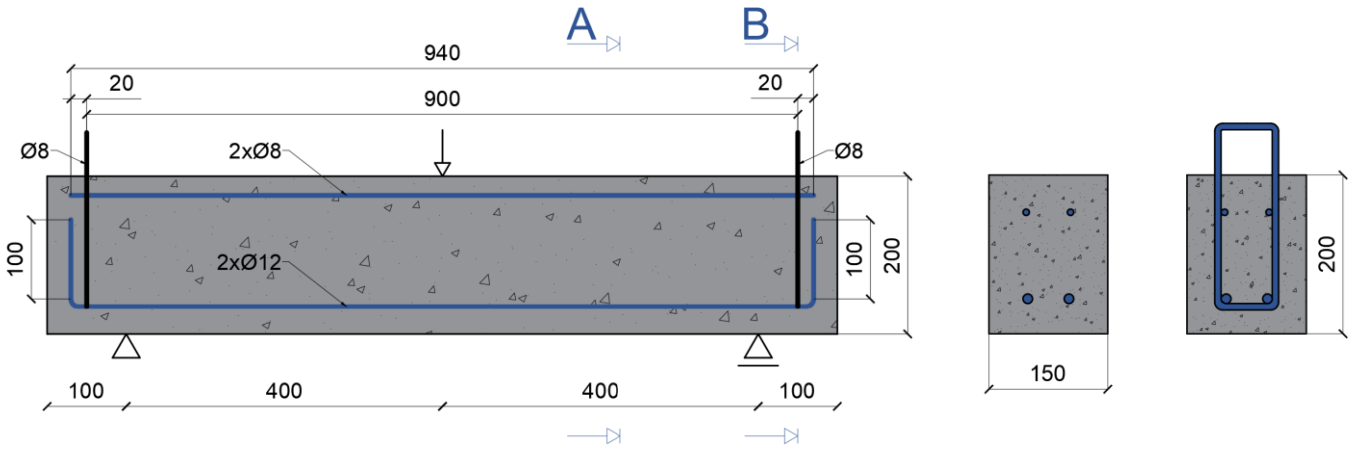

Figure 33. Reinforcement layout used in the shear test.

Control beam (CB2)					
Bending resistance			Shear resistance		
d	156	mm	V_e	46.0	kN
x_u	29.8	mm	k	2	-
α	0.75	-	ρ_l	1.0	%
β	0.39	-	V_{rc}	25.9	kN
N_c	127.3	kN	F_w	51.7	kN
F_s	127.3	kN	F_b/F_w	1.78	
A_{sl}	226.2	mm^2/m			
σ_s	563.0	N/mm^2			
W	1x10^6	mm^3			
$M_{cr,c}$	4.1	kNm			
M_y	18.0	kNm			
z	144.4	mm			
M_r	18.4	kNm			
F_b	92.0	kN			

Table 4. Calculation of the bending and shear resistance for the 3P bending test.

To prevent flexural failure and promote shear failure in the shear test, the bending resistance F_b and shear resistance F_w are determined. The bending resistance F_b of the control beam is 92.0 kN (Table 4). Shear failure occurs if the shear capacity of the beam is lower than the bending capacity. Since the occurring shear force at a load of F_b in the 3P bending setup is more than the shear strength of concrete: $V_e > V_{rc}$, the condition for shear failure is satisfied when no shear reinforcement is applied. For this reason, it was opted to not apply stirrups. The ratio between F_b and F_w is taken sufficiently large to ensure shear failure in the control beam.

Two protruding two-legged stirrups are added at the ends of the beams to facilitate displacement of the beams. The position of the reinforcement in the cross section is the same for all four beams tested in the 3P test (Figure 34 until Figure 36). The final experimental setup is displayed in Figure 50.

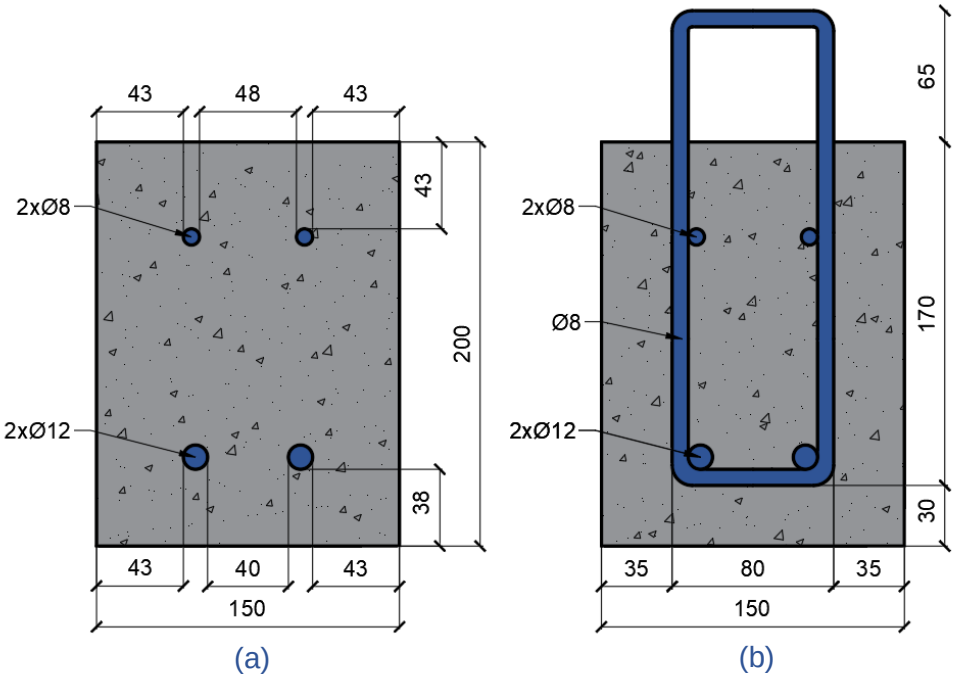

Figure 34. Cross section A (a) and B (b) of CB2.

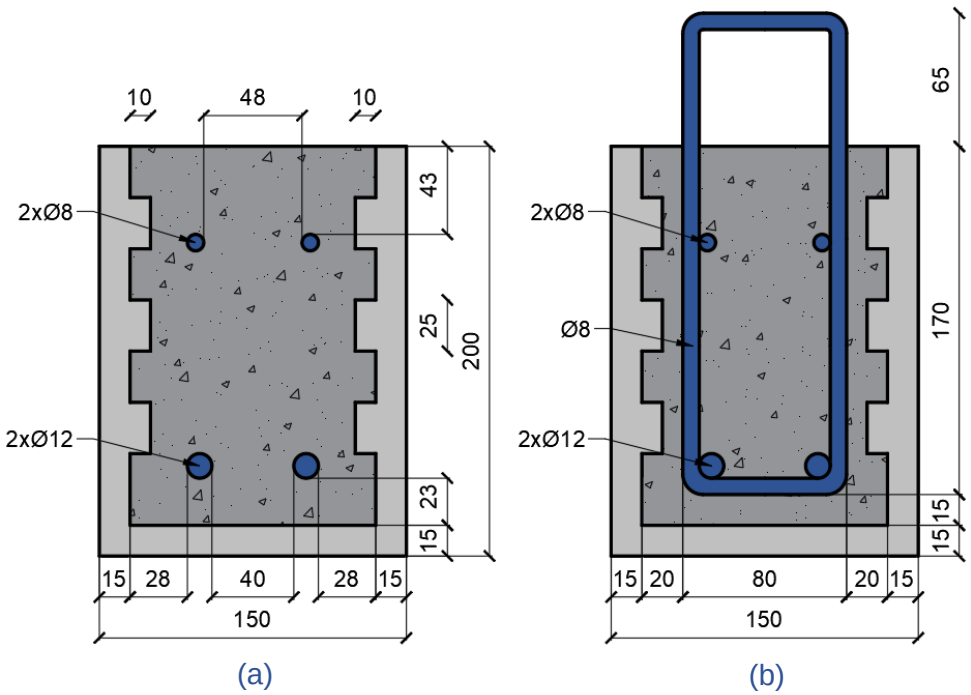

Figure 35. Cross section A (a) and B (b) of HBT2.

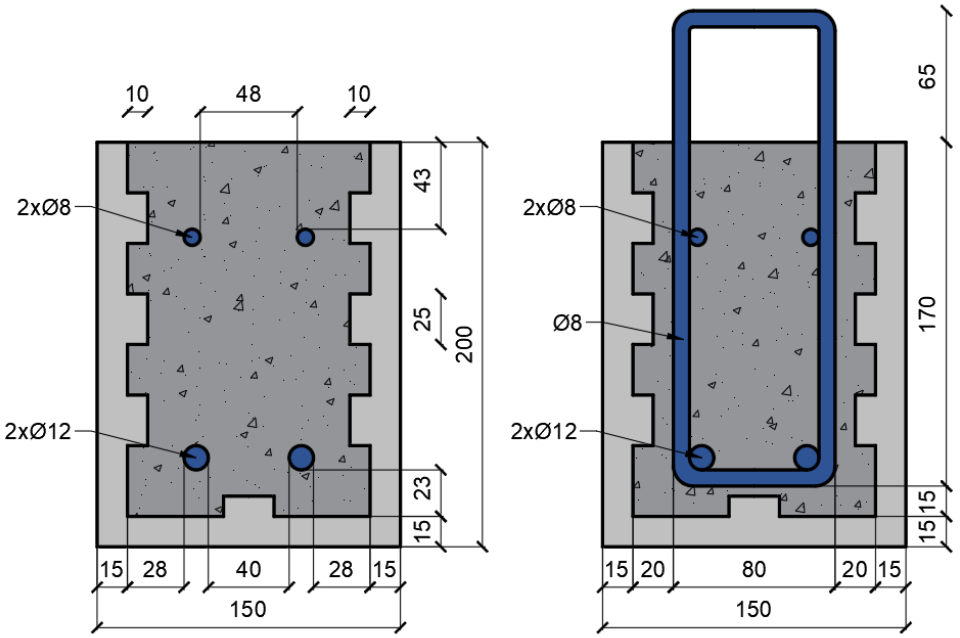

Figure 36. Cross section A (a) and B (b) of HBTL2.

4. Material and tests

4.1 Concrete mix

The concrete used to fabricate the beams contains rapid hardening Portland cement (Table 5). The same concrete mix composition is used in all experiments. The compressive strength of the concrete was determined according to NEN-EN 12390-3 [91], based on 150 mm cubes, and the results were verified on conformity according to NEN-EN 206 [92] for two different batches (Table 6). The concrete cubes are sealed and cured at room temperature in a dry environment. The concrete characteristic compressive strength f_{ck} was determined with expression $f_{ck} = f_{cm}$- 8 from the Eurocode [1], where f_{cm} is the mean compressive strength. The concrete mix for the bending test (C4P) and shear test (C3P) has a characteristic compressive strength of 40.4 MPa and 38.8 MPa, respectively (Table 6). Hence, the concrete strength grade is C30/37. The elastic modulus of concrete in compression was determined according to NEN-EN 12390-13 [93] (Appendix C). C4P has an elastic modulus of 38.6 GPa and C3P has an elastic modulus of 38.2 GPa.

Material	kg/m^3
CEM I 52.5R	260.0
Sand 0.125 - 0.25 mm	78.8
Sand 0.25 - 0.50 mm	256.2
Sand 0.5 - 1.0 mm	256.2
Sand 1 - 2 mm	157.7
Sand 2 - 4 mm	98.5
Sand 4-8 mm	394.2
Gravel 6-16 mm	729.2
Water	156
SP	0.26

Table 5. Concrete mix composition.

Batch	$f_{c,i}$	f_{cm}	f_{ck}	$f_{c,i} \geq f_{ck} - 4$
C4P	49.01	48.4	40.4	✓
	47.76			✓
	48.37			✓
C3P	46.59	46.8	38.8	✓
	47.19			✓
	46.50			✓

Table 6. Characteristic concrete compressive strength at 28 days (Unit = MPa).

4.2 SHCC mix

Through laboratory testing on different cementitious mixtures containing PE fibres (Table 7), a suitable mix design for printable SHCC was created. The fibres have a length of 6 mm. To begin with, a PE-SHCC reference mix design (SF5-SP0.2 from Table 7) was chosen based on a PVA-SHCC mixture [94].

Mix name	CEM III/B 42.5R	Silica fume (%)[1]	Limestone powder	Water	PE fibres 6mm (%)[2]	SP	VMA [%][3]
SF5-SP0.2	939.7	49.5 (5)	494.6	395.7	18.8 (1.92)	2.5	0
SF5-SP0.2-V10							0.10
SF5-SP0.2-V20							0.20
SF5-SP0.3	939.4	49.4 (5)	494.4	395.7	18.8 (1.92)	2.9	0
SF5-SP0.3-V05							0.05
SF5-SP0.3-V10							0.10
SF10-SP0.3	835.1	92.8 (10)	463.9	371.1	17.6 (1.80)	2.7	0
SF10-SP0.3-V05							0.05
SF5-SP0.35-V05	938.9	49.4 (5)	494.1	395.3	18.8 (1.92)	3.6	0.05
SF5-SP0.45-V05	938.3	49.4 (5)	493.8	395.1	18.8 (1.92)	4.3	0.05
SF5-SP0.6-V05	937.0	49.3 (5)	493.2	394.5	18.7 (1.92)	5.9	0.05
PE1SF10	841.8	93.5 (10)	467.6	374.1	9.8 (1.0)	2.9	0
PE1SF12.5	806.6	114.7 (12.5)	448.1	358.5	9.4 (0.96)	2.8	0
PE1SF15	770.9	136.2 (15)	428.3	342.6	9.0 (0.92)	2.6	0
PE1.5SF0	1065.0	0	532.5	426	14.9 (1.5)	2.1	0
PE1.25SF0	1067.9	0	533.9	427.2	12.3 (1.25)	2.1	0
PE1SF0	1070.6	0	535.3	428.3	9.8 (1.0)	2.1	0
PE1.25SF10	839.7	93.3 (10)	466.5	373.2	12.3 (1.25)	2.8	0
PE1SF10	841.8	93.5 (10)	467.6	374.1	9.8 (1.0)	2.9	0
PE1SF0	1070.6	0	535.3	428.3	9.8 (1.0)	2.1	0

Table 7. List of mixtures (Unit = kg/m^3).

Afterwards, the influence of viscosity modifying agents (VMA), superplasticizer (SP), silica fume (SF) and PE fibre content on the rheological, compressive and tensile properties was investigated with a slump flow test, uniaxial compressive test and uniaxial tensile test.

[1] By mass total binder (cement + silica fume)
[2] Volume fraction fibres
[3] By mass total binder (cement + silica fume)

4.2.1 Material test setup

The flowability of the fresh mixtures was evaluated with a slump flow test, performed according to ASTM C1437-20 [95]. A cone mould with an upper diameter of 70 mm, a bottom diameter of 100 mm and a height of 60 mm was cast on a slump flow table at a fixed time interval to determine the development of the slump as time progresses. The cementitious materials were sealed in a plastic bag during the test to prevent excessive moisture loss.

The compressive strength of several mix compositions were determined through an uniaxial compression test on small cubes according to NEN-EN 196-1 [96]. Three small cubes of 40mm were cut from a prism (160 mm x 40 mm x 40 mm) and cured at 20° (±2) in a curing room with a RH > 95%, 24 hours after casting. The loading rate was 1.5 MPa/s.

The strain-hardening behaviour is an important characteristic of SHCC, thus it is necessary to confirm that the mix compositions can be classified as SHCC. For this purpose, displacement controlled uniaxial tensile tests on dog bone specimens were conducted to characterize the tensile behaviour (Figure 37). The dog bone specimens were demoulded 24 hours after casting and subsequently cured at 20° (±2) in a curing room with a RH > 95%. Two external linear variable displacement transducers (LVDTs) were attached to the specimens to measure vertical displacements. The deformations were measured with a gauge length of 80 mm.

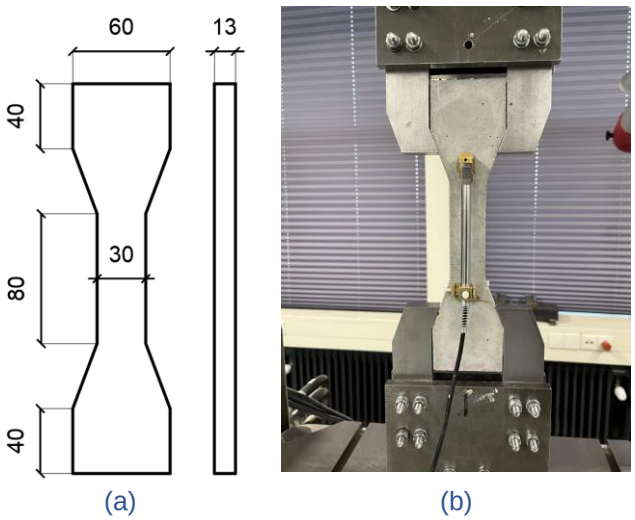

Figure 37. Dimensions dog bone specimen in mm (a) and uniaxial tensile test setup (b).

4.3 Structural tests

4.3.1 Fabrication of beams

Eight beams are fabricated. Four beams consisting of a control beam (CB1) and three hybrid beams (HBT1, HBTL1 and 3DHB1) are tested in a (four-point) bending test and four beams (CB2, HBT2, HBTL2 and 3DHB2) are tested in a shear test. Trial experiments are conducted in order to find a suitable fabrication method (Appendix B). The final fabrication process of the beams is described in this section.

4.3.1.1. Precast SHCC U-shaped formwork

The SHCC U-shaped permanent formwork are fabricated using wooden shuttering, extruded polystyrene (XPS) and rubber. The formwork was cast invertedly to make the casting process easier (Figure 38). An inner mould consisting of XPS plates which are wrapped together with tape, was glued to the bottom of the wooden mould with silicon glue to keep the inner mould in place (Figure 38.1). Two

strips of rubber with holes were glued to two outer plates of the Styrofoam mould for the creation of shear keys (Figure 39). After the inner mould is in place, SHCC was cast inside the wooden mould (Figure 38.2). After one day of hardening, the wooden mould was turned upside down and removed (Figure 38.3). At this point, a SHCC U-shaped with Styrofoam remains. The inner part of the Styrofoam was able to be removed with a crowbar (Figure 38.4). Vaseline was applied on the surface of the XPS plates to reduce the friction for the vertical sliding motion. The design of the rubber to create shear keys is adopted from another master thesis [97]. The original rubber strip (1.4 m) was cut in half to create two rubber strips of 0.7 m (Figure 40).

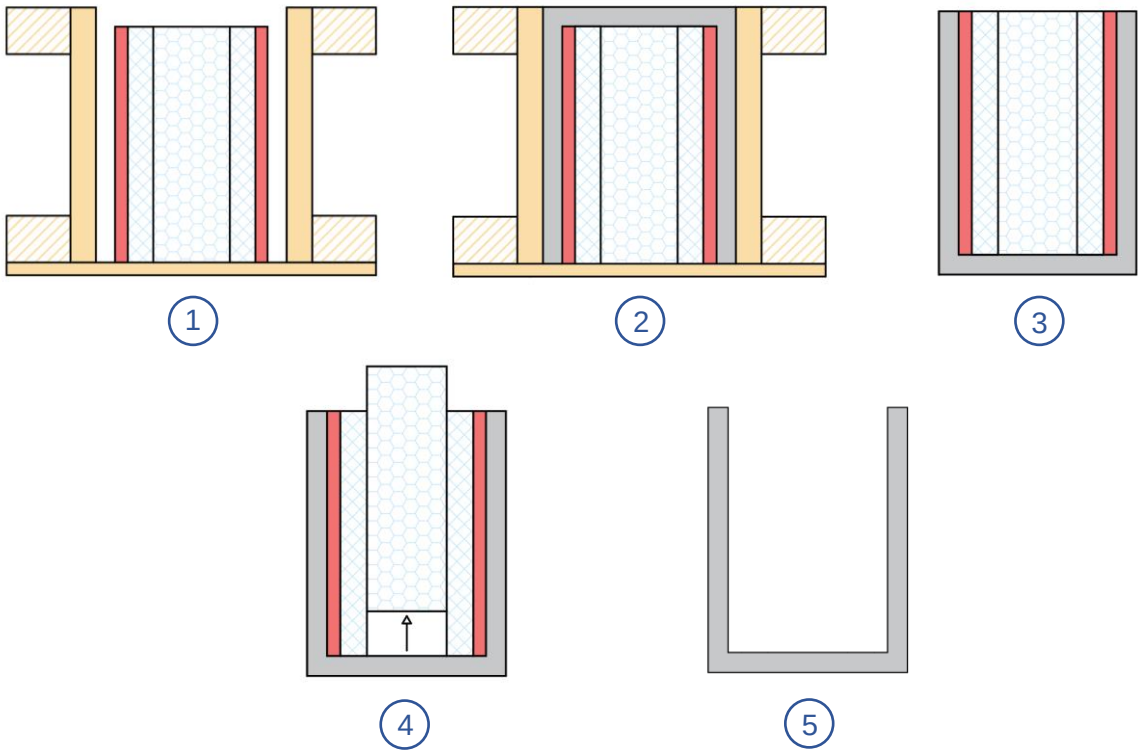

Figure 38. Schematic overview of the steps involved in the casting procedure of the precast SHCC U-shaped formwork.

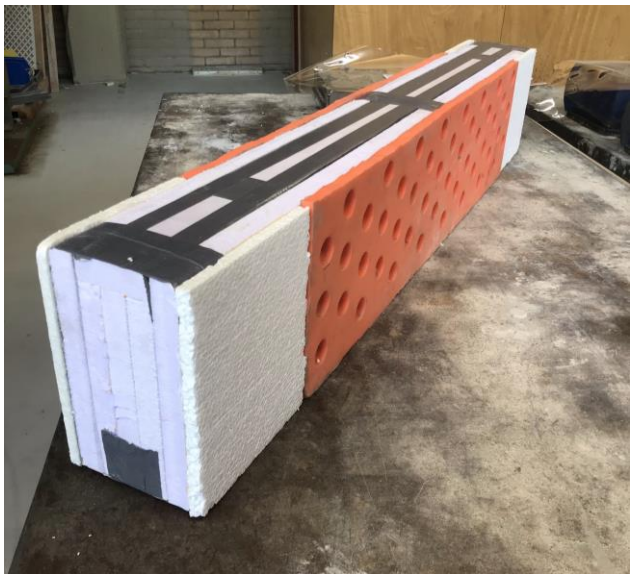

Figure 39. Inner mould for the precast SHCC U-shaped formwork.

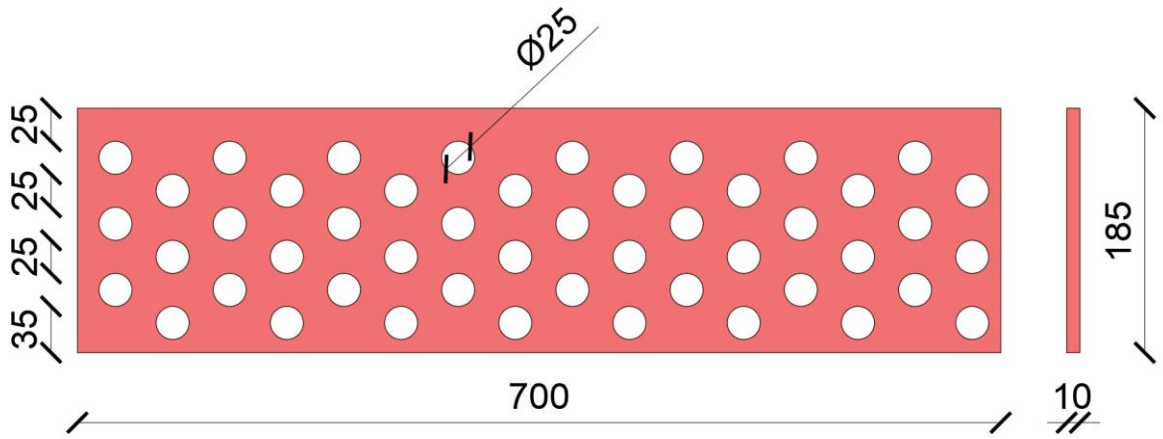

Figure 40. Dimensions rubber strip in mm.

The method described in Figure 38 is used to cast the SHCC U-shaped permanent formwork for beam specimen HBT1 and HBT2 (Figure 41). Application of Vaseline was necessary to achieve vertical displacement of the Styrofoam with a crowbar (Figure 41.4). The casting procedure of HBTL1 and HBTL2, the hybrid beams with transverse and longitudinal shear keys, was exactly the same, however in order to make longitudinal shear keys, holes were drilled in the horizontal XPS plate. The transverse and longitudinal shear keys span a length of 700 mm in the middle of the U-shaped formwork (Figure 42). The variation in the thickness of the webs (11-17 mm) is a result of the non-uniform thickness of the rubber strip and position of the Styrofoam inner mould inside the wooden mould.

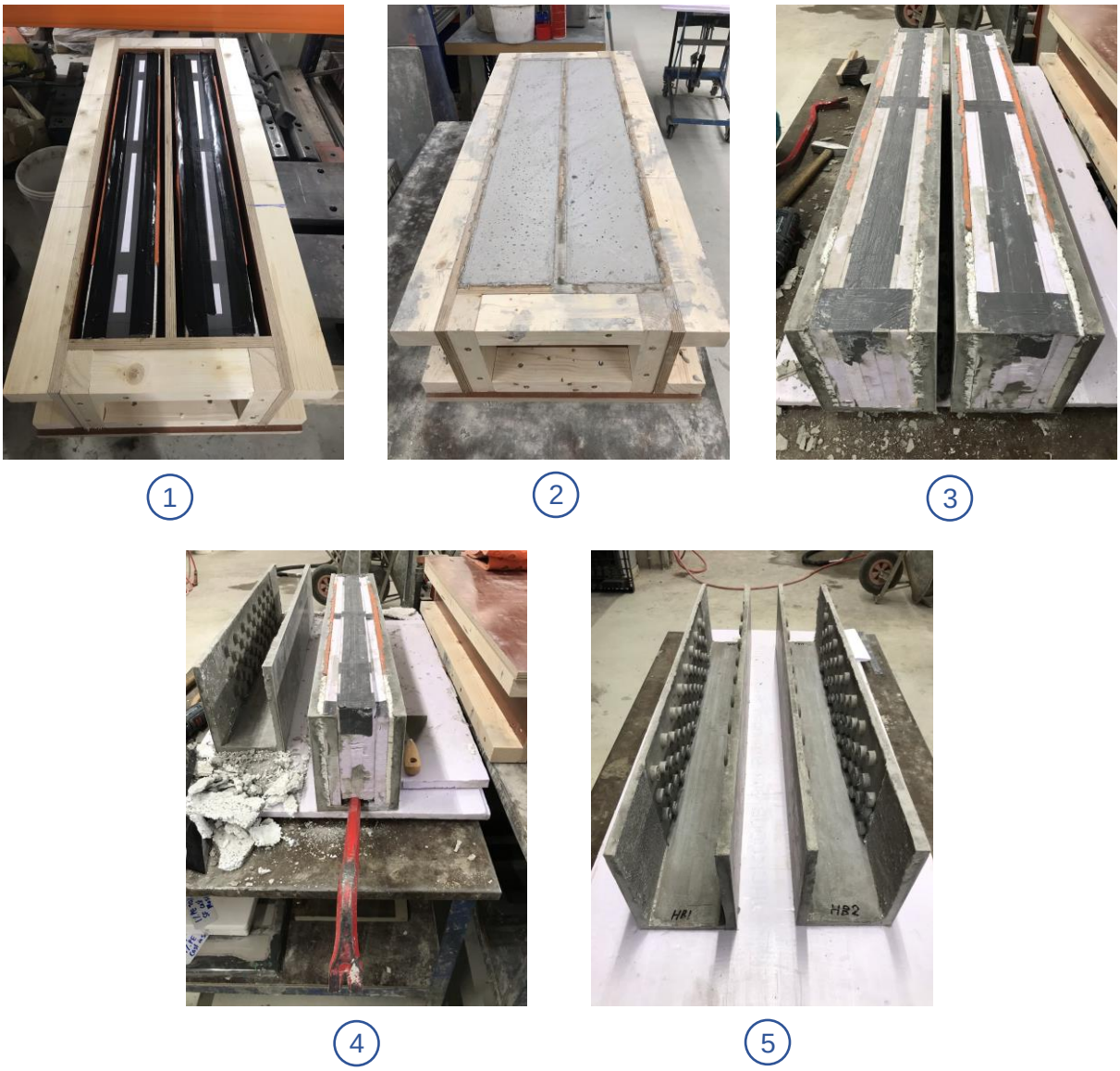

Figure 41. Casting procedure of HBT1 and HBT2.

Figure 42. From right to left: HBT1, HBT2, HBTL1 and HBTL2.

4.3.1.2. 3D printed SHCC U-shaped formwork

Extrusion-based 3D printing is employed to create two SHCC U-shaped permanent formwork. The printing setup consists of a mixing machine, conveying pump, printhead, pressure gauge, screw pump, hose and nozzle (Figure 43). The nozzle has a diameter of 15 mm (Figure 44a). The printhead speed was set to 4800 mm/min and the nozzle stand-off distance was constant 10 mm. The cementitious material was prepared in four batches of (4+6)-6-6-6 litres. The time between adding mixing water for one batch and the following batch was 10 minutes. The printing process commenced after the third batch was ready, which is 30 minutes after adding mixing water of the first batch.

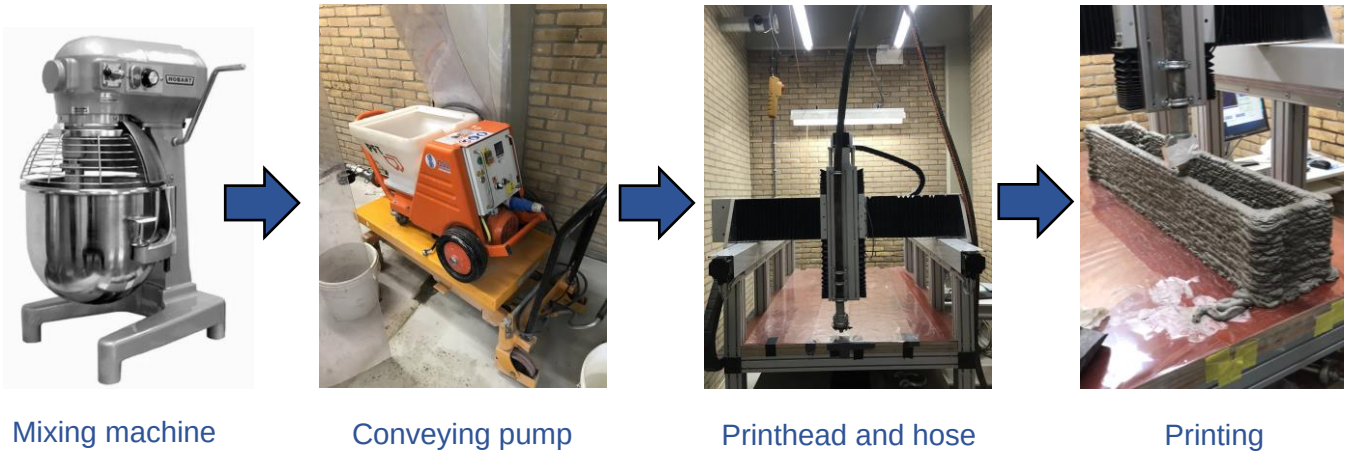

Figure 43. Printing equipment for extrusion-based 3D printing.

The filaments in the soffit of the 3DP-SHCC permanent formwork are printed longitudinally, in the direction of the tensile stresses, instead of perpendicular (Figure 44b). Therefore, the resistance of beam 3DPHB1 and 3DPHB2 are governed by the strength of the printed filaments in the soffit (tension zone) rather than the bond strength of adjacent filaments [10].

(a) (b)

Figure 44. Print nozzle (a) and printing pattern for the 3DP-SHCC permanent formwork (b).

4.3.1.3. Casting concrete

After the precast and 3DP-SHCC permanent formwork have hardened, the specimens are prepared for casting concrete (Figure 45). The reinforcement cages are locked in placed with plastic spacers. The same concrete mix composition is used for all beams (Table 5).

(a)

(b)

(c)

(d)

Figure 45. Moulds of CB1/CB2 (a), HBT1/HBTL1 (b), HBT2/HBTL2 (c) and 3DHB1/3DHB2 (d) before pouring concrete.

The concrete was prepared in two batches, one batch for the beams tested in bending and one batch for beams tested in shear. All the concrete was cast on the same day, whilst the curing age of the SHCC formwork was different (Table 8). The formwork were cured at room temperature (20° ± 2) with a RH>95%. The beams are demoulded 28 days after casting the concrete. Subsequently, the surface of sides of the beams are painted white in preparation of Digital Image Correlation (DIC) analysis (Figure 46).

Beam	Curing age
HB1T	19 days
HB2T	19 days
HB1TL	14 days
HB2TL	14 days
3DHB1	11 days
3DHB2	19 days

Table 8. Curing age SHCC in the beams at the moment of pouring concrete.

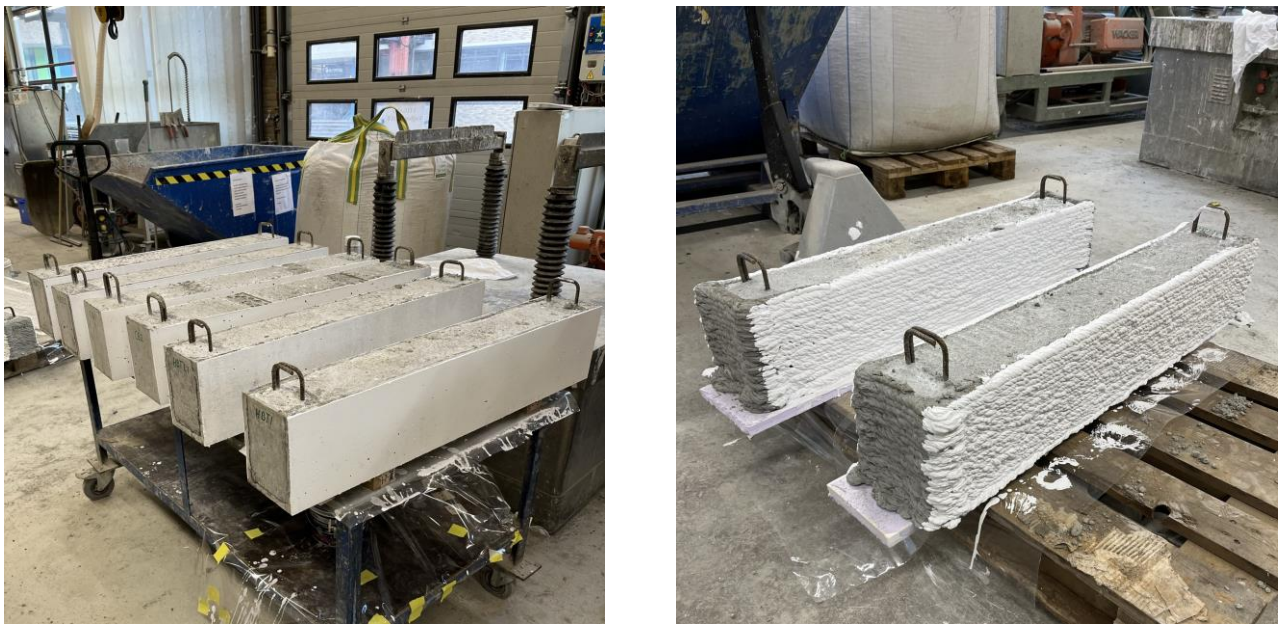

(a) (b)

Figure 46. Hybrid beams with precast SHCC formwork, including control beams (a) and printed SHCC formwork (b).

4.3.2 Bending test

A four-point bending test was conducted on four beams: CB1 (Figure 29), HBT1 (Figure 30), HBTL1 (Figure 31) and 3DHB1 (Figure 32), under displacement control at a rate of 0.01 mm/s. The distance between the supports is 800 mm and the constant moment region between the load points is 400 mm. All beams have a height of 200 mm and all beams except 3DHB1 have a width of 150 mm. Beam 3DHB1 has a width of 180 mm. The reinforcement layout is displayed in Figure 28. During each test, the deformation of the beams was captured on both sides with Digital Image Correlation (DIC). LVDTs

were applied to measure the midspan deflection, deformation in the tension zone and opening between SHCC and concrete at mid span, and verify the results obtained from the DIC. The width of the loading and support plates is equal to the total width of the beam. The experimental setup is shown in Figure 47.

Figure 47. Experimental setup bending experiment.

4.3.2.1. LVDTs

One LVDT (LVDT01) and three LVDTs (LVDT06, LVDT07, LVDT08) were placed on all four beams (CB1, HBT1, HBTL1 and 3DHB1) in order to verify the data obtained from the DIC analysis. LVDT01 measures the midspan deflection whilst LVDT6, LVDT7 and LVDT8 measures the tensile deformation at the bottom of the beams, within the constant moment region (Figure 48). In addition, two extra LVDTs (LVDT03 and LVDT04) were placed on top of the hybrid beams to measure the out-of-plane opening between the SHCC web and concrete (Figure 49).

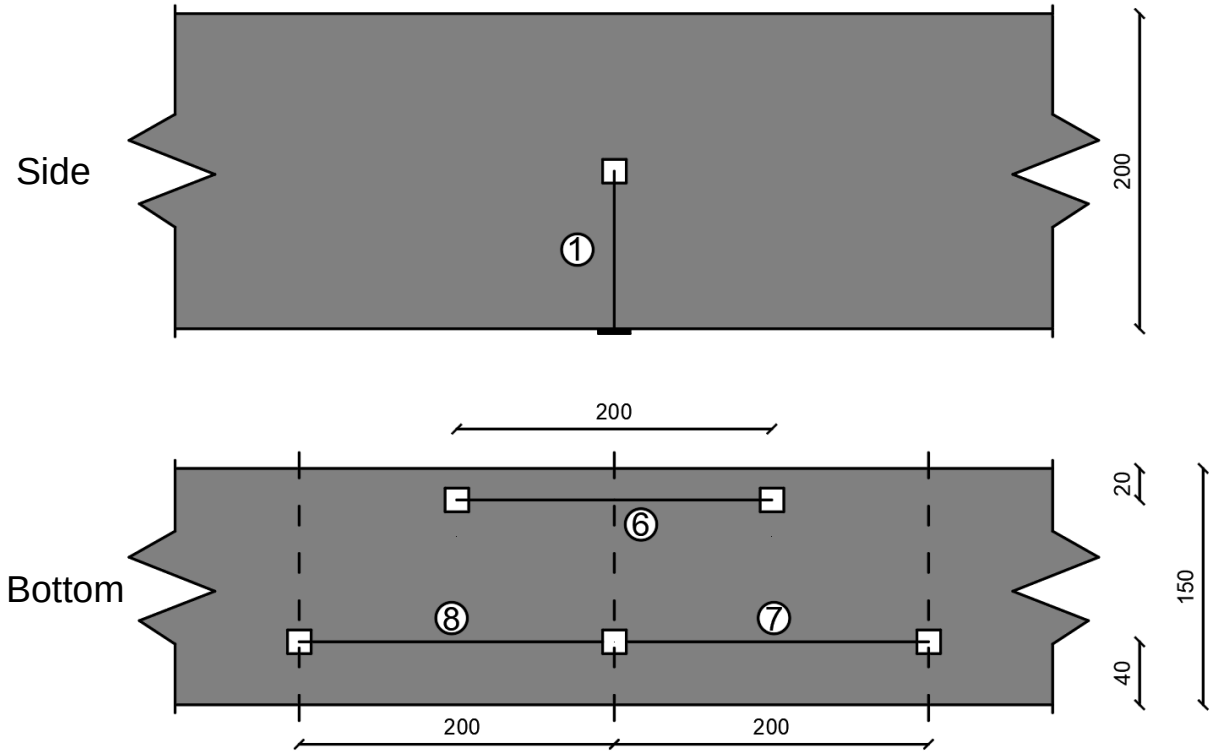

Figure 48. LVDT positions at the side and bottom of the beams.

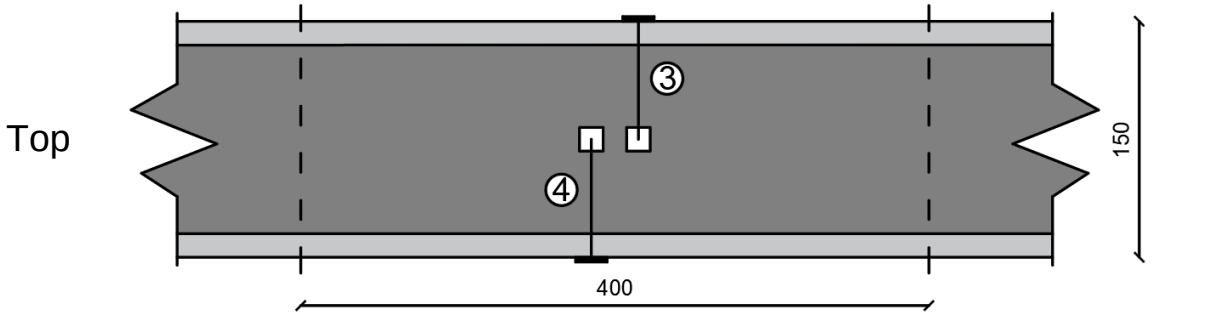

Figure 49. LVDT positions at the top of the hybrid beams.

4.3.3 Shear test

A three-point bending test was conducted on four beams: CB2 (Figure 34), HBT2 (Figure 35), HBTL2 (Figure 36) and 3DHB2, under displacement control at a rate of 0.01 mm/s. The distance between supports is 800 mm. All beams have a height of 200 mm and all beams except 3DHB2 have a width of 150 mm. The reinforcement layout is displayed in Figure 33. During each test, the deformation of the beams was captured with Digital Image Correlation (DIC). LVDTs were applied to measure the vertical and horizontal deformation at several locations, and verify the results obtained from the DIC. The span is equal to 800 mm. The width of the loading and support plates is equal to the total width of the beam (150 mm). The experimental setup is shown in Figure 50.

Figure 50. Experimental setup shear experiment.

4.3.3.1. LVDTs

One LVDT (LVDT01) and one LVDT (LVDT02) were placed on all the beams to measure the midspan deflection and deformation in the compression zone, respectively (Figure 51). Four LVDTs (LVDT03, LVDT04, LVDT05, LVDT06) and four LVDTs (LVDT07, LVDT08, LVDT09, LVDT10) were placed on top of the hybrid beams to measure the opening and sliding of the SHCC web relative to the concrete (Figure 51).

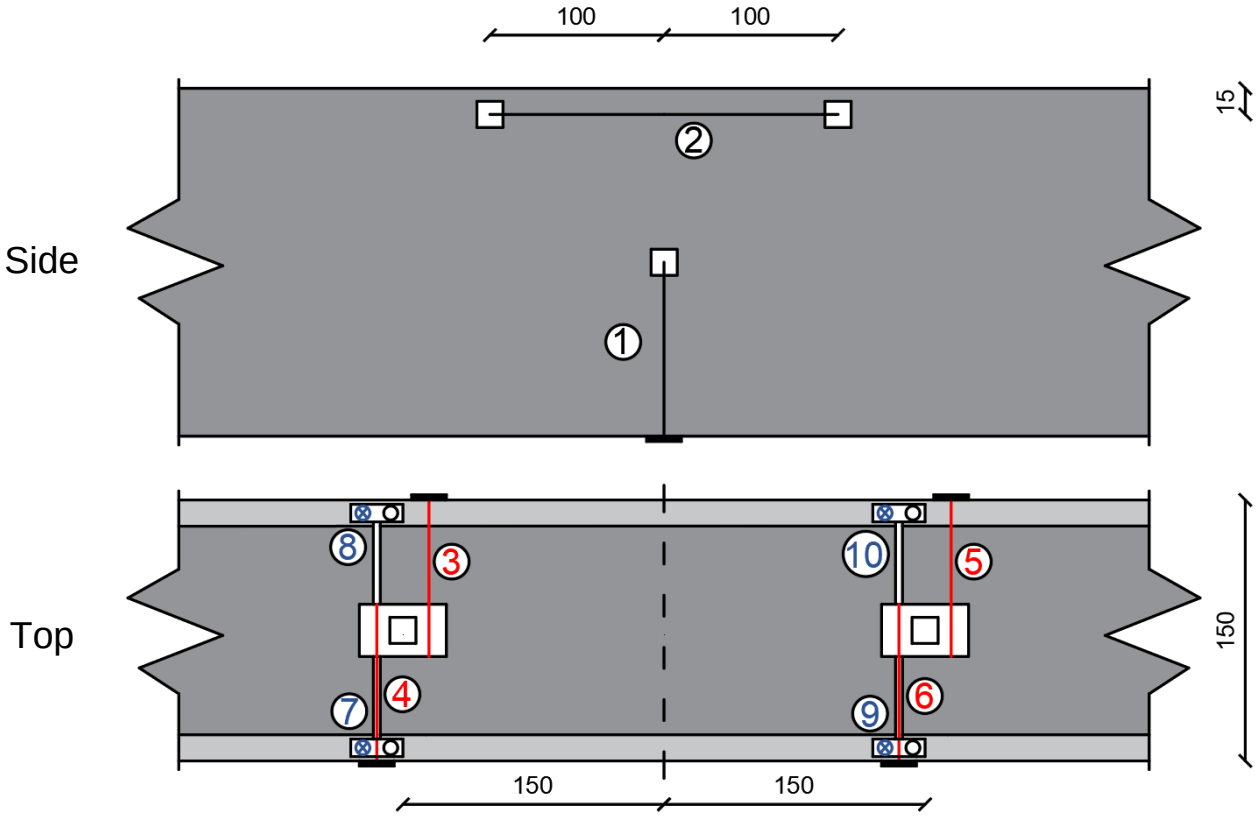

Figure 51. LVDT positions in the shear test.

5. Experimental results

5.1 SHCC mix design

5.1.1 Slump flow test

Two series of slump flow tests were performed on mixtures listed in Table 7. In the first series tests, the influence of VMA, SP and SF content of cementitious mixtures with a PE fibre content of 1.8% to 1.92% on the slump and slump flow was investigated. In the second series, the slump and slump flow of mixtures with a PE fibre content up to 1%, no VMA and varying SF content were determined. In both series of test, the slump was evaluated directly after removing the cone mould and the slump flow was evaluated after dropping the flow table 25 times.

5.1.1.1. First series

The cone height (Figure 52) and slump flow (Figure 53) have been assessed every 15 minutes, until 90 minutes after adding mixing water. For all tested mixtures it holds that increasing the VMA content resulted in a higher cone height and lower slump flow value, whereas increasing the SP content from

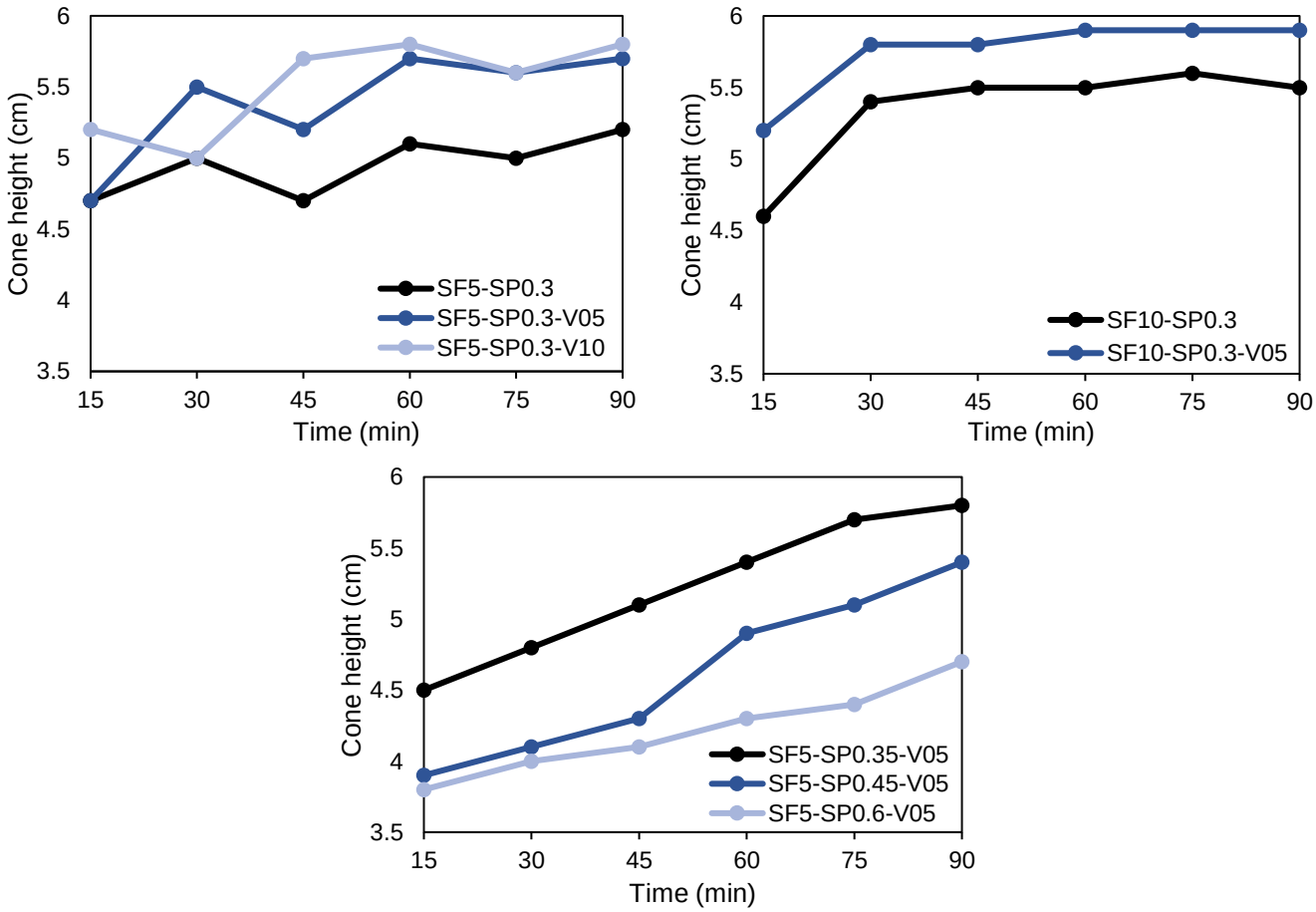

Figure 52. Cone height directly after removing the cone mould (volume per mixture = 2.5 L).

0.20% to 0.30% by mass of total binder resulted in a higher slump flow. Moreover, a decrease in slump flow was observed when increasing the silica fume content from 5% to 10% by mass of total binder.

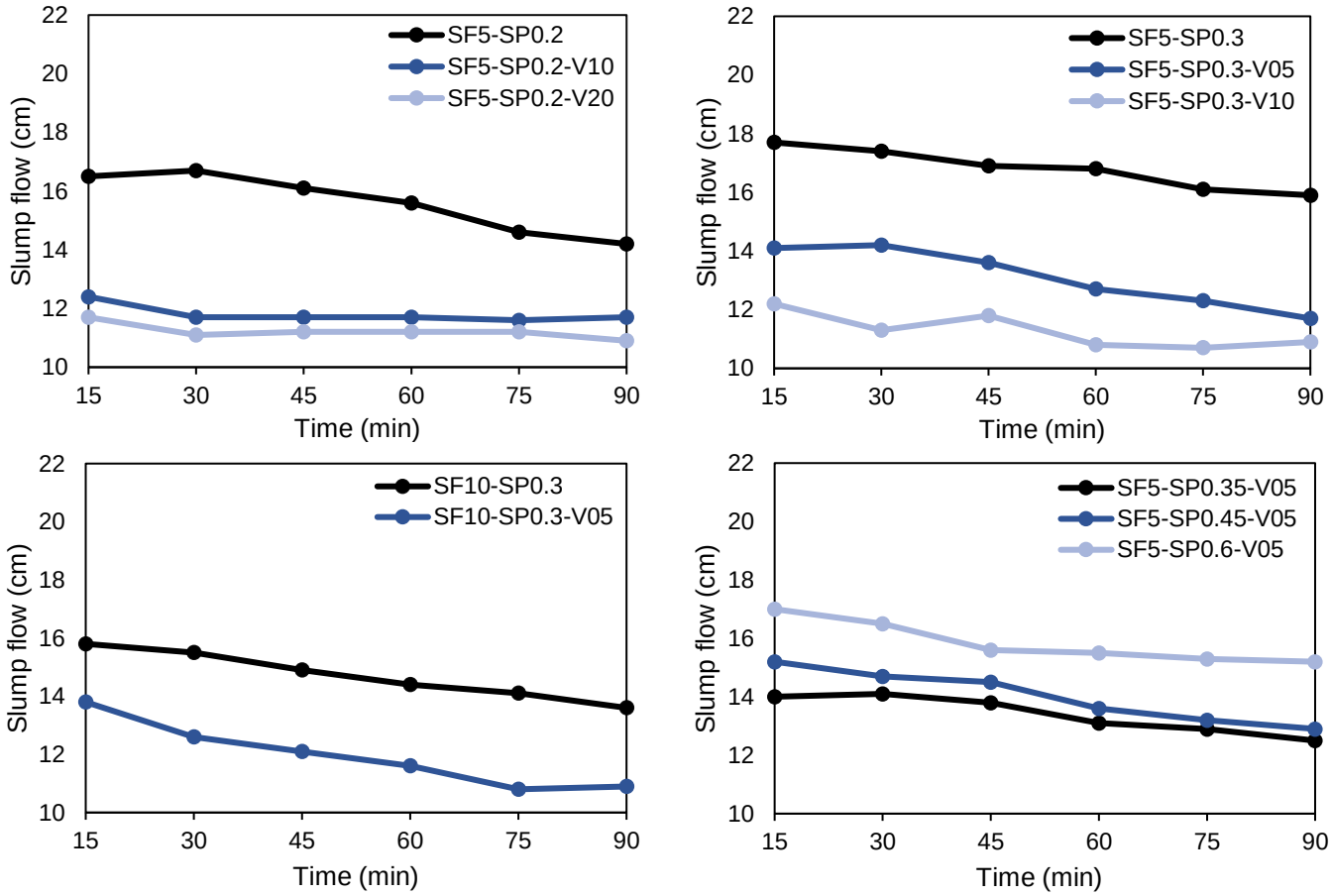

Figure 53. Slump flow after dropping the flow table for 25 times (volume per mixture = 2.5 L).

5.1.1.2. Second series

Three mix compositions from Table 7 with a PE fibre content up to 1% and a SF content of 10% (PE1SF10), 12.5% (PE1SF12.5) and 15% (PE1SF12.5) by mass percentage of total binder were subjected to a slump flow test. Mixture PE1SF10 is similar to SF10-SP0.3 from the first series, but with a reduced fibre content. When the fibre content of a mixture is reduced, the workability and hence, the slump flow will increase [98, 99]. As expected, an increase in slump flow was observed when the fibre content was lowered (Figure 54). Also, PE1SF12.5 and PE1SF15 had a lower slump flow compared to PE1SF10. The slump flow of PE1SF12.5 went from 19.9 cm to 14.5 cm within a time span of 75 min. A previous study mentioned that a slump flow between 150 mm and 190 mm is desirable for printable cementitious materials [51]. Based on this observation, another slump flow test with mixture PE1SF12.5 was carried out, this time with a shorter interval (10 min) and a volume of 4 L (Figure 55).

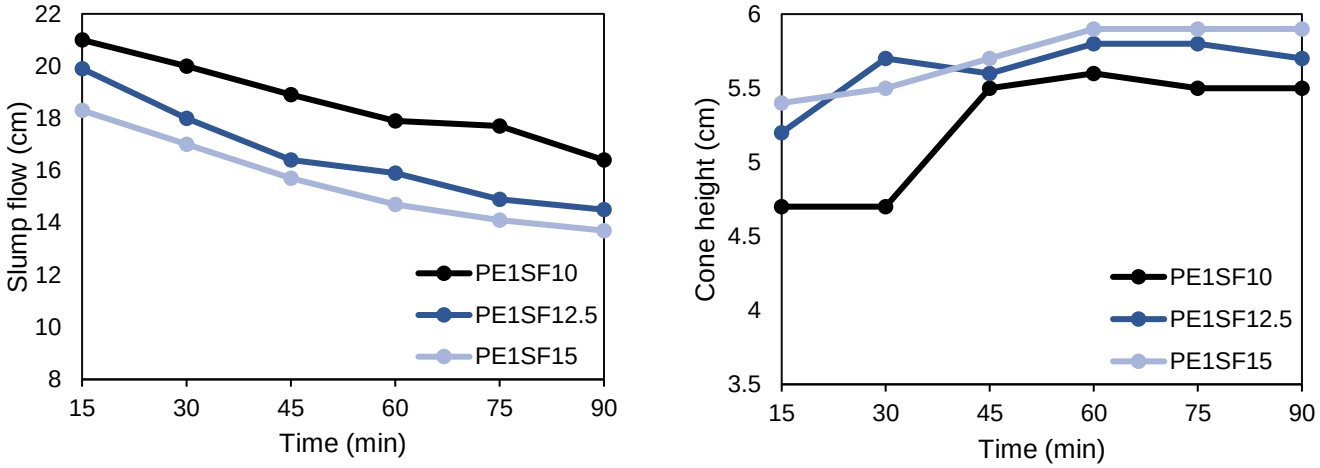

Figure 54. Slump flow (after dropping the table) and cone height (after removing the cone mould) (volume per mixture = 1 L).

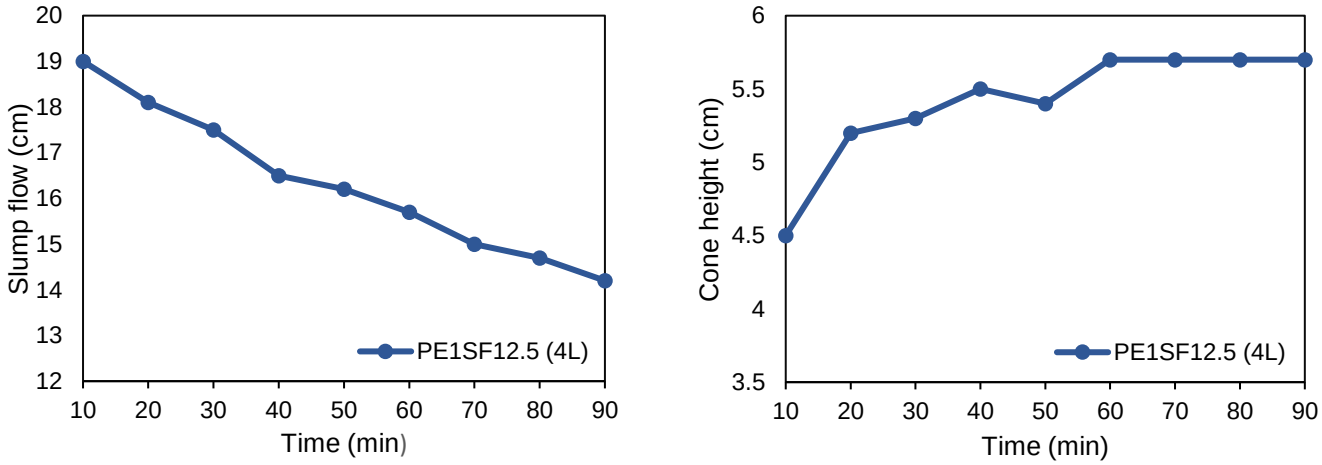

Figure 55. Slump flow (after dropping the table) and cone height (after removing the cone mould).

5.1.2 Printing experiments

It was opted to carry out pumpability tests and small-scale print experiments with mixture SF5-SP0.6-V05 from the first series and mixture PE1SF12.5 from the second series, since the slump flow test results of these two mixtures were promising. In the pumpability test, cementitious material is extruded by a conveying pump (Figure 56). The goal of the test is to see whether the pump is compatible with

Figure 56. Conveying pump used for 3D printing

the mixture and find an estimation of the printability window by calculating the flow rate of the extruded material at a predefined constant pump speed. It was observed that both materials were extrudable at least 60 minutes after addition of mixing water.

The pumpability test was followed by small-scale print sessions to evaluate the print quality of the printed material and to find a suitable nozzle standoff distance and print speed. Two problems occurred during the printing experiment when using mixture SF5-SP0.6-V05. The printed filaments contained large gaps, likely caused by the adhesiveness of the material. The material was dragged by the printhead, which created gaps in the filaments. Additionally, blockage arose between the pressure gauge and screw pump due to accumulation of fibres. Therefore, the experiment had to be stopped earlier than anticipated. The undesired adhesiveness of SF5-SP0.6-V05 is attributed to the VMA content. From research it is known that VMA increases the cohesiveness of cementitious materials [63]. Furthermore, the fibre dispersion of SF5-SP0.45-V05 was not optimal due to the high amount of fibres (1.92% by volume). Fibre flocks of roughly 3 mm were already present in the fresh mixture before printing and this brought about the blockage problem. The blockage and large voids did not occur when printing with mixture PE1SF12.5. Additionally, the yield stress of PE1SF12.5 was sufficient to print twenty layers.

5.1.3 Uniaxial compressive test

The effect of silica fume, PE fibre content and casting method on the compressive strength of cementitious materials from Table 7 was investigated. The effect of silica fume on the compressive strength of SHCC and concrete is comparable [100, 101]. Silica fume tends to increase the compressive strength of the cementitious materials (Table 9), similarly as in the case of concrete. Furthermore, reduction of PE fibres increases the compressive strength. The same effect was observed by Wang, et al. [99]. Cubes cast with printed cementitious material (PE1SF10 (P)) had a lower compressive strength compared to conventional cubes with the same mix composition.

	SF5-SP0.45-V05	SF5-SP0.6-V05	PE1SF0	PE1SF10	PE1SF10 (P)	PE1.25SF0	PE1.25SF10
7d	40.9	37.7	50.9	58.0	45.1	43.0	50.5
14d	52.3	41.7	56.6	62.8	50.3	47.3	51.0
28d	52.5	45.2	57.3	65.6	54.2	51.4	55.4

Table 9. Average 7-, 14- and 28-day cube compressive strength of 40 mm cube specimens (Unit = MPa).

5.1.4 Uniaxial tensile test

The influence of PE fibre volume fraction and silica fume content on the tensile stress-strain relation was analysed with an uniaxial tensile test. The setup of the experiment is mentioned in Figure 37. The tensile stress-strain relation of the mixtures indicate that the mixtures with PE-1% still exhibit strain-hardening behaviour with a relatively high average ultimate tensile strength $\bar{\sigma}_{tp}$ and average ultimate tensile strain $\bar{\varepsilon}_{tu}$ (Figure 57). The ultimate tensile strain ε_{tu} is defined as the strain at 85% of the maximum stress. Two out of three dog bone specimens of PE1.25SF10 failed outside the measuring zone, likely caused by improper mixing (Figure 58b).

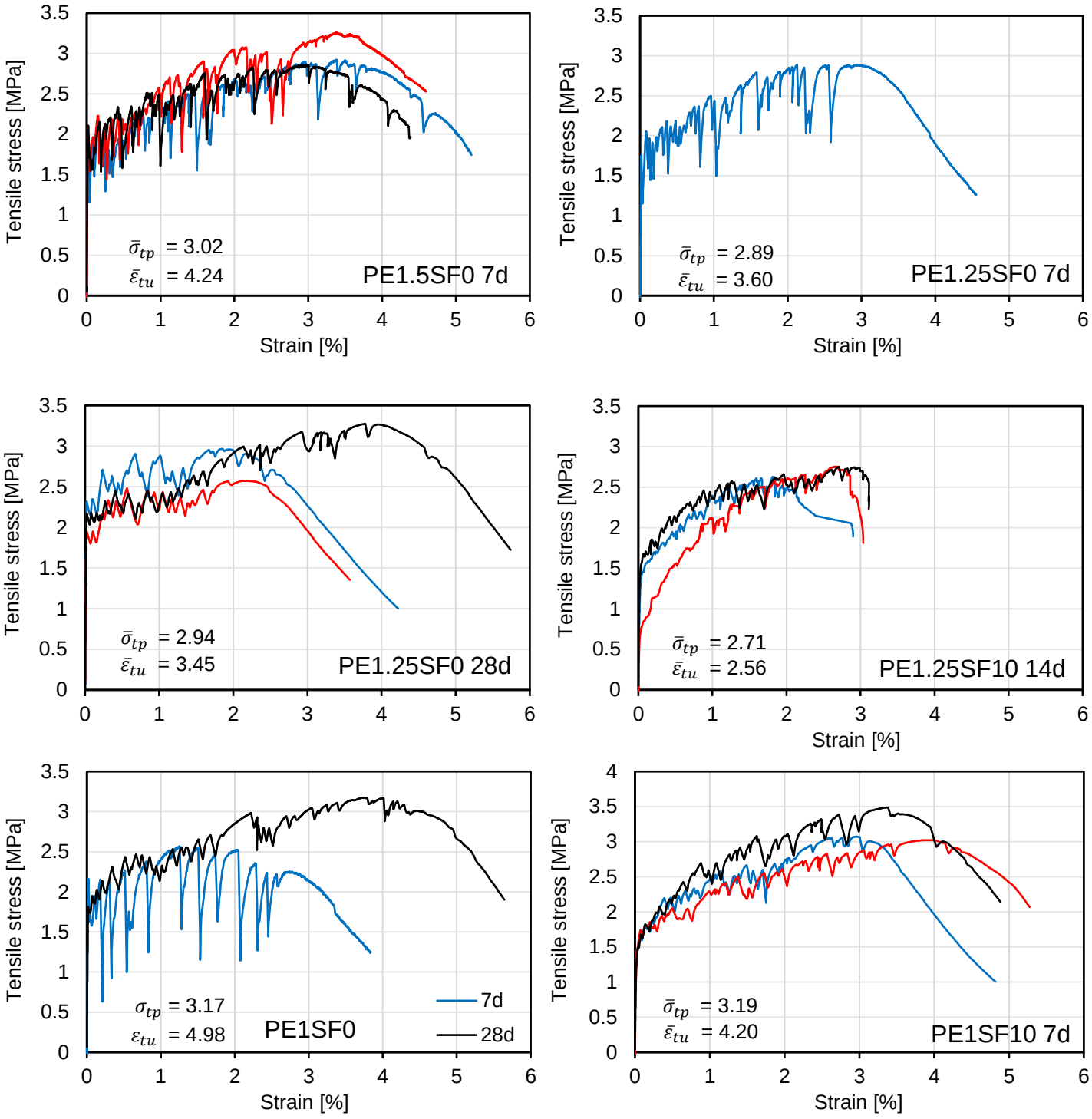

Figure 57. Tensile stress – strain relation.

(a) (b)

Figure 58. Cracks in dog bone specimens of PE1SF10 (a) and PE1.25SF10 (b).

5.1.5 Final SHCC mix design

The final SHCC mix composition used in the precast and printed U-shaped permanent formwork, PE1SF10 and PE1SF12.5 respectively, are displayed in Table 10. The difference in mix composition for the precast and printed SHCC formwork is due to the difference in rheology requirement for casting SHCC and printing SHCC. A flowable mixture was desirable for the precast SHCC permanent formwork to fill the holes in the rubber strip. For this reason, it was opted to reduce the silica fume content to 10% for the precast SHCC formwork in order to increase the flowability of the material. Mixture PE1SF12.5 was compatible with the printing setup in the lab and had sufficient yield stress to print a SHCC permanent formwork consisting of 20 layers. All the final SHCC mixes have a fibre length of 6 mm.

Name	CEM III/B 42.5R	Silica fume (%)	Limestone powder	Water	PE fibres 6 mm (%)	SP	w/b
PE1SF10	841,8	93,5 (10)	467,6	374,1	9.8 (1.0)	2.9	0.4
PE1SF12.5	806.6	114.7 (12.5)	448.1	358.5	9.4 (0.96)	2.8	0.39

Table 10. Final SHCC mix composition for the precast and printed U-shaped permanent formwork (Unit = kg/m^3).

5.1.5.1. Tensile properties

The tensile stress-strain curve of the final cementitious mixes were determined with an uniaxial tensile test to quantify the strength and ductility (Figure 59 and Figure 60). PE1SF10-T refers to the mixture used to cast the U-shaped formwork with only transverse shear keys and PE1SF10-TL refers to the U-shaped formwork with both transverse and longitudinal shear keys. PE1SF12.5 has a lower average ultimate strain $\bar{\varepsilon}_{tu}$ as compared to the other two mixtures (Table 11 Table 11). Presumably, this is caused by the absence of vibration when casting the dog bone specimens resulting in poor fibre dispersion and cracks appearing outside the measuring zone of the LVDTs (Figure 61). Nonetheless, all tested mixtures exhibited strain-hardening behaviour.

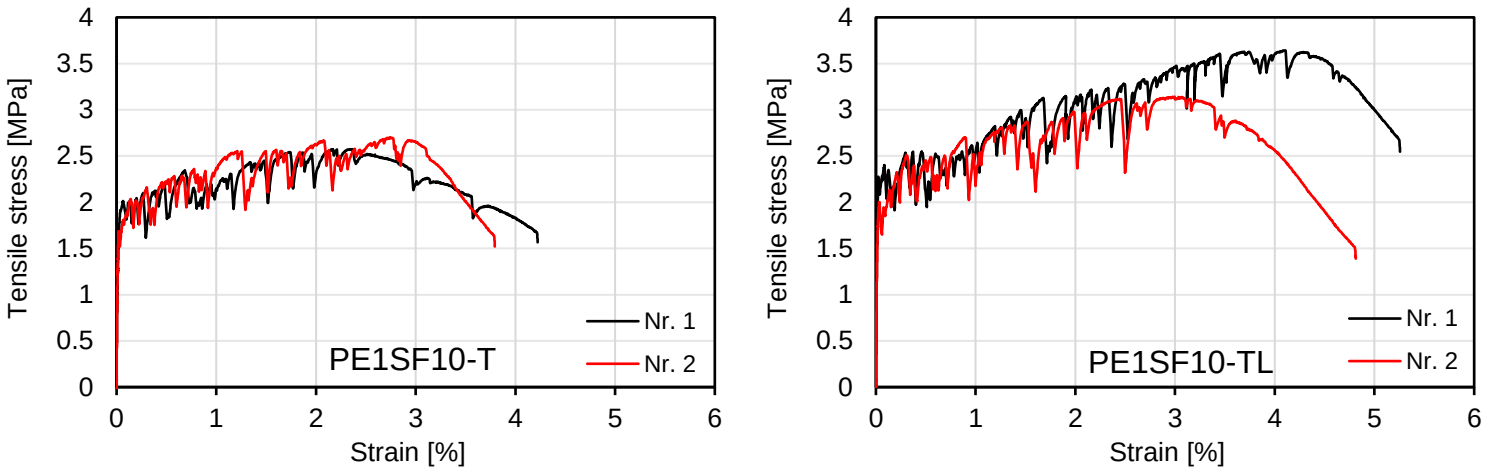

Figure 59. Tensile stress-strain curve of the mixture used in the precast formwork of HBT1 + HBT2 (left) and HBTL1 + HBTL2 (right) at 28 days.

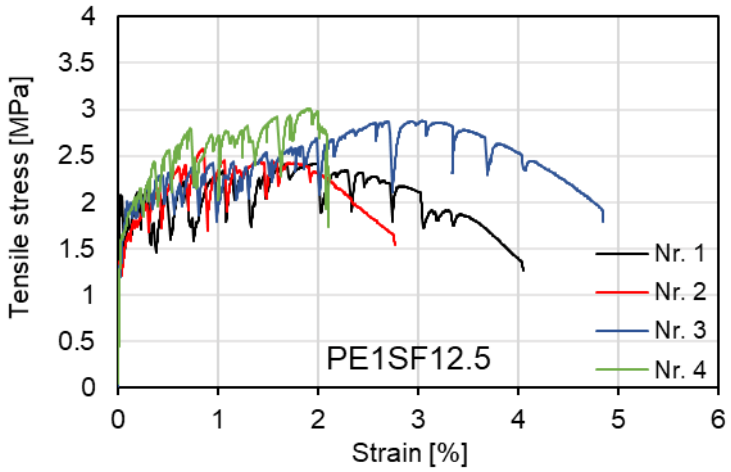

Figure 60. Tensile stress-strain curve of the mixture used in the 3D printed formwork at 28 days.

Name	$\bar{\sigma}_{cr}$ (MPa)	$\bar{\varepsilon}_{cr}$ (%)	$\bar{\sigma}_{tp}$ (MPa)	$\bar{\varepsilon}_{tp}$ (%)	$\bar{\varepsilon}_{tu}$ (%)
PE1SF10-T	1.80	0.03	2.64	2.55	3.31
PE1SF10-TL	2.14	0.03	3.39	3.37	4.20
PE1SF12.5	1.59	0.02	2.72	1.94	2.85

Table 11. Average cracking stress ($\bar{\sigma}_{cr}$), cracking strain ($\bar{\varepsilon}_{cr}$), tensile peak stress ($\bar{\sigma}_{tp}$), peak strain ($\bar{\varepsilon}_{tp}$) and strain capacity ($\bar{\varepsilon}_{tu}$).

Figure 61. Cracks observed in the dog bone specimens of PE1SF12.5.

5.1.5.2. Compressive properties

The compressive strength of the SHCC mixtures was determined with an uniaxial compression test on 40 mm cubes (Table 12).

	PE1SF10-T	PE1SF10-TL	PE1SF12.5
7d	50.3	53.7	51.6
14d	54.1	59.3	57.0
28d	58.5	60.6	60.2

Table 12. Compressive strength of SHCC mixtures (Unit = MPa).

5.2 Structural tests

5.2.1 Bending

5.2.1.1. Load vs. midspan deflection

The load versus midspan deflection for CB1, HBT1, HBTL1 and 3DHB1 shows that all the hybrid beams reached a higher peak load F_{max} compared to the control beam (Figure 62). Beams HBT1, HBTL1 and 3DHB1 had a 47.6%, 61.2% and 55.0% larger peak load compared to the control beam, respectively (Table 13). Additionally, the control beam seems to have a larger deflection at peak load compared to the hybrid beams, which suggests that the control specimen has a superior deformation capacity. After careful examination of the DIC results, it was noticed that the control beam had a cracking behaviour which is not typical for reinforced concrete loaded in bending in one plane (Figure 63). Between load step 39.5 kN and 64.7 kN, out-of-plane motion of the supports was visible, indicating that the experimental setup was not completely stable during the loading phase of the control specimen. Despite this observation, the designed peak load of the control beam was 89.9 kN (Table 3) which does not deviate a lot from the experimental peak load of 98.3 kN (Table 14). The multi-layer (MLM) proposed by Yassiri [9] was also used to predict the failure load of the reference beam (Figure 62). The MLM overestimated the failure load by 4.0%, but the predicted mid span deflection was inaccurate. The unexpected result of the reference beam is further discussed in section 7.1.1.

The load-deflection curve of all hybrid beams were similar up to the yield point of the longitudinal reinforcement, yet all the hybrid beams differ in load carrying capacity. HBTL1 has a 9.6% higher peak load compared to HBT1, probably due to the superior SHCC tensile properties (Table 11) and slightly improved SHCC activation resulting from the longitudinal shear keys. Meanwhile, 3DHB1, the beam with a printed SHCC formwork, has the highest midspan deflection at peak load, even though the 3D printed SHCC mixture has a lower strain capacity compared to the precast SHCC mixture (Table 11). The main

reason for this observation is that 3DHB1 has an unintended larger SHCC formwork thickness of 30 mm compared to the other hybrid beams which have only a thickness of 15 mm.

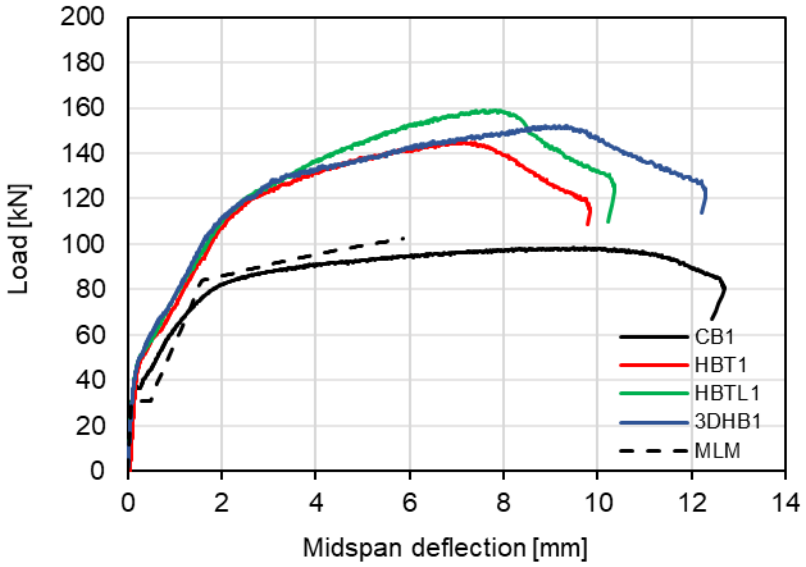

Figure 62. Load vs. midspan deflection.

	F_{max} (kN)	u_{max} (mm)
CB1	98.3	9.73
HBT1	145.1	7.17
HBTL1	159.1	7.84
3DHB1	152.4	9.19
MLM	102.3	5.86

Table 13. Peak load and corresponding midspan deflection.

5.2.1.2. Cracking pattern

The cracking pattern of the tested beams were analysed with DIC at different load steps with software GOM Correlate. The DIC images were chosen based on the load-deflection curve of the beam. For every beam, the number of cracks and crack spacing were evaluated at section 1, which is located at 7.5 mm from the bottom. The results of the DIC analysis are verified with the data from the LVDTs (Appendix D).

Control beam

The propagation of cracks along with the crack width (in mm) within the constant moment region for five load steps is displayed in Figure 63. The atypical cracking pattern on both sides of the beam was likely caused by out-of-plane deformation during testing as was already discussed in section 5.2.1.1. Eventually the reference beam failed at a load of 98.3 kN with very large localised cracks (Figure 64). The peak load F_{max}, the load $F_{0.3}$ and deflection $u_{0.3}$ at a maximum crack width of 0.3 mm and midspan deflection at peak load u_{max}, number of cracks within constant moment region at peak load n_{cr}, average crack spacing at peak load $\bar{s}_{cr}$ and maximum crack width at peak load CW for the control beam CB1 are summarized in Table 14.

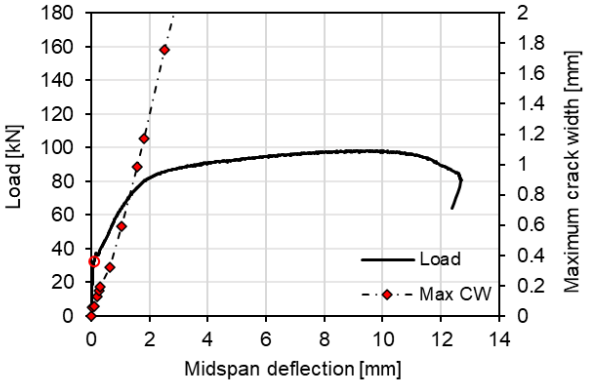

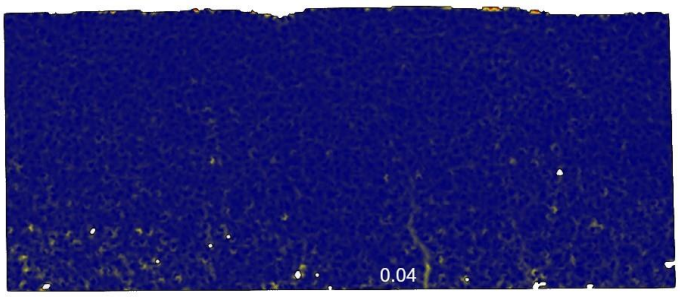

32.6 kN

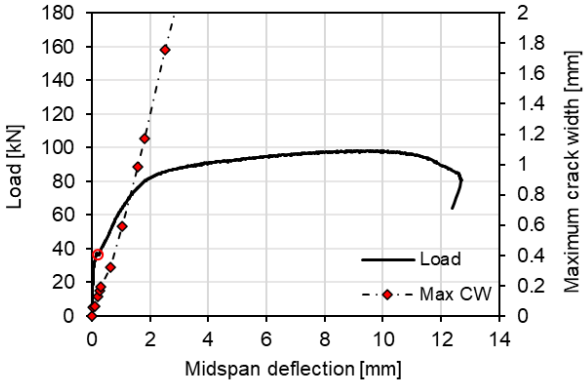

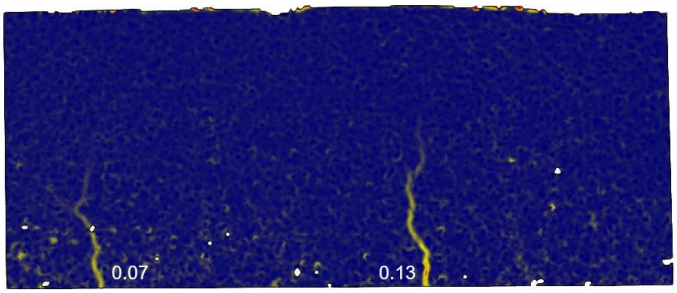

36.3 kN

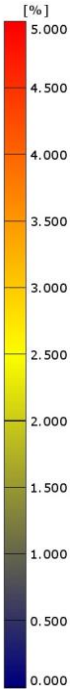

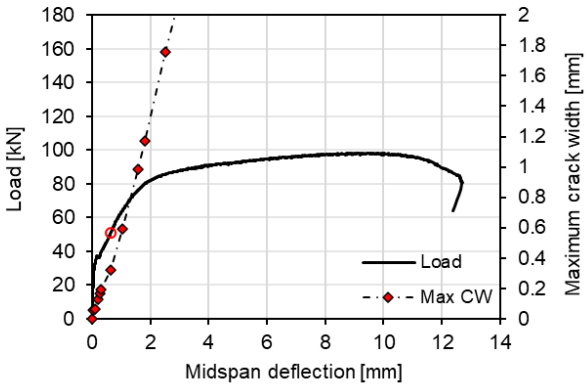

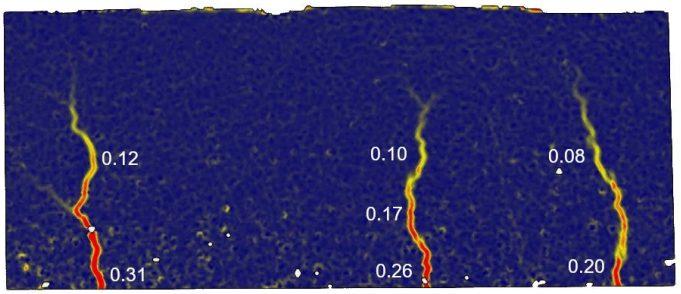

51.0 kN

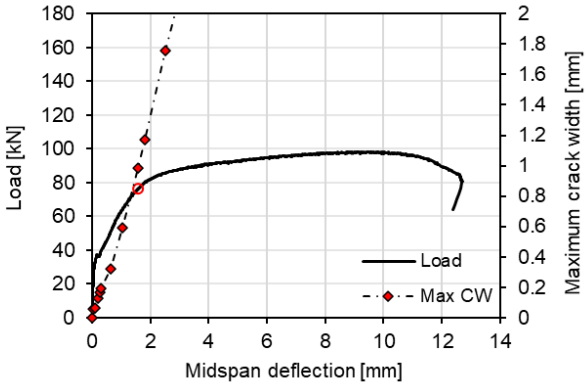

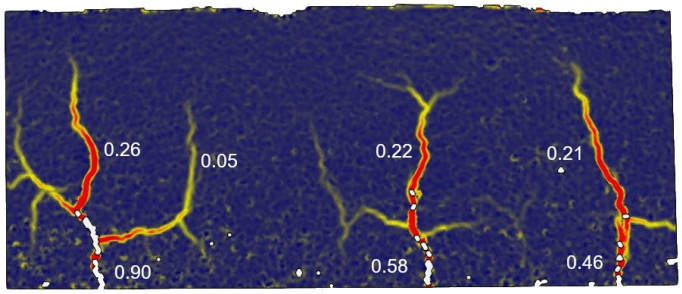

76.2 kN

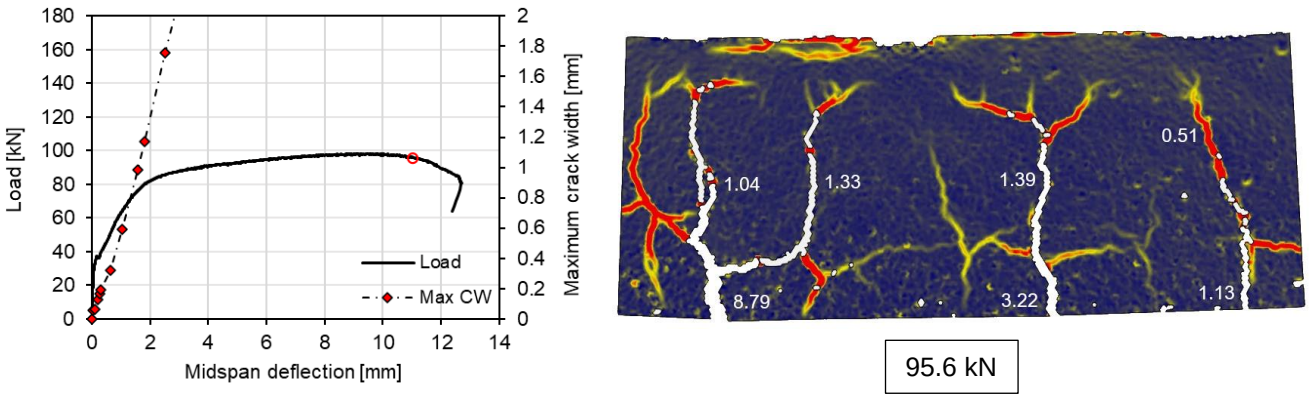

Figure 63. Cracking pattern of CB1 at several load steps.

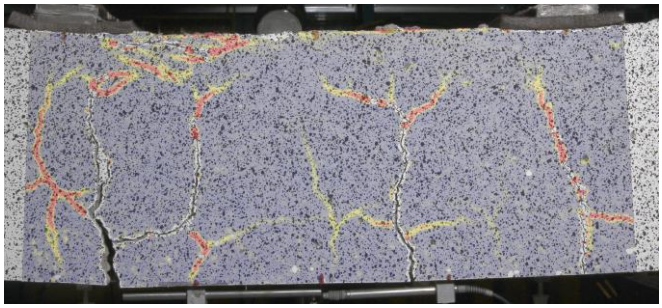

Figure 64. Localization of the dominant crack in CB1.

Property	Value	
F_{max}	98.3	kN
$F_{0.3}$	48.3	kN
$u_{0.3}$	0.59	mm
u_{max}	9.73	mm
n_{cr}	3	
$\bar{s}_{cr}$	183.6	mm
CW	7.73	mm

Table 14. Crack pattern properties of CB1.

Hybrid beam with transverse shear keys

The propagation of cracks and the corresponding crack width along section 1 for six load steps are displayed in Figure 65. The number of cracks in the U-shaped formwork are too many to be labelled individually, so the cracks with a crack width larger than 0.01 mm are presented in a scatter plot for every load step. The crack pattern of HBT1 features multiple fine flexural cracks which seem to localise in bundles of cracks. Initial flexural cracks developed at a load step of 38.7 kN (Figure 63). Those cracks further localised when the load increased. At a load of 98.4 kN more flexural cracks formed in between existing cracks. At a load of 129.8 kN, after the reinforcement has yielded, cracks localised even further. The beam failed with a large localised crack in the constant moment region (Figure 66). The crack

spacing and maximum crack width of HBT1 at peak load were only 12.6 mm and 1.88 mm respectively, which is a lot lower compared to the reference beam (Table 15).

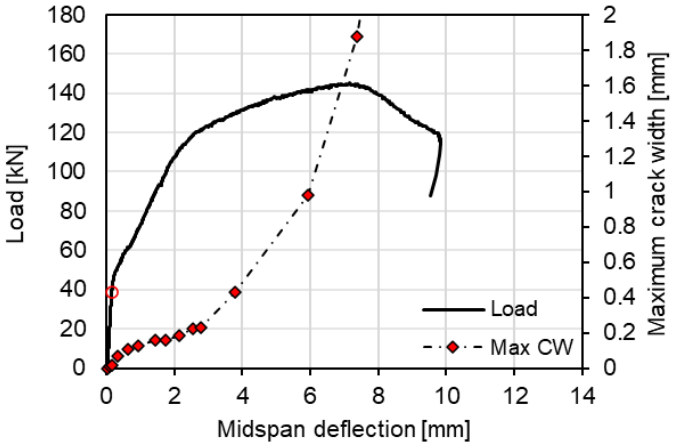
Load [kN]
Maximum crack width [mm]
Midspan deflection [mm]
Load
Max CW

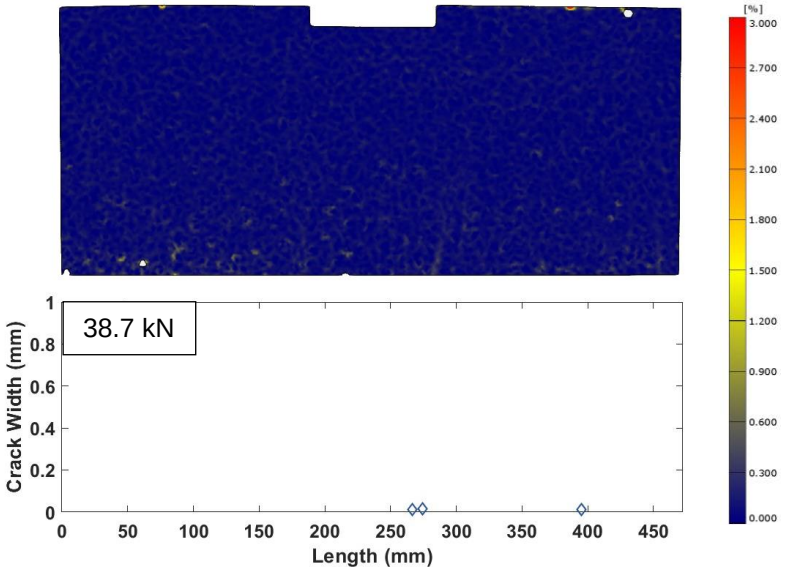
38.7 kN
Crack Width (mm)
Length (mm)
[%]

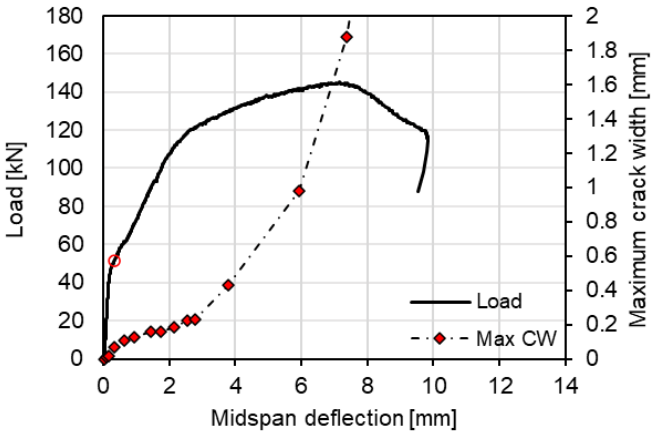
Load [kN]
Maximum crack width [mm]
Midspan deflection [mm]
Load
Max CW

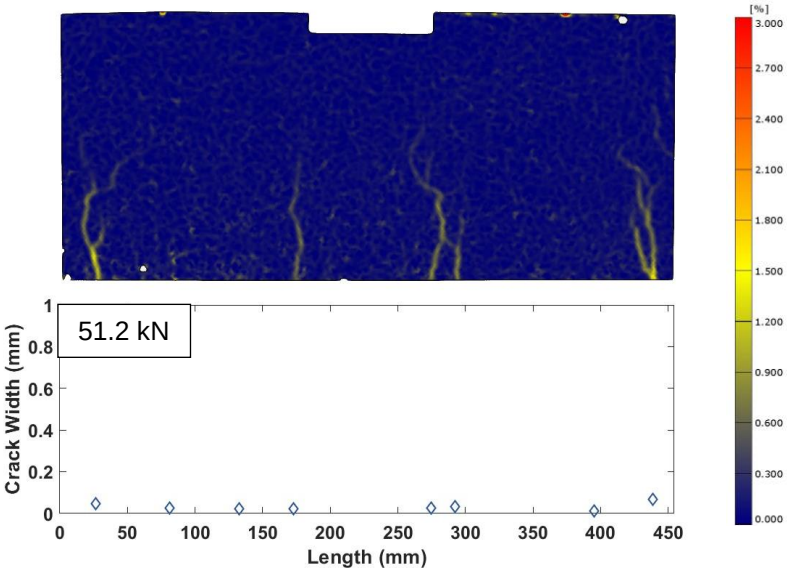
51.2 kN
Crack Width (mm)
Length (mm)
[%]

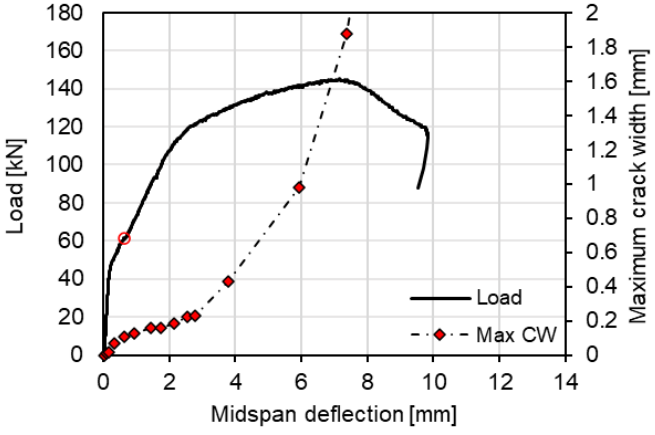
Load [kN]
Maximum crack width [mm]
Midspan deflection [mm]
Load
Max CW

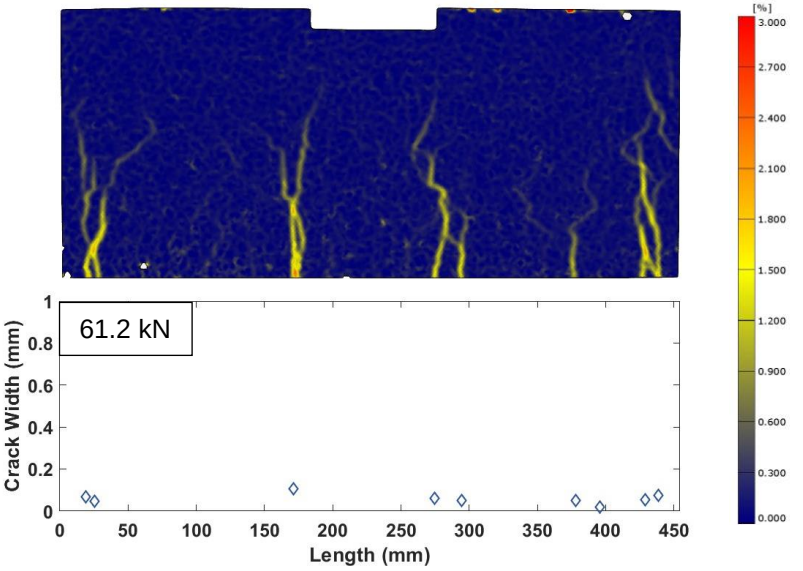
61.2 kN
Crack Width (mm)
Length (mm)
[%]

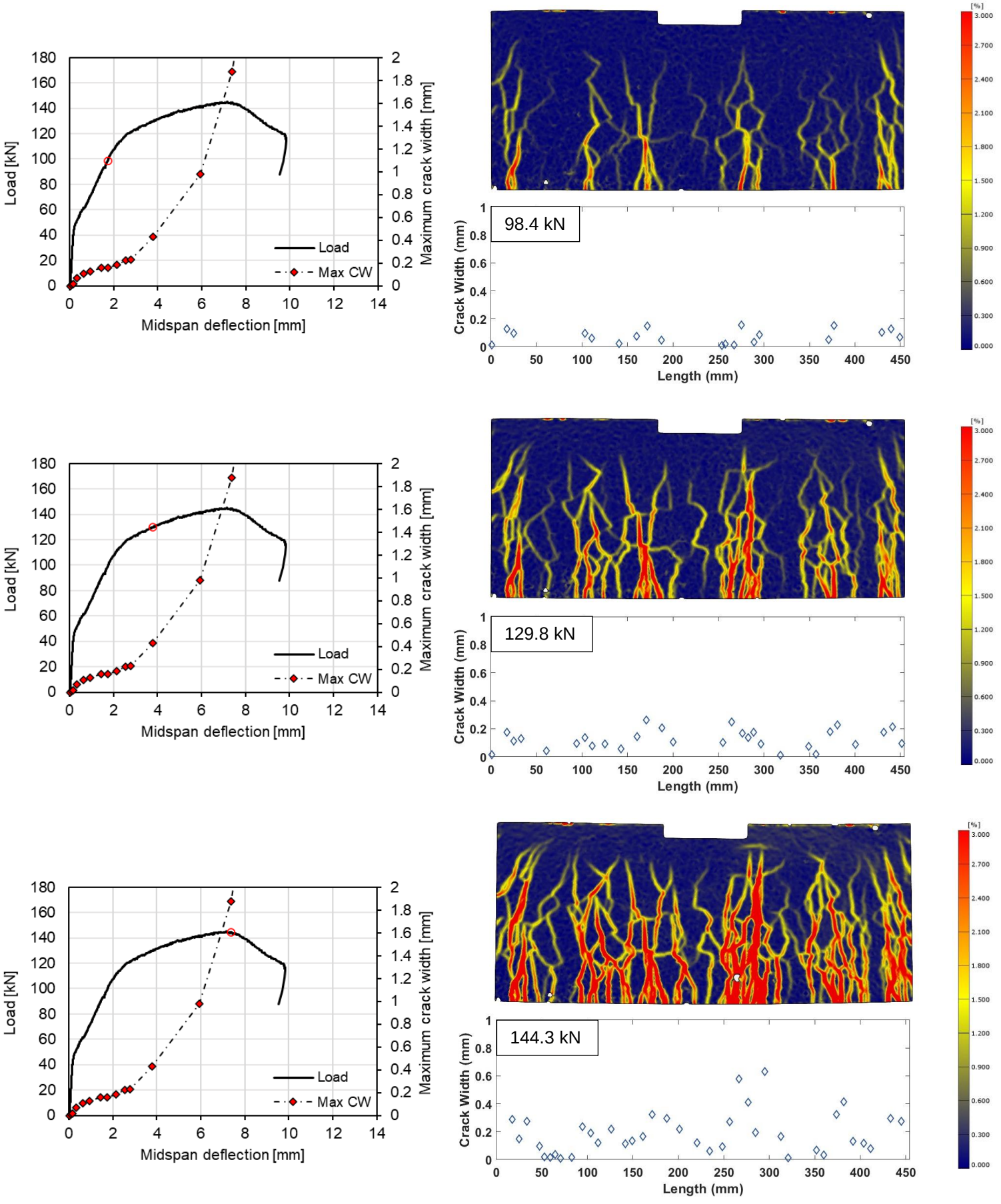

Figure 65. Cracking pattern HBT1 at several load steps.

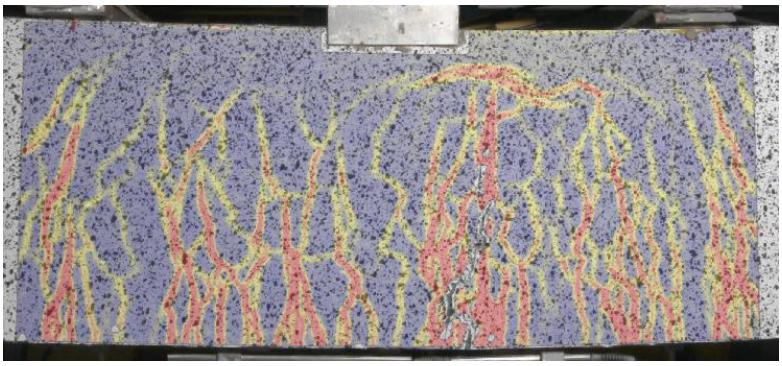

Figure 66. Localization of the dominant crack in HBT1.

Property	Value	
F_{max}	145.1	kN
$F_{0.3}$	124.7	kN
$u_{0.3}$	3.14	mm
u_{max}	7.17	mm
n_{cr}	35	
$\bar{s}_{cr}$	12.6	mm
CW	1.88	mm

Table 15. Crack pattern properties of HBT1 at peak load.

Not all cracks were able to be captured with the DIC due to the quality of the DIC pattern (Figure 67). The cracks were either too small (smaller or equal to 0.01 mm) or very close to each other. In addition, it should be noted that a few scatter points in the scatter plots of the crack width do not coincide with a crack due to strain caused by noise. An attempt was made to try and optimize the DIC results by choosing an appropriate cracking strain threshold.

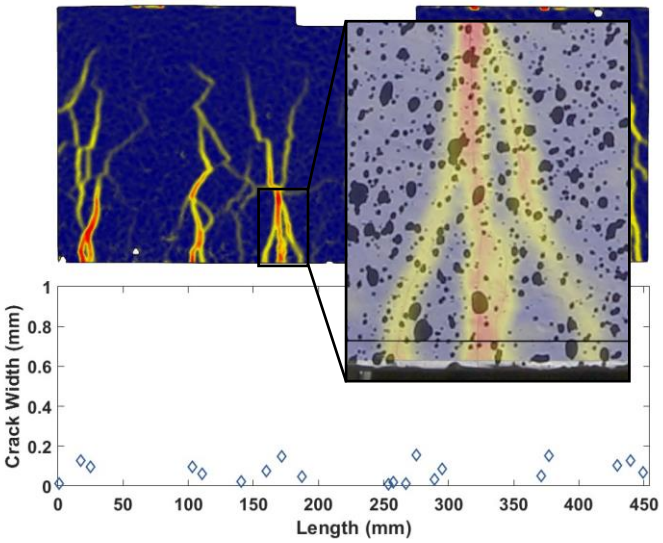

Figure 67. Precision DIC results.

Hybrid beam with transverse and longitudinal shear keys

The cracking pattern of the hybrid beam with transverse and longitudinal shear keys HTBL1 is very similar to the hybrid beam with only transverse shear keys HBT1. The large flexural cracks in the concrete turn into multiple fine cracks in the SHCC. The beam failed due to a large localized crack in the constant moment region (Figure 69).

The DIC analysis was carried out with two different combinations of facet size and point distance, a similar one as HBT1 (30px,16px) and more refined (20 px,10px). The propagation of cracks and the corresponding crack width along section 1 for both facet sizes and point distances are displayed in Figure 68. The facet size and point distance influence the number of cracks and crack width. A facet size and point distance of (30px, 16px) tend to overestimate the crack width at some locations compared to (20px, 10px) (Figure 68). At those locations, the DIC software is unable to recognize multiple strain peaks and instead, uses one strain peak for multiple cracks in case of a less refined facet size and point distance. Hence, a facet size and point distance of (30px, 16px) underestimates the number of cracks and overestimates the crack spacing compared to (20px, 10px) (Table 16). However, refinement of the facet size and point distance results in more noise (unjustly labelled cracks). Hence, the real number of cracks likely lies some somewhere in between.

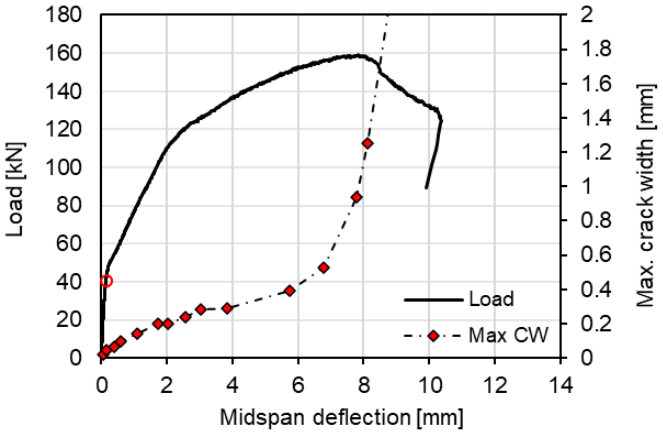
Load [kN]
Max. crack width [mm]
Midspan deflection [mm]
Load
Max CW

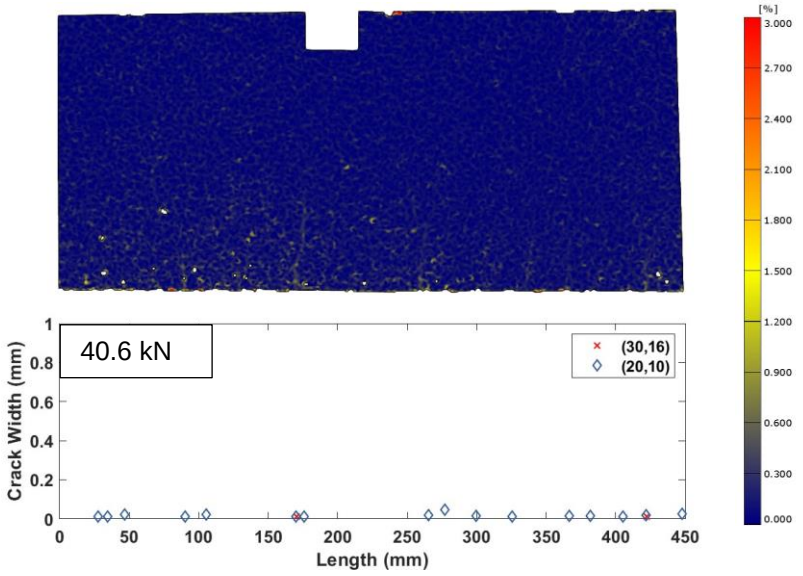
40.6 kN
Crack Width (mm)
Length (mm)
(30,16)
(20,10)
[%]

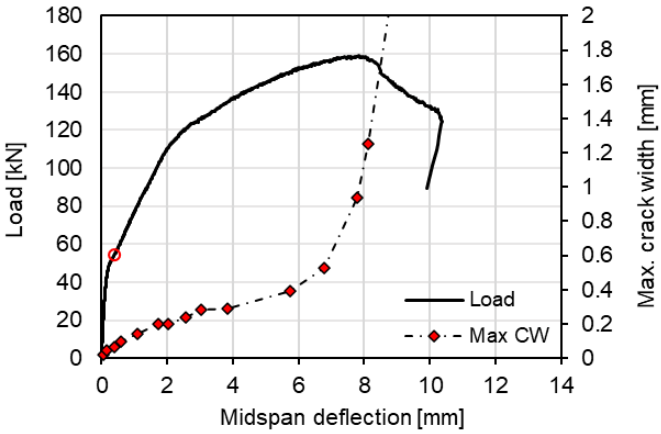
Load [kN]
Max. crack width [mm]
Midspan deflection [mm]
Load
Max CW

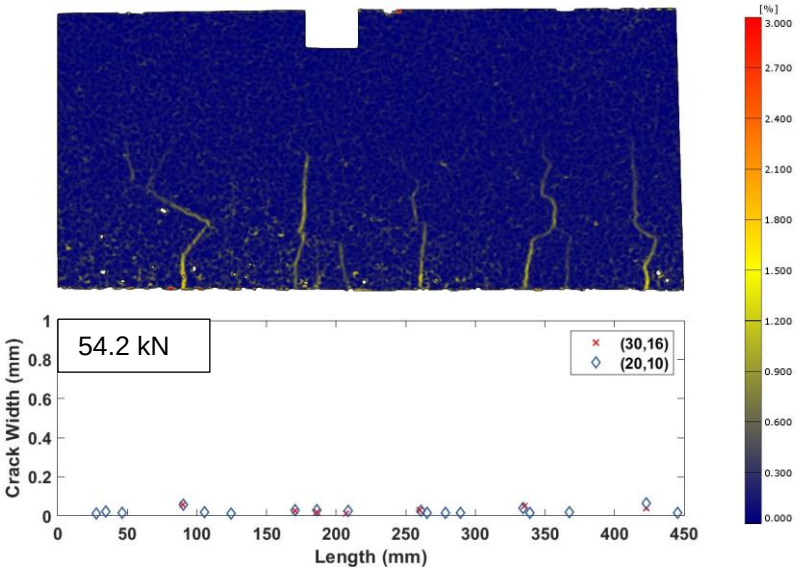
54.2 kN
Crack Width (mm)
Length (mm)
(30,16)
(20,10)
[%]

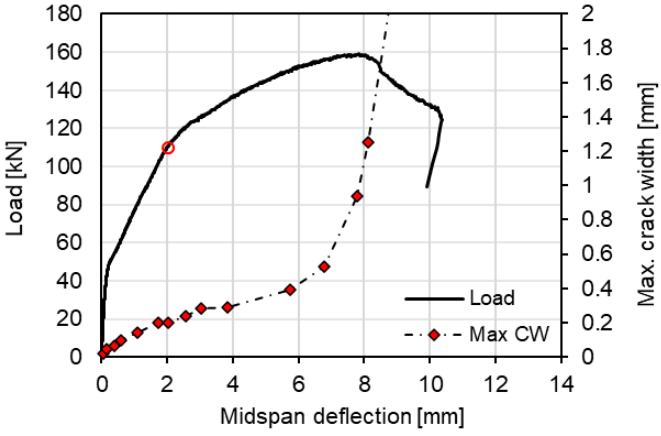
Load [kN]
Max. crack width [mm]
Midspan deflection [mm]
Load
Max CW

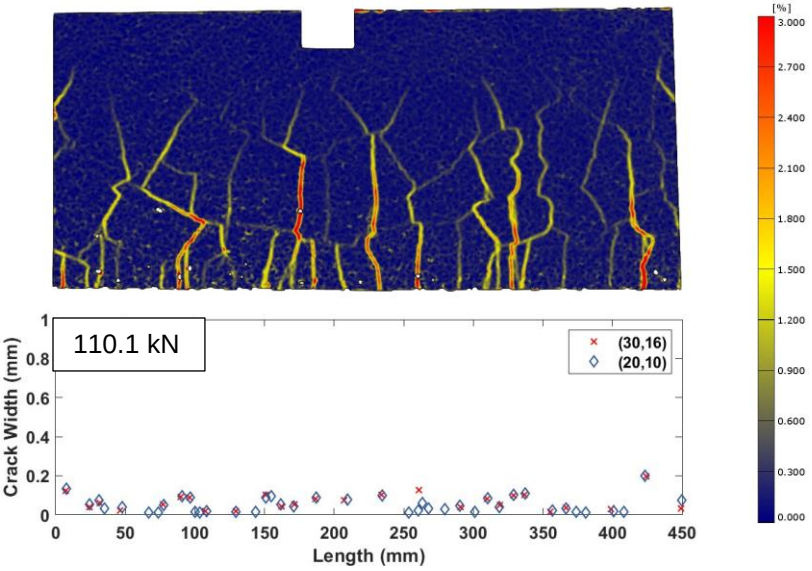
110.1 kN
Crack Width (mm)
Length (mm)
(30,16)
(20,10)
[%]

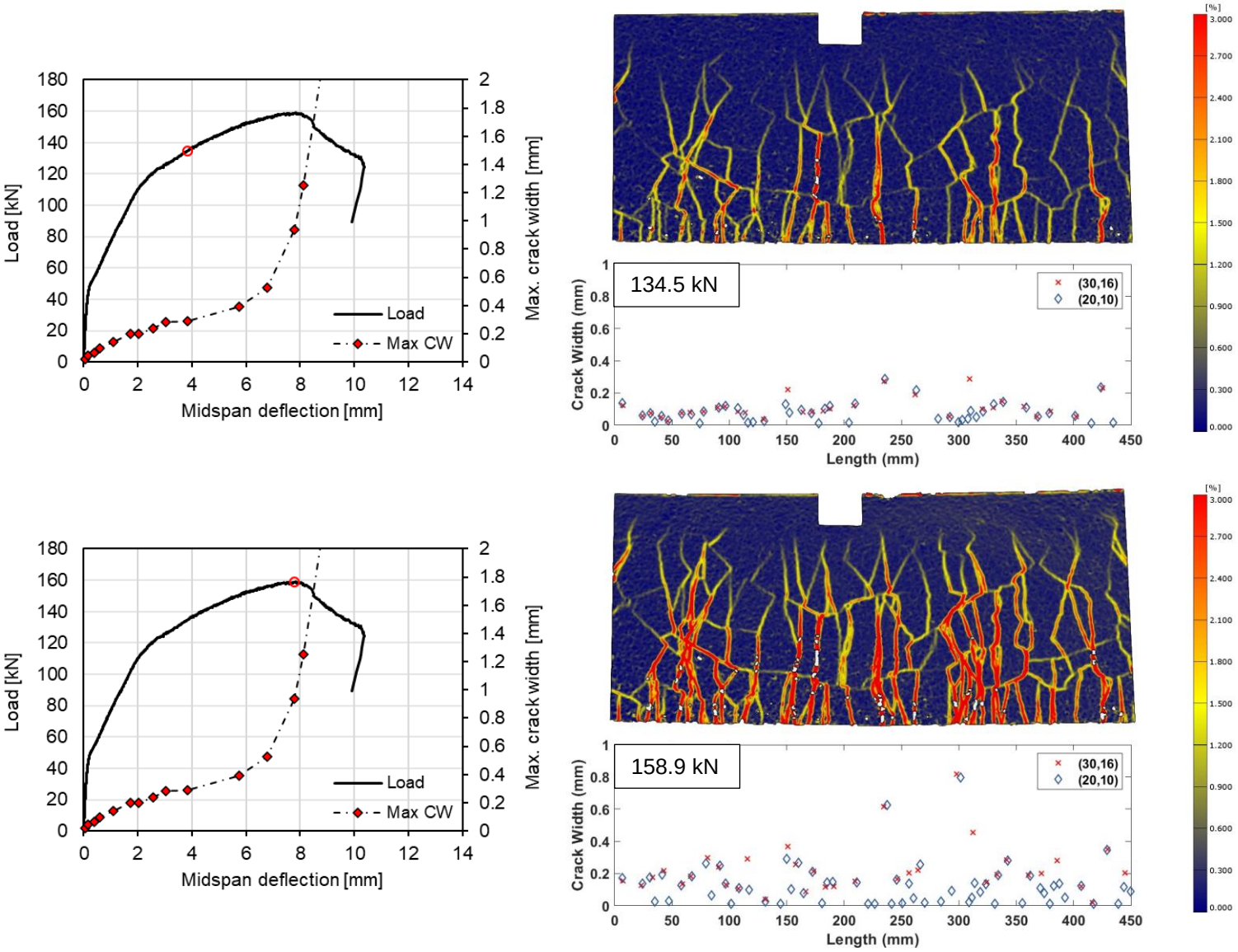

Figure 68. Cracking pattern of HBTL1 at several load steps.

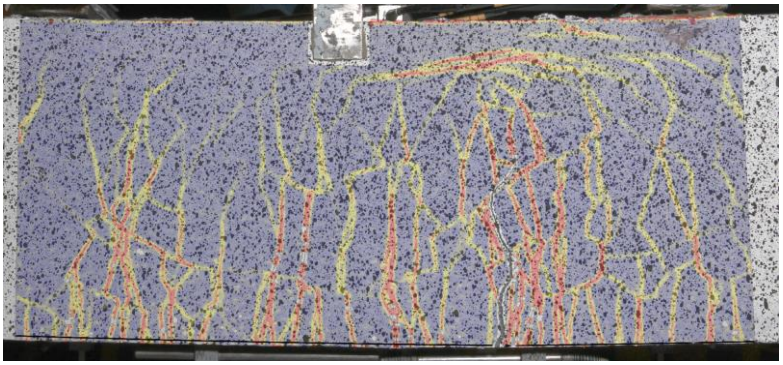

Figure 69. Dominant crack at failure of HBTL1.

Property	Value	
F_{max}	159.1	kN
$F_{0.3}$	137.3	kN
$u_{0.3}$	4.03	mm
u_{max}	7.84	mm
$n_{cr,(30,16)}$	34	
$n_{cr,(20,10)}$	54	
$\bar{s}_{cr,(30,16)}$	12.31	mm
$\bar{s}_{cr,(20,10)}$	7.90	mm
CW	0.94	mm

Table 16. Crack pattern properties of HBTL1.

Hybrid beam with 3D printed formwork

The cracking behaviour of the hybrid beam with a 3D printed SHCC formwork displayed multiple fine cracks (Figure 70). The failure mechanism consisted of a localised flexural crack at midspan (Figure 71). A scatter plot is used to visualize the crack width along section 1 and section 2, which are located 7.5 mm and 25 mm above the bottom, respectively. Interestingly, at every load step, the number of cracks in section 2, is larger than in section 1. At peak load, the number of cracks in section 1 was 46, whilst in section 2 around 60 cracks were captured by DIC (Table 17). The same was not observed in the hybrid beams with a precast SHCC formwork. Presumably, the weaker interface of the printed filaments and concrete resulted in a longer debonding length, more SHCC activation, lower crack spacing and crack width along section 2 in the hybrid beam with 3D printed formwork as compared to an interface with mechanical interlock.

Although the surface of the 3D printed formwork was not flat, which normally causes noise in the DIC data, however the DIC results looked accurate enough.

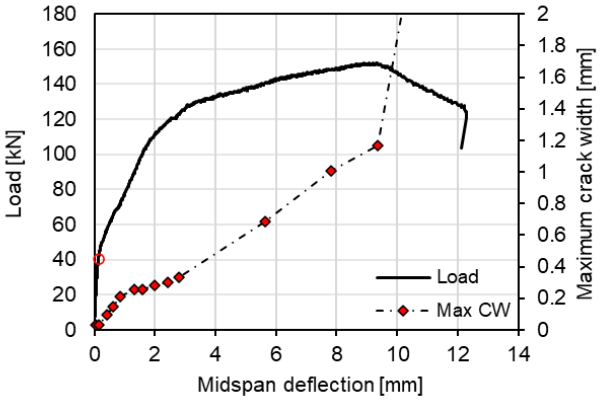
Load [kN]
Maximum crack width [mm]
Midspan deflection [mm]
Load
Max CW

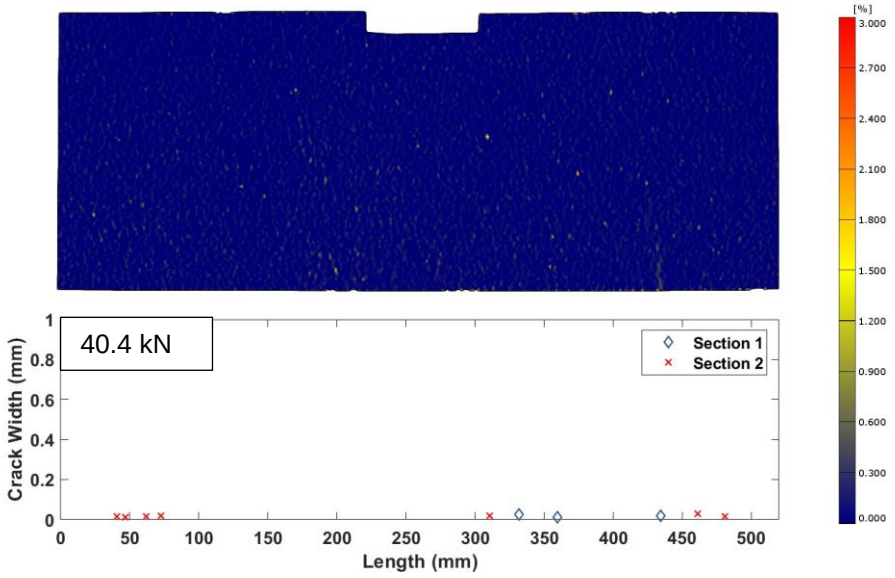
40.4 kN
Crack Width (mm)
Length (mm)
Section 1
Section 2
[%]

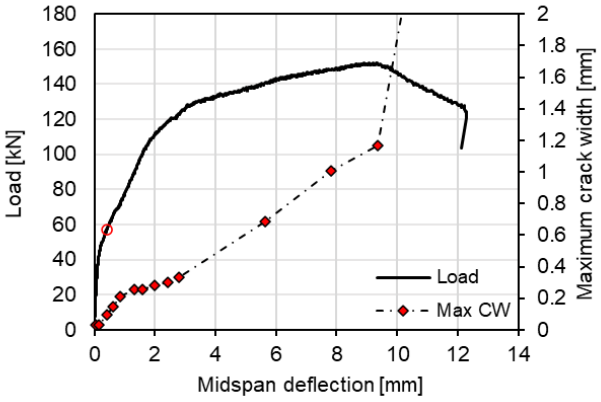
Load [kN]
Maximum crack width [mm]
Midspan deflection [mm]
Load
Max CW

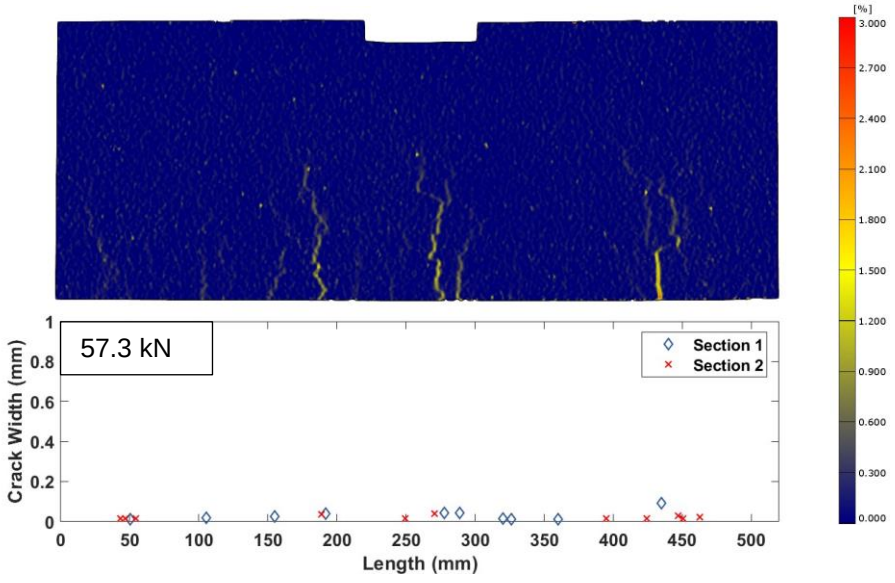
57.3 kN
Crack Width (mm)
Length (mm)
Section 1
Section 2
[%]

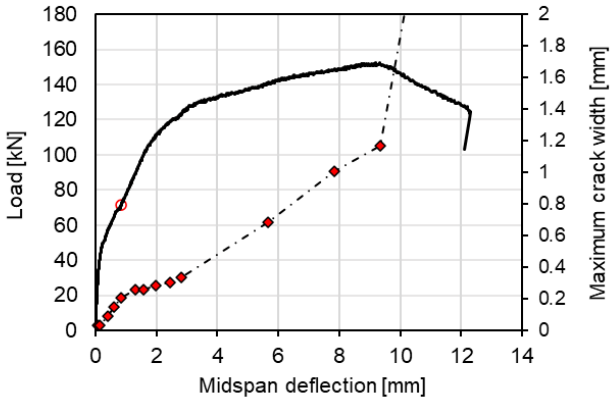
Load [kN]
Maximum crack width [mm]
Midspan deflection [mm]

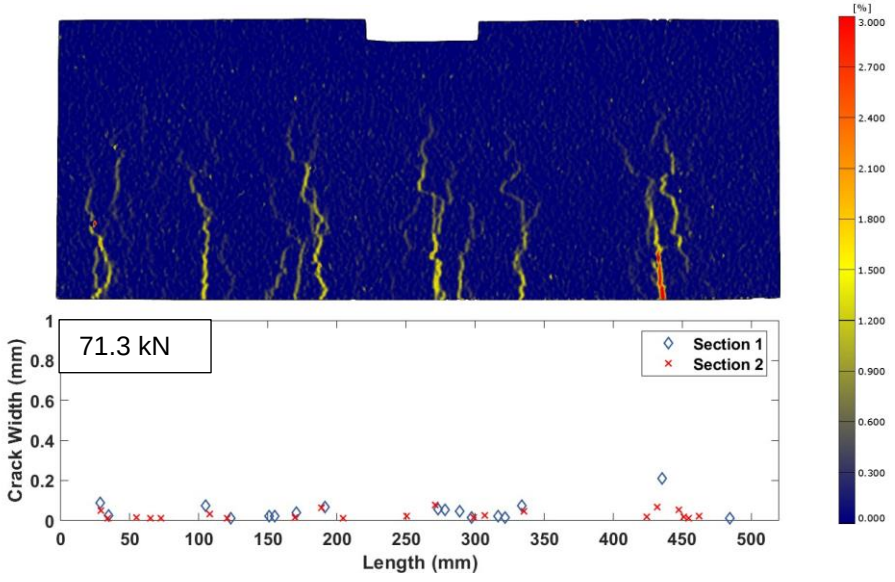
71.3 kN
Crack Width (mm)
Length (mm)
Section 1
Section 2
[%]

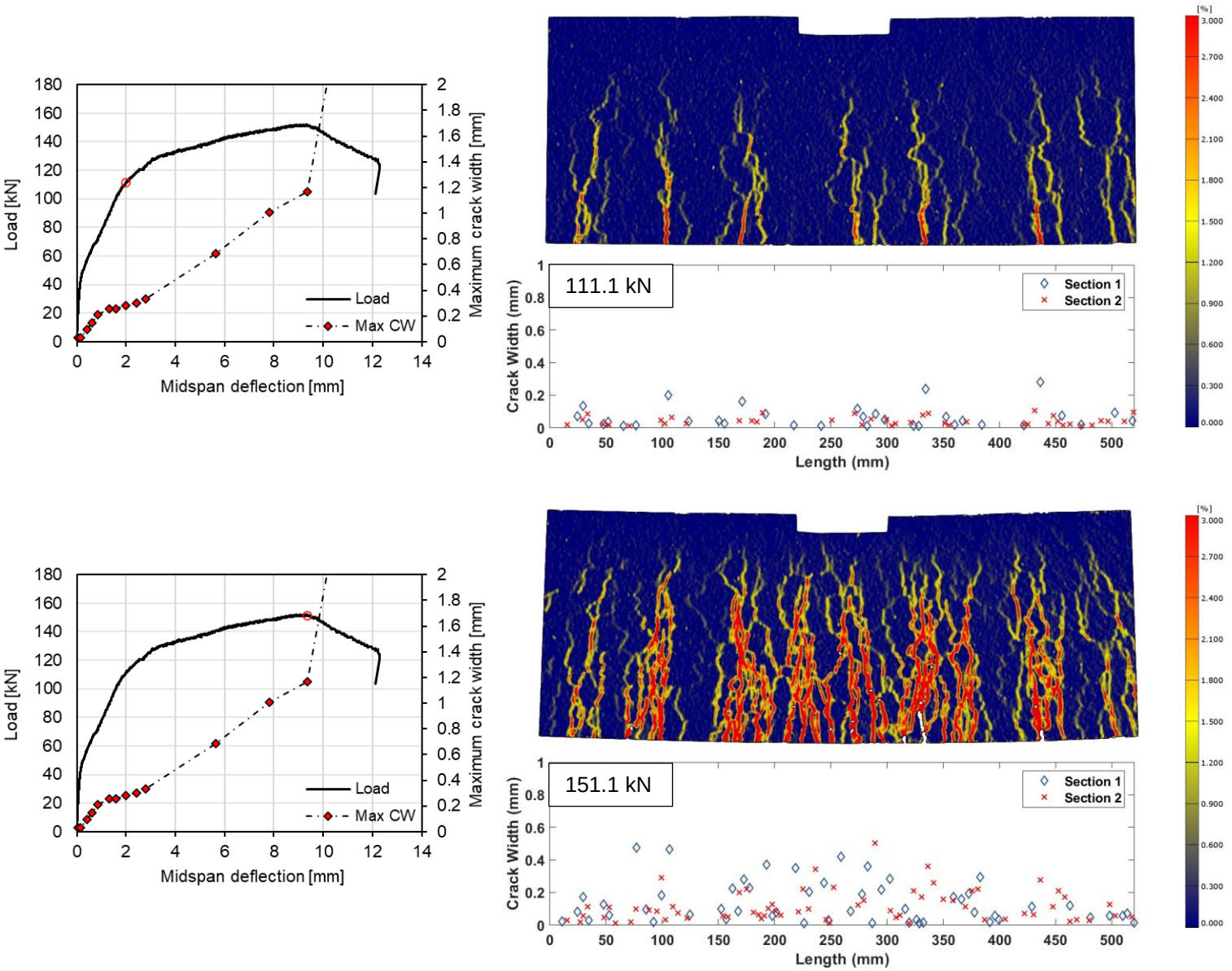

Figure 70. Cracking pattern of 3DHB1 at several load steps.

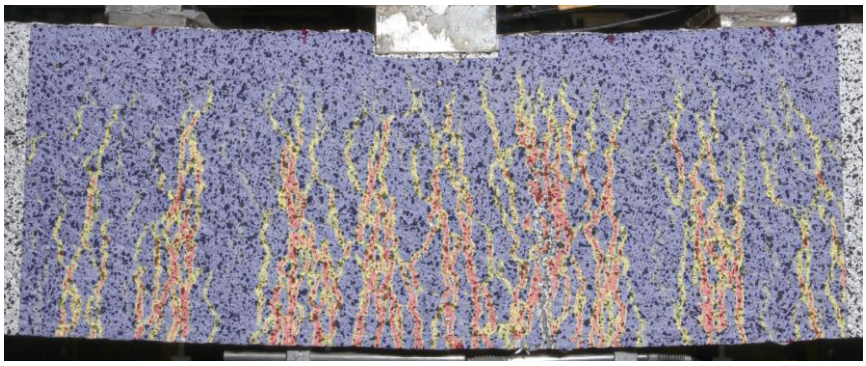

Figure 71. Dominant crack at failure in 3DHB1.

Property	Value	
F_{max}	152.4	kN
$F_{0.3}$	119.0	kN
$u_{0.3}$	2.43	mm
u_{max}	9.19	mm
n_{cr}	46	
$\bar{s}_{cr}$	9.00	mm
CW	1.17	mm

Table 17. Crack pattern properties of 3DHB1 at section 1 at peak load.

5.2.1.3. Crack width

The Eurocode [1] states that the maximum allowable crack width in SLS is 0.3 mm under quasi-permanent load for every exposure class, except X0 and XC1. Often it is the case that crack width control is critical in the design of reinforced concrete structures. Therefore, it is of interest to determine the maximum crack width in the beams at different load steps. The strain in longitudinal direction ε_{xx} and relative displacements evaluated at different sides, sections and points were extracted from GOM Correlate and used as input in a MATLAB code to calculate the number of cracks and crack width. At some load steps GOM does not recognize data points as a result of crack formation. Therefore, it is not possible to determine the strain and relative displacement of these points. In those circumstances, extra data points are manually added near the crack and evaluated separately. In this way, the maximum crack width at several load steps were determined for all the beams and plotted against the midspan deflection (Figure 72). The load-deflection response and maximum crack width are also plotted in one graph (Figure 73a). The blue dotted line represents the load level at which the maximum crack width has reached 0.3 mm. The hybrid beams show superior crack width control compared to the control beam, i.e. crack widths in the SHCC exceed the 0.3 mm limit at a higher load. The maximum crack width was lower in the hybrid beams than the control beam for all load steps. Also, the maximum crack width in CB1 tends to increase rapidly in contrast to the hybrid beams where the maximum crack width increases very slowly before yielding of the reinforcement, indicating the activation of SHCC (Figure 73b). After the reinforcement has yielded, the crack width become too large for the fibres in the SHCC to bridge the cracks. As a result, a very steep increase in crack width is observed after yielding of the reinforcement.

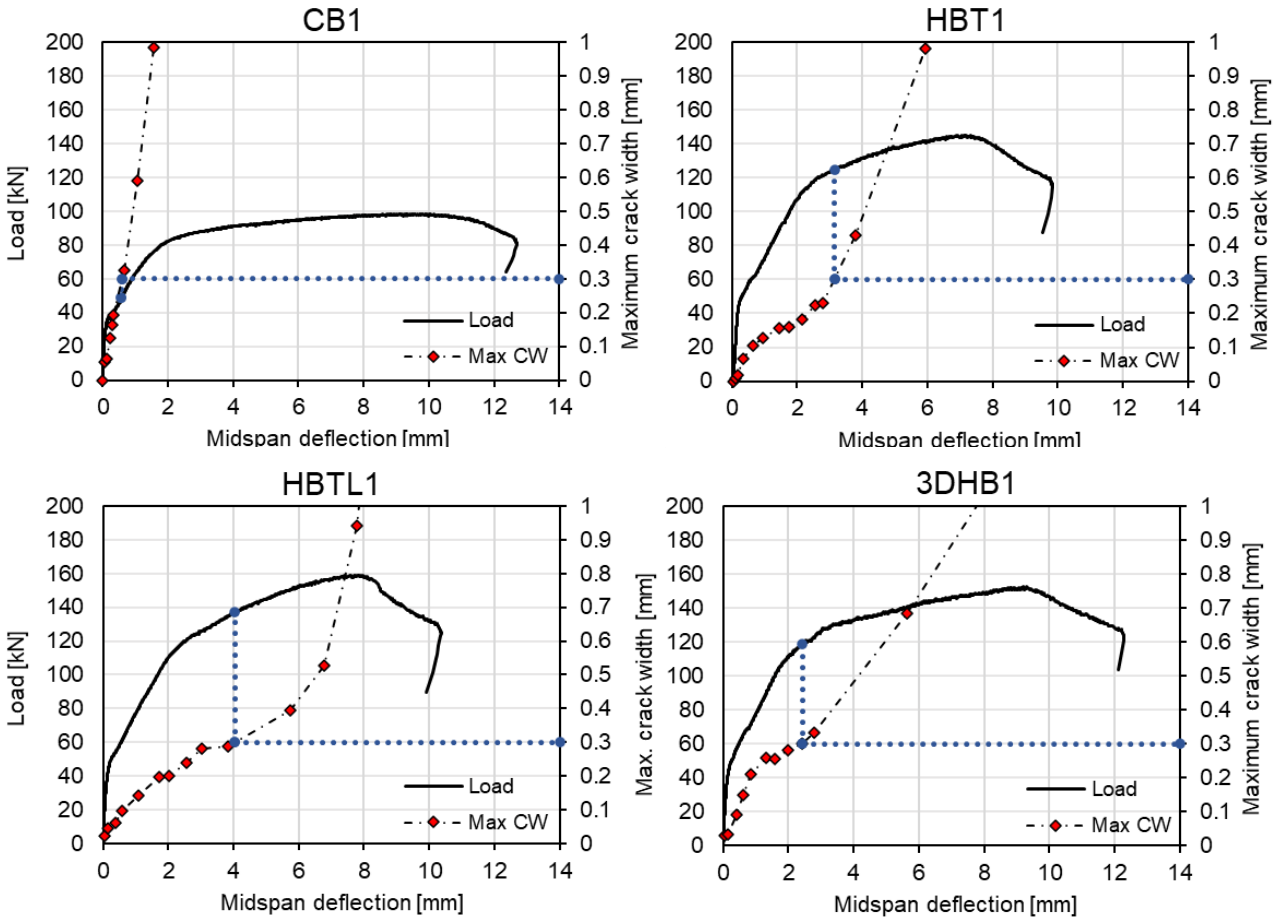

Figure 72. Load-deflection curve and max. crack width response

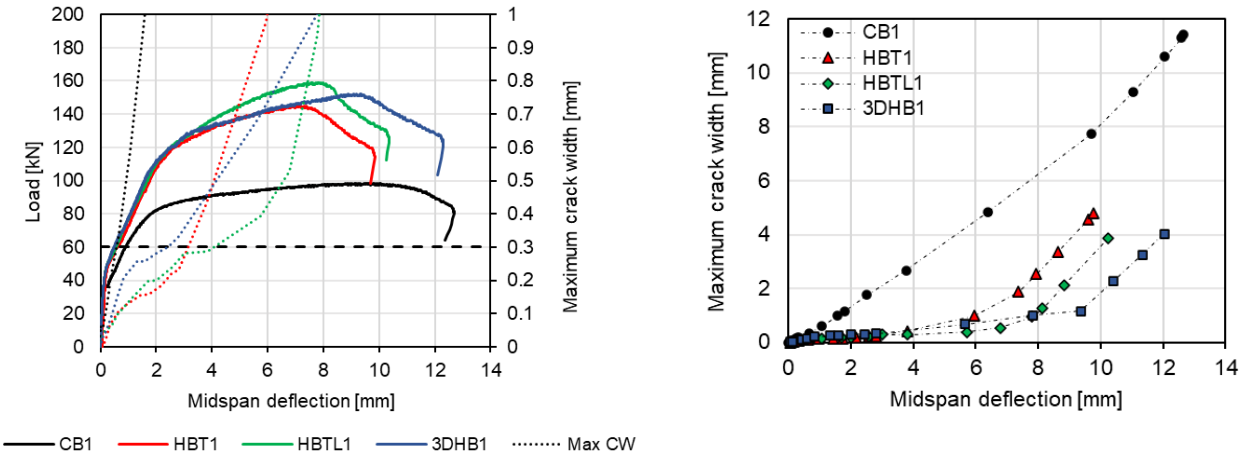

(a) (b)

Figure 73. Load-deflection and max. crack width response (a) and max. crack width vs. midspan deflection (b) of all beams.

The maximum crack width between every load step was linearly interpolated in order to determine the load which corresponds to a maximum crack width of 0.3 mm $F_{0.3}$. SHCC seem to have a larger influence on $F_{0.3}$ and $u_{0.3}$ compared to F_{max} and u_{max} (Table 18). This is because the largest contribution to the bending resistance of RC structures comes from the reinforcement. The larger $F_{0.3}$ and $u_{0.3}$ of the hybrid beams compared to the reference beam is a result of the SHCC formwork and indicates that the SHCC improves the crack width control. The crack width threshold of 0.3 mm was reached somewhere along section 1 in all the beams. The crack width of 0.3 mm in the hybrid beam with a printed SHCC formwork localised at a lower load compared to the hybrid beams with a precast SHCC formwork. It is believed that the inferior tensile properties of the printed SHCC (Table 11) explains

	$F_{0.3}$ (kN)	F_{max} (kN)	$u_{0.3}$ (mm)	u_{max} (mm)
CB1	48.4	98.3	0.59	9.73
HBT1	124.6	145.1	3.14	7.17
HBTL1	137.3	159.1	4.03	7.84
3DHB1	119.0	152.4	2.43	9.19

Table 18. Several load and deflection values at specific points.

this difference. In all the hybrid beams the crack width localised either at or after yielding of the reinforcement, unlike the reference beam (Figure 74b). The crack width of 0.3 mm localised way before yielding of the reinforcement in the reference beam CB1. The same amount of reinforcement in the hybrid beams was sufficient to reach the yield point of the reinforcement before a crack of 0.3 mm localised. In the reference beam, the reinforcement could not reach the yield point before a crack of 0.3 mm localised. Hence, in the SHCC-RC hybrid beams, the reinforcement is used more efficiently than in the concrete beam to control the maximum crack width.

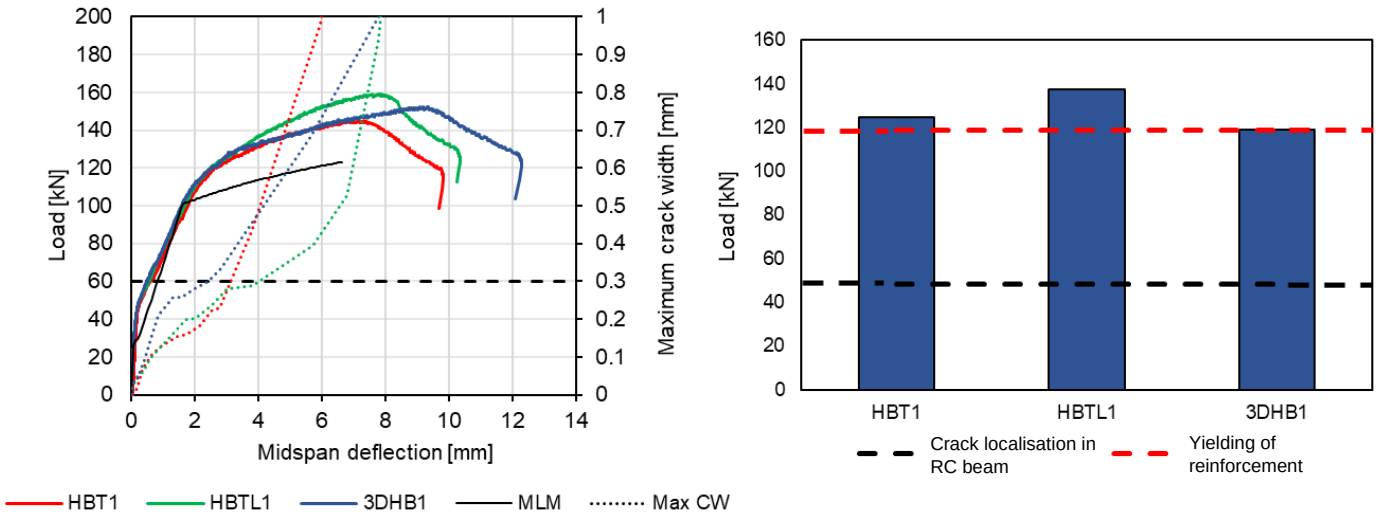

Figure 74. Load-deflection and crack width response (a) with the load at which the crack width of 0.3 mm localised (b). The red dashed line is the load at yielding of the reinforcement in the hybrid beams and the black dashed line corresponds $F_{0.3}$ of CB1.

It was mentioned in section 5.2.1.1 that the load-deflection curve of the reference beam CB1 is probably not accurate. Therefore, the crack width data of CB1 is compared with the MLM and some reference studies. This is further elaborated in section 7.1.2.

5.2.1.4. Delamination

The opening between the SHCC and concrete was measured during testing with LVDTs. The position of the LVDTs is shown in Figure 48 and Figure 49. The data from LVDT03 and LVDT04 show that there was no significant debonding between the SHCC and concrete in the top of the beam at midspan. The debonding of SHCC and concrete up to the peak load was very small (Figure 75). The hybrid beam with 3D printed formwork 3DHB1 opened 0.2 mm, whilst the opening in HBT1 and HBTL1 opened less than 0.1 mm. This may indicate that the printed SHCC-concrete interface can be considered weaker compared to an interface with mechanical interlock. There was no significant debonding in all the hybrid beams.

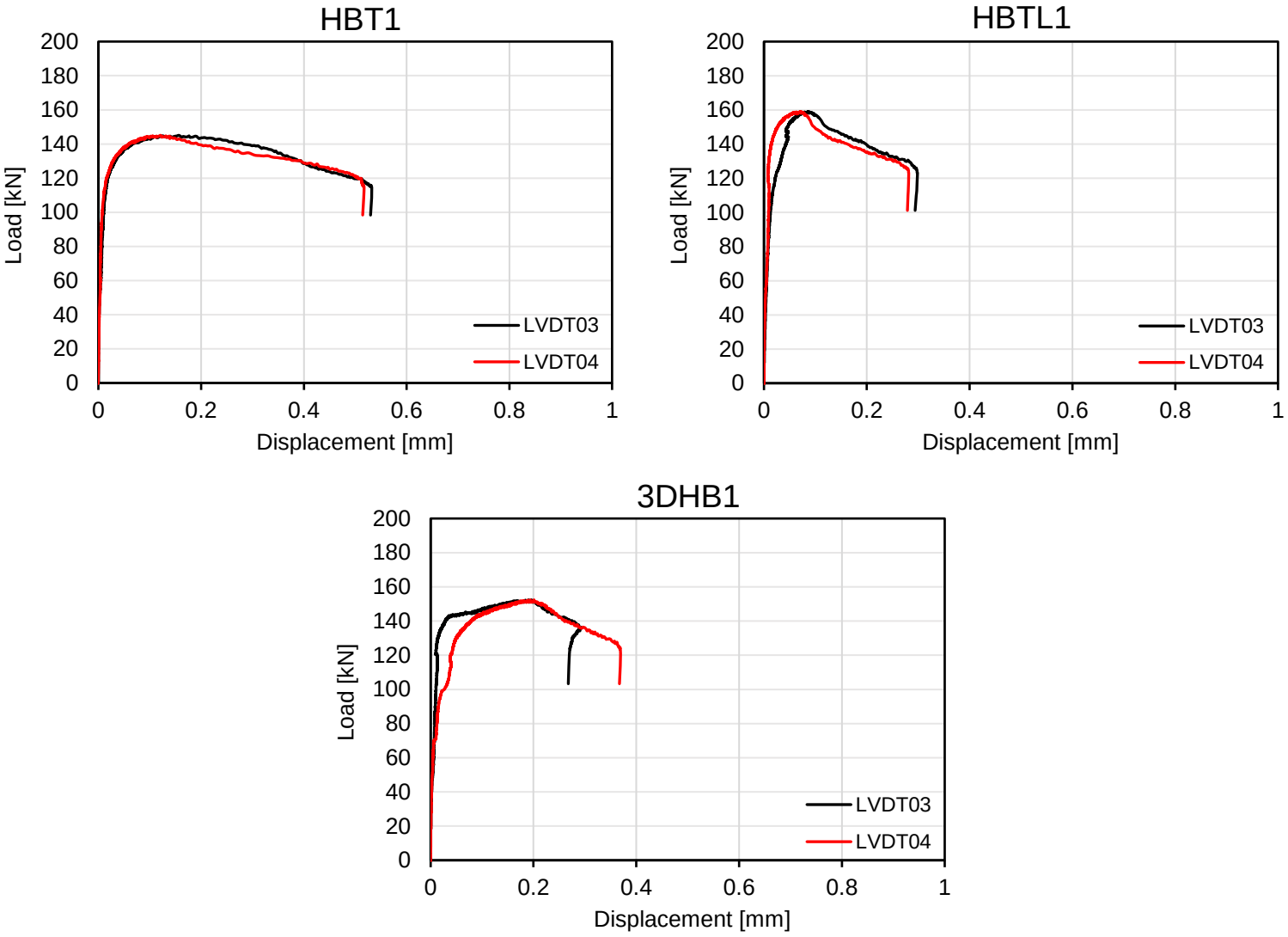

Figure 75. Opening between SHCC and concrete.

5.2.2 Shear

5.2.2.1. Load vs midspan deflection

A three-point bending test was carried out on four beams without shear reinforcement: a control beam (Figure 34), hybrid beam with a precast SHCC U-shaped formwork and transverse shear keys (Figure 35), hybrid beam with a precast SHCC U-shaped formwork and transverse as well as longitudinal shear keys (Figure 36), and a hybrid beam with a printed SHCC U-shaped formwork (Figure 32). The dimensions and reinforcement layout of the test setup are mentioned in Figure 33. Initially, the beams deform linear elastically (Figure 76). After the formation of the first few flexural cracks, the beam stiffness reduced which led to a drop in the slope of the load-deflection curve. This is followed by a further reduction in stiffness with formation of flexure-shear cracks. The post-peak response of the control beam is characterised by a sudden drop in load whilst the hybrid beams all behaved more ductile. Besides, the stiffness in all hybrid beams reduced at a lower rate than the control beam after the formation of flexural cracks. It is a direct result of the strain-hardening characteristic of SHCC. In addition, the peak load F_{max} of HBT2, HBTL2 and 3DHB2 are 0%, 9.5% and 20.1% higher than the peak load of the control beam, respectively (Table 19). Despite the negligible difference in peak load of CB2 and HBT2, HBT2 exhibited a larger energy absorption capacity E_{abs}, which is defined as the area under the load-deflection curve, until 85% of the post-peak load (Table 19). This is a consequence of the crack bridging force in the hybrid beams which provide additional shear resistance, both after the appearance of shear cracks and after ultimate failure. Finally, the force at which the first diagonal/shear crack occurs $F_{diagonal}$ tend to be higher for the hybrid beams compared to CB1 (Table 19), which is probably the result of the higher compressive strength of SHCC. The force at which the first flexural crack occurs $F_{flexure}$ is comparable for all the beams (Table 19).

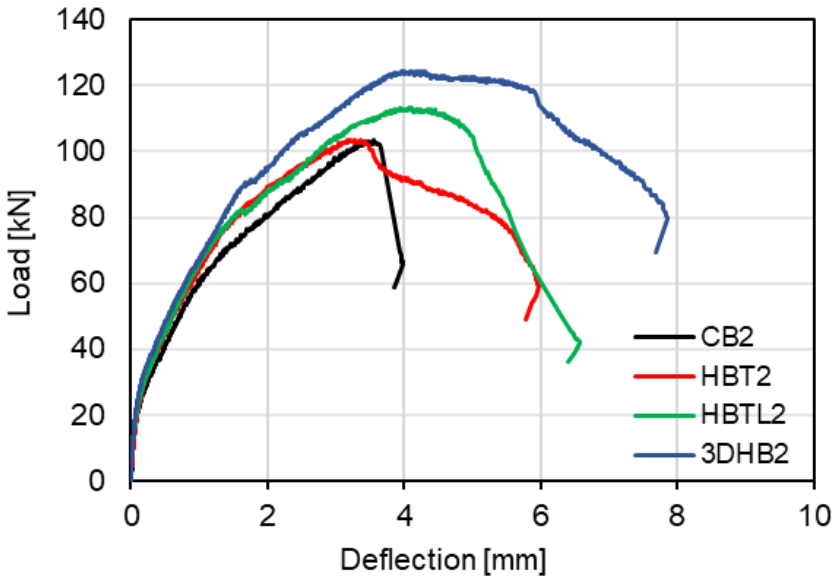

Figure 76. Load vs. midspan deflection of the shear test.

	$F_{flexure}$	$F_{diagonal}$	F_{max}	$u_{diagonal}$	u_{max}	E_{abs} (J)
CB2	16.0	38.9	103.7	0.44	3.55	530.8
HBT2	17.5	40.2	103.7	0.40	3.28	672.5
HBTL2	20.2	43.7	113.5	0.46	4.09	1096.2
3DHB2	22.7	48.5	124.5	0.51	3.99	1382.7

Table 19. Results shear test.

5.2.2.2. Shear ductility

Post-cracking shear ductility is a property which refers to the ability of a beam to continue deforming after the initiation of the dominant shear crack. It can be used to measure the capacity of a beam to resist sudden shear failure and sustain large deformations without collapsing. The post-cracking shear ductility of concrete beams can be represented in terms of a ductility factor (DF) or shear resistance factor (SRF) according to previous research [102, 103]:

$$DF = \frac{u_{max}}{u_{diagonal}}$$

$$SRF = \frac{F_{max}}{F_{diagonal}}$$

u_{max} is the midspan deflection at peak load and $u_{diagonal}$ is the midspan deflection at which the dominant shear crack initiated. In this research a different definition is used, because the SHCC has a pronounced effect on the deformation capacity. Instead of F_{max} and u_{max}, 85% of the post-peak load ($F_{85\%}$) is used (Table 20). The SRF of all the hybrid beams are similar to the reference beam CB2 (Table 20) Meanwhile, the hybrid beams have a larger DF (Table 20). The post-cracking shear ductility of the hybrid beams in terms of the DF is larger than the reference beam CB2 due to the additional bridging force provided by the SHCC. The hybrid beam with a 3D printed formwork 3DHB2 has the largest post-cracking shear ductility mainly due to the unintended deviation in SHCC formwork thickness.

	$F_{diagonal}$	$F_{85\%}$	SRF	$u_{diagonal}$	$u_{85\%}$	DF
CB2	38.9	88.1	2.26	0.44	3.76	8.54
HBT2	40.2	87.9	2.19	0.40	4.42	11.1
HBTL2	43.7	95.7	2.19	0.46	5.15	11.2
3DHB2	48.5	105.8	2.18	0.51	6.38	12.5

Table 20. SRF and DF values.

5.2.2.3. Cracking pattern

The evolution of the crack pattern is captured with DIC analysis at different load steps with GOM Correlate, based on the major principal strain field. The results of the DIC analysis are verified with the data from the LVDTs (Appendix D).

Control beam

The first flexural crack appeared at a load of 16.0 kN (Figure 77). Upon further increasing the load, more localised flexural cracks initiated and when the flexural cracks stabilised, the first diagonal crack appeared in the right shear span at a load step of 36.9 kN (Figure 77). This diagonal crack propagated towards the loading point, whilst increasing in width as the load was increasing. The diagonal crack in the left shear span also started to grow but at a lower rate (Figure 78). Afterwards, both diagonal cracks localised simultaneously up to the peak load (Figure 78). Finally, the beam failed in shear with a localised dominant shear crack in the right shear span (Figure 79).

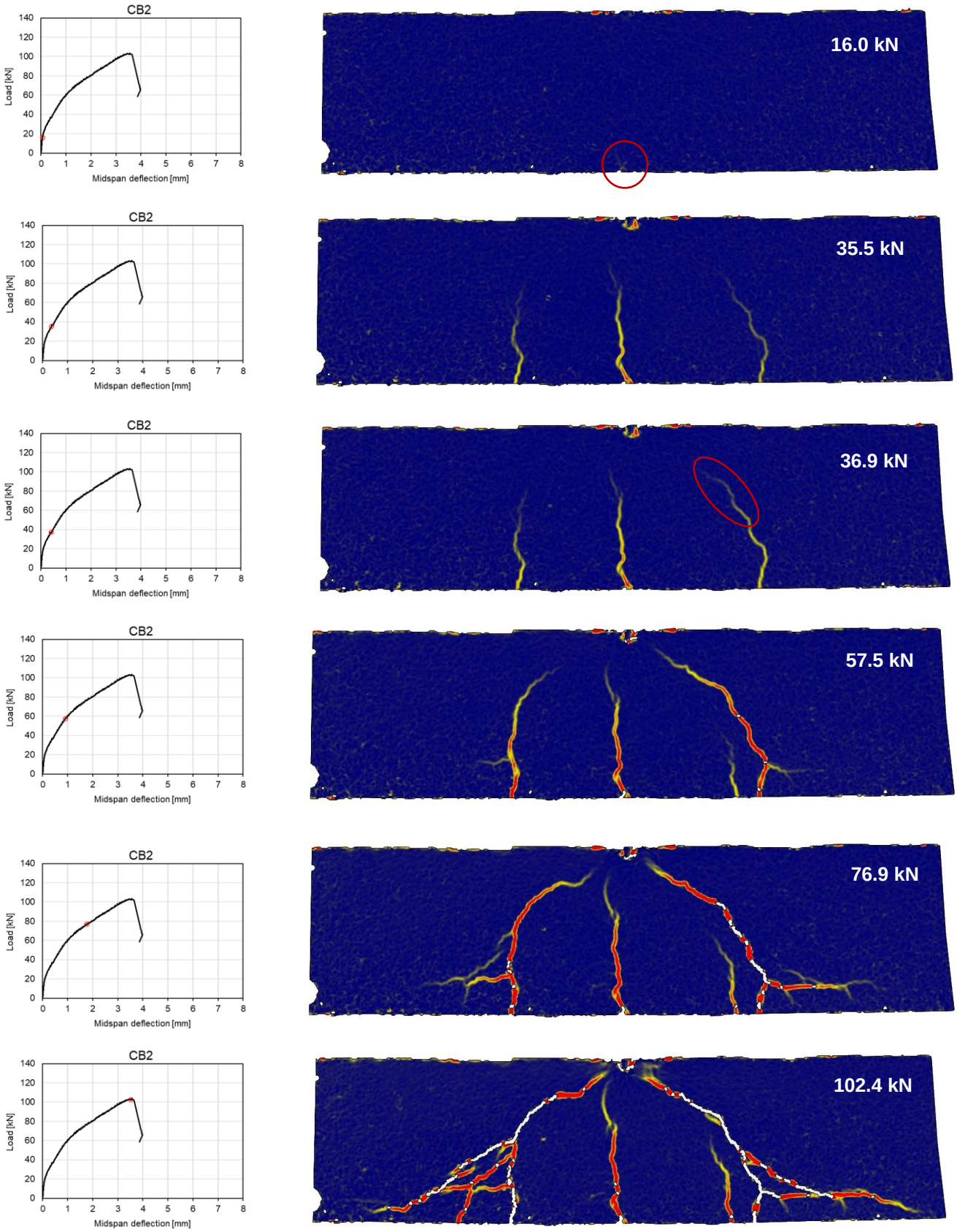

Figure 77. Development of cracks in CB2.

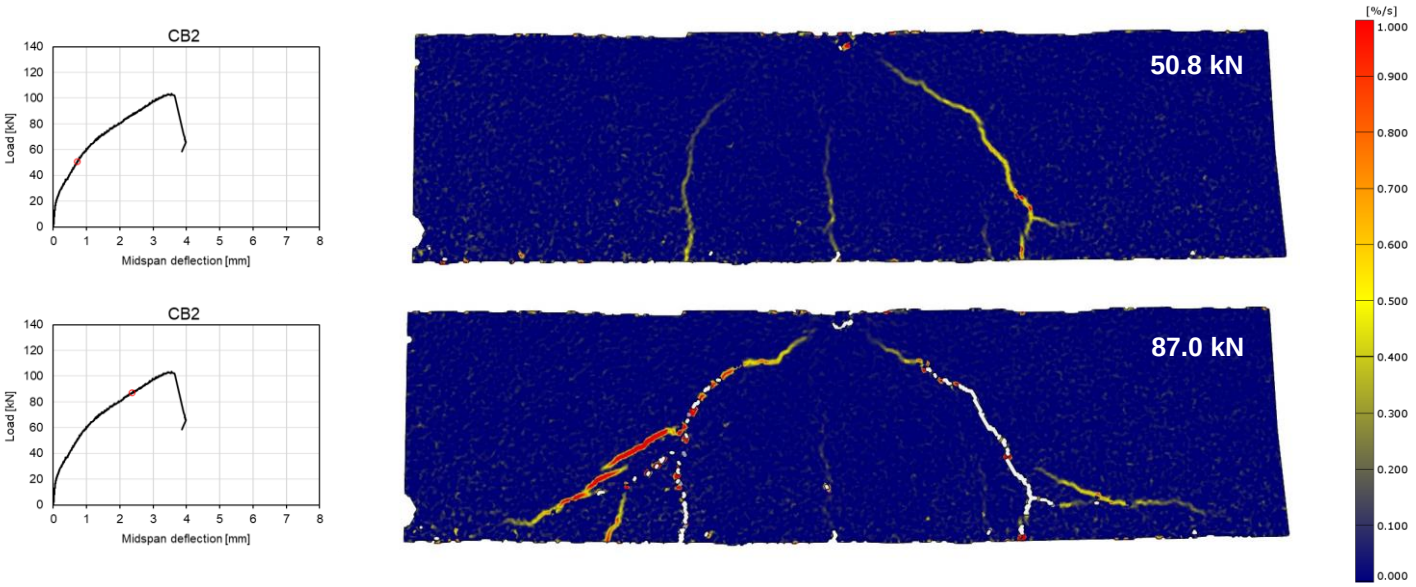

Figure 78. Growth rate major principal strain of CB2.

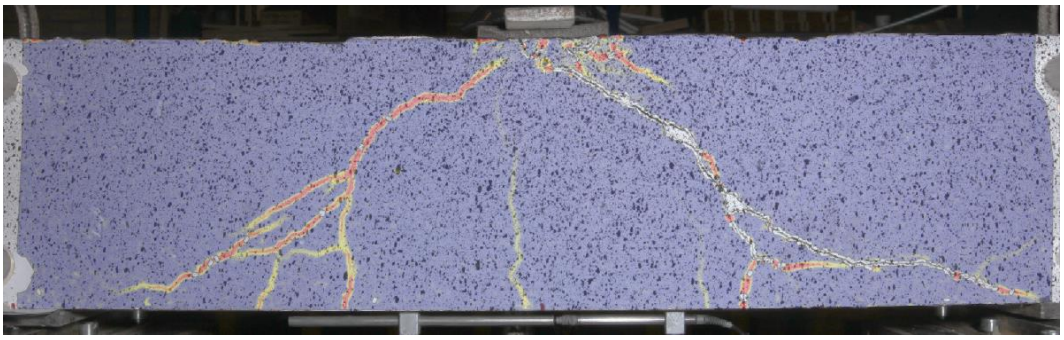

Figure 79. Dominant crack at failure of CB2.

Hybrid beam with transverse shear keys

The crack pattern of HBT2 is very different from the control beam. Instead of sparsely spaced flexural and diagonal shear cracks, multiple bundles of fine flexural and diagonal cracks appeared (Figure 80). The first diagonal crack appeared at the load step of 40.2 kN (Figure 80). Upon increasing the load, both diagonal cracks start to localise simultaneously. However, around a load of 78.5 kN, the diagonal cracks in the left shear span started to localise more compared to the diagonal cracks in the right shear span (Figure 81). Towards a load of 91.7 kN, the right diagonal crack localised at a higher rate compared to the left diagonal cracks. Afterwards, both diagonal cracks localised simultaneously up to the peak load. A large dominant diagonal shear crack appeared in the left shear span at final failure (Figure 82).

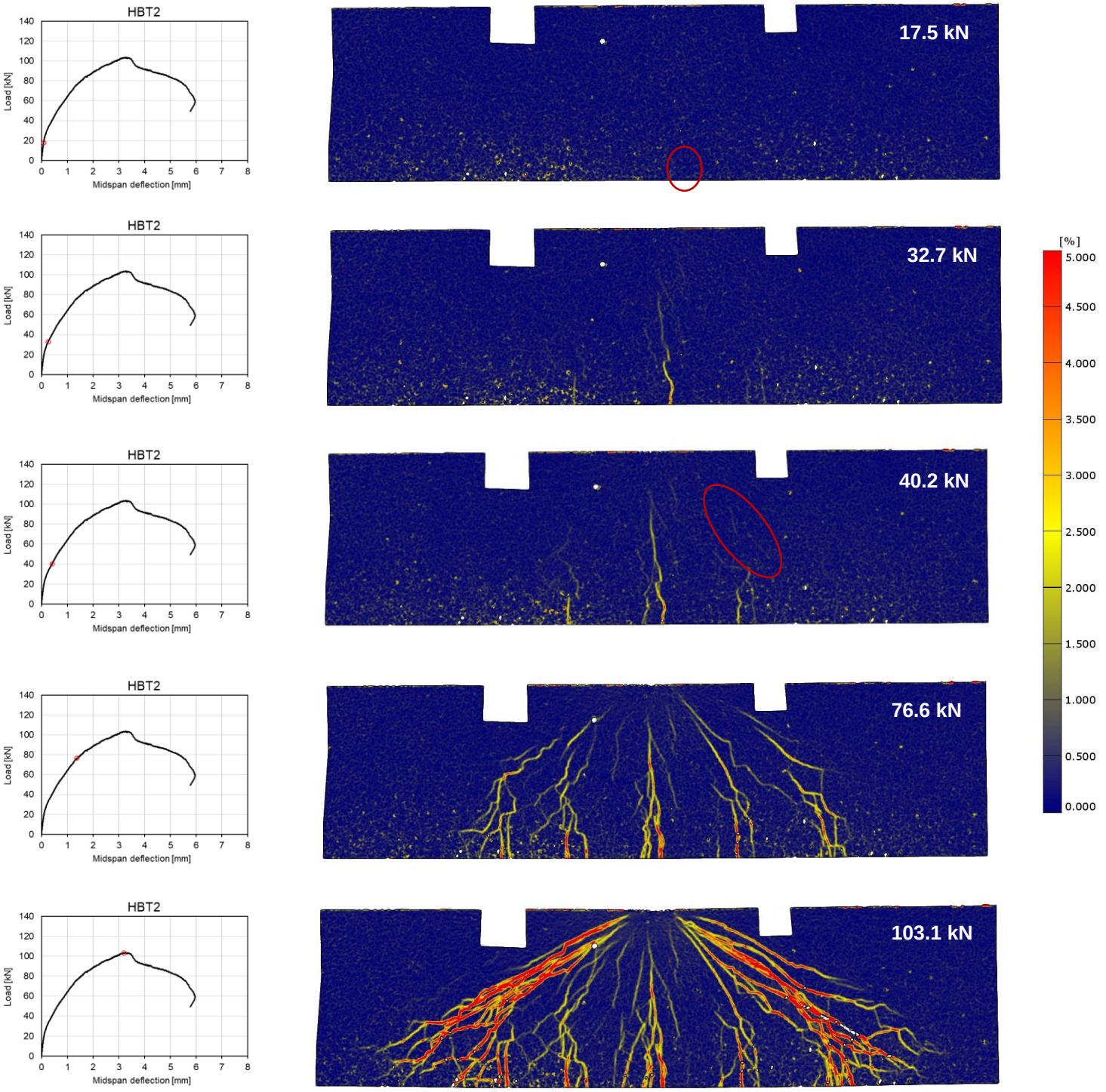

Figure 80. Development of cracks in HBT2.

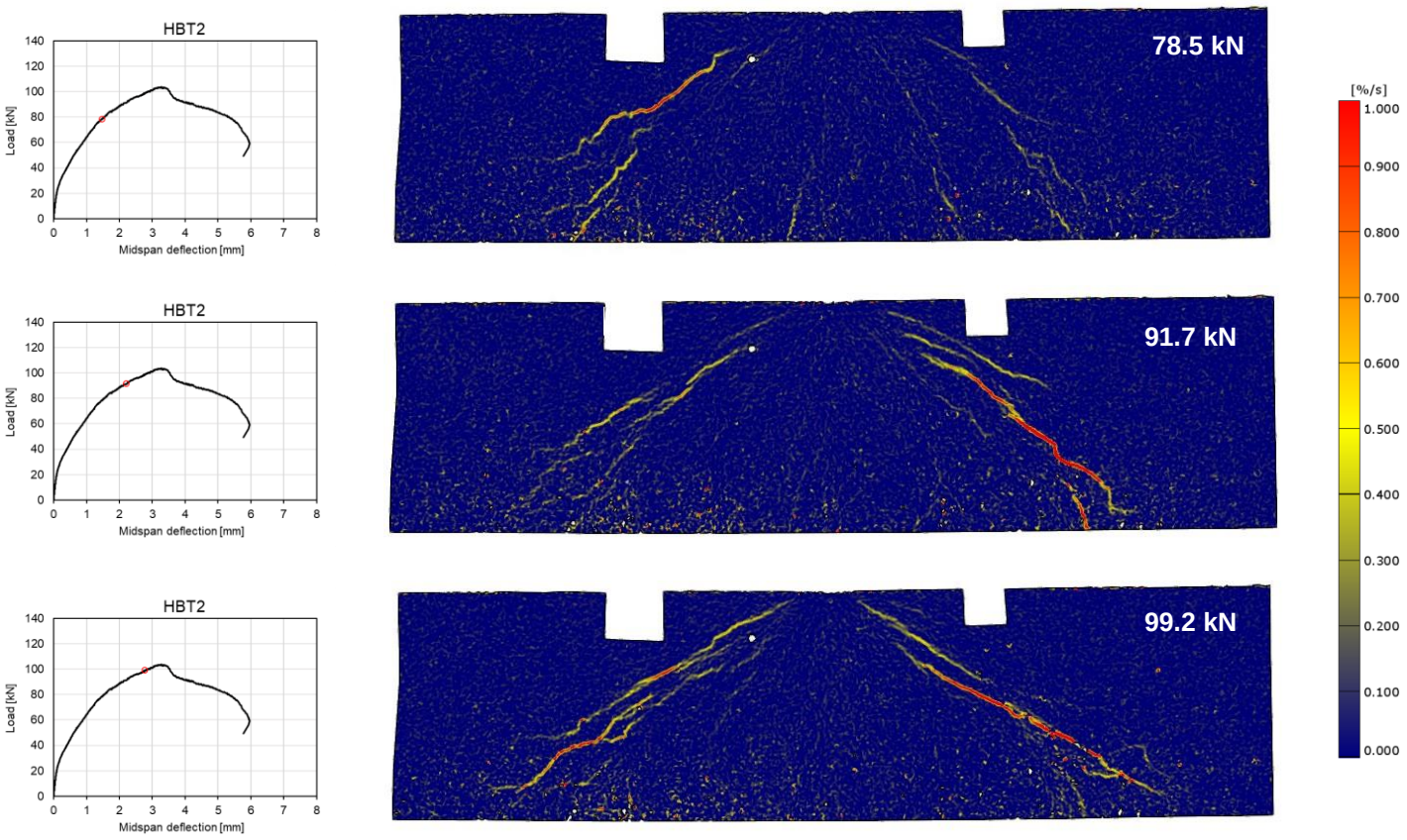

Figure 81. Growth rate major principal strain in HBT2.

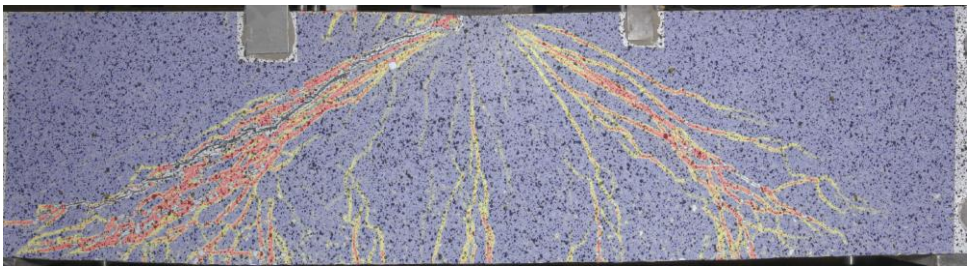

Figure 82. Dominant crack at failure of HBT2.

Hybrid beam with transverse and longitudinal shear keys

The cracking pattern of the hybrid beam with transverse and longitudinal shear keys (HBTL2) is bit different from the hybrid beam with only transverse shear keys (HBT2). Similarly as with beam HBT2, the crack pattern of HBTL2 can be characterised with multiple fine flexural and diagonal cracks. The first flexural crack appeared at a load step of 20.2 kN (Figure 83). At a load step of 43.7 kN, the first diagonal shear crack initiated in the right shear span (Figure 83). When the flexural cracks stabilised, more fine diagonal cracks start to appear. Around a load of 83.0 kN, the diagonal cracks in the right span gradually started to localise at a higher rate compared to the left diagonal cracks (Figure 85). Upon further increasing the load to the peak load, both diagonal cracks on either side localised simultaneously. The beam failed eventually with a localised diagonal crack in the right shear span (Figure 84).

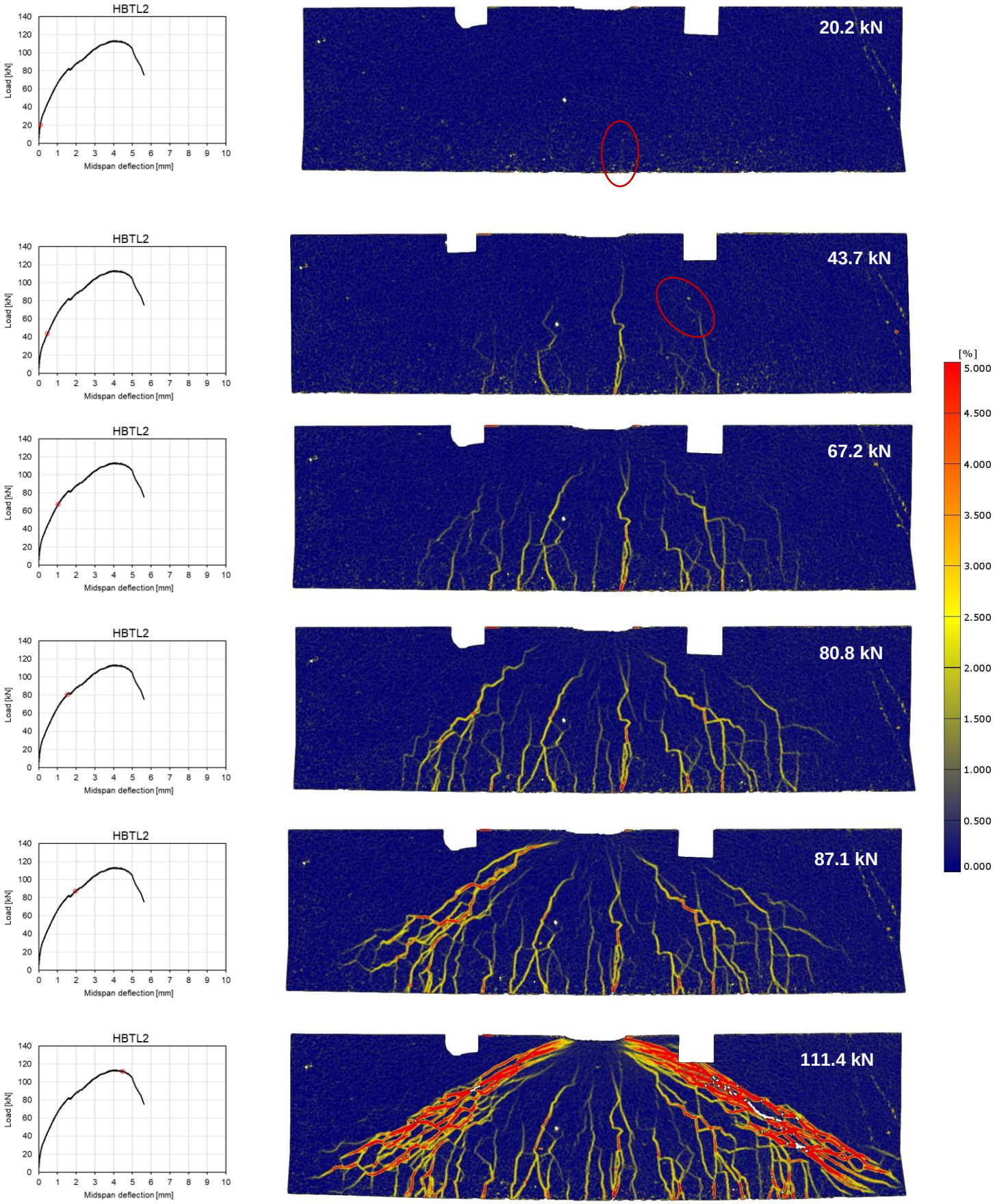

Figure 83. Development of cracks of HBTL2.

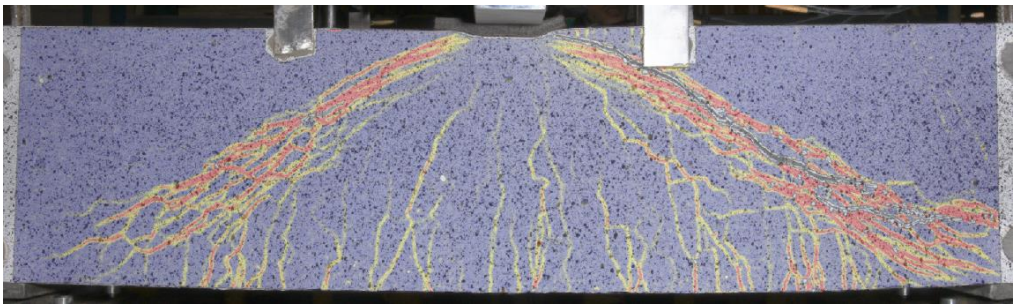

Figure 84. Dominant shear crack at failure.

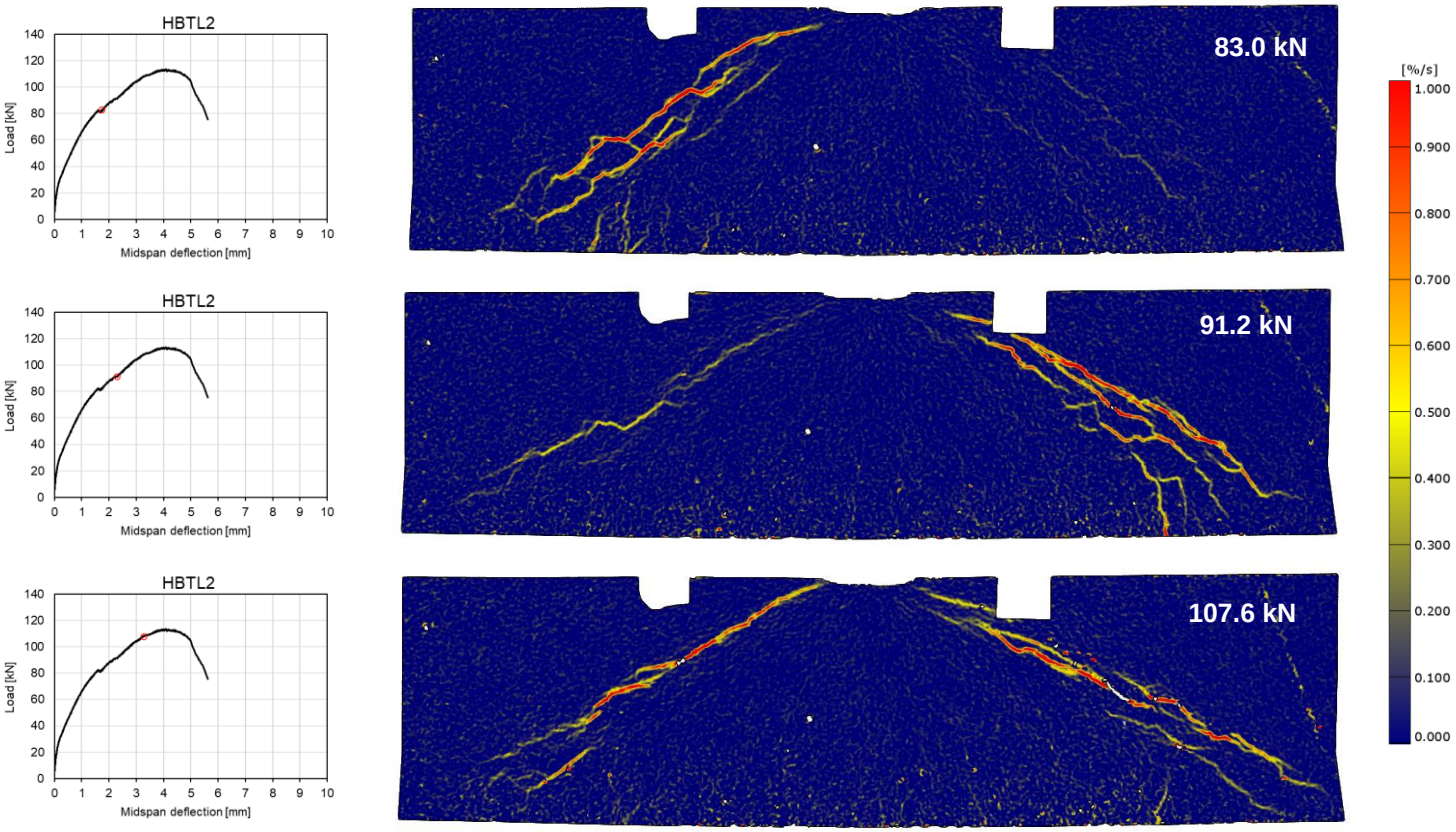

Figure 85. Growth rate major principal strain at several load steps.

The flexural cracks in HBTL2 are distributed more uniformly compared to HBT2, where the flexural cracks are more grouped up in bundles with less cracks in between. Something similar has been observed in the DIC results of HBT1 and HBTL1.

Hybrid beam with printed formwork

The first flexural crack appeared at a load step of 22.7 kN (Figure 86). After further increasing the load, the first diagonal crack appeared at a load step of 52.0 kN (Figure 86). The most noticeable aspect in the cracking behaviour of beam 3DHB2 are diagonal cracks which propagate along the interface of the printed filaments due to weak interfacial properties (Figure 86). Up to the peak load, both dominant shear cracks localised simultaneously. At post-peak, the left dominant shear crack continued to localise causing a large drop in load and failure of the beam (Figure 87).

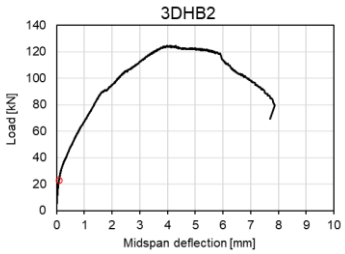
3DHB2
Load [kN]
Midspan deflection [mm]

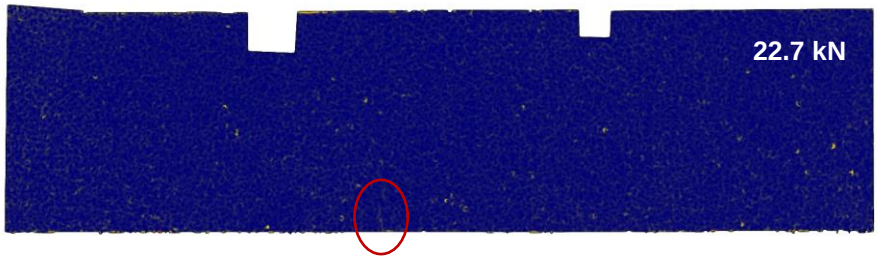
22.7 kN

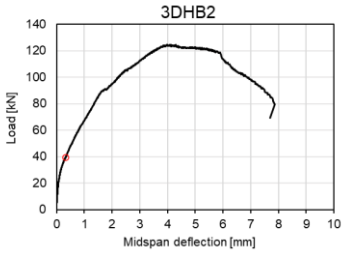
3DHB2
Load [kN]
Midspan deflection [mm]

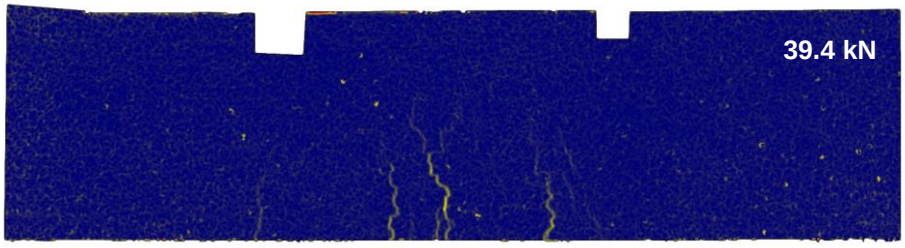
39.4 kN

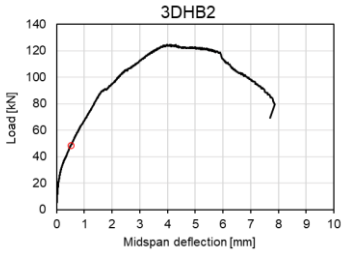
3DHB2
Load [kN]
Midspan deflection [mm]

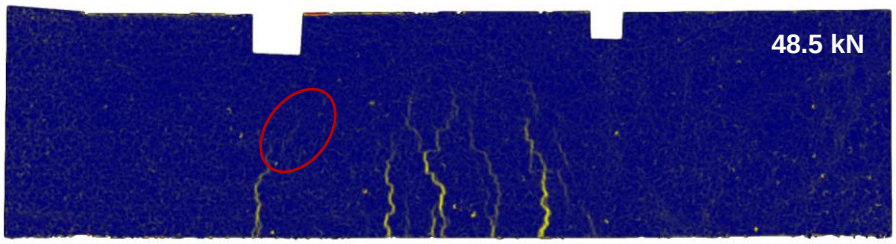
48.5 kN

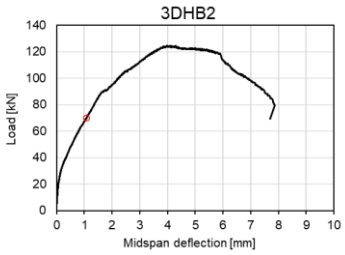
3DHB2
Load [kN]
Midspan deflection [mm]

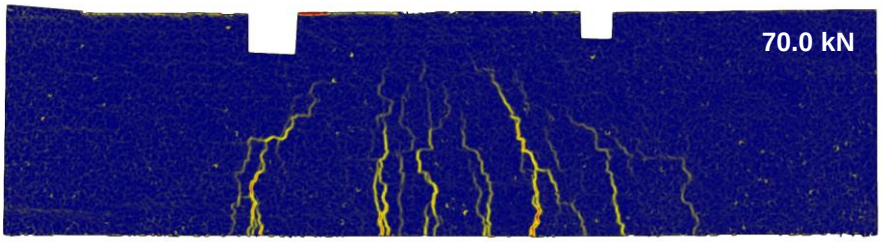
70.0 kN

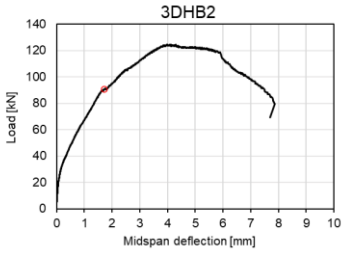
3DHB2
Load [kN]
Midspan deflection [mm]

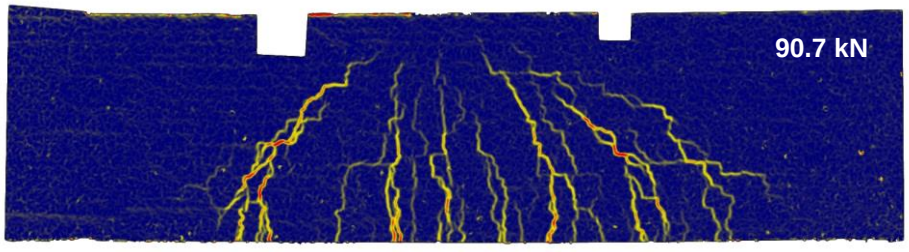
90.7 kN

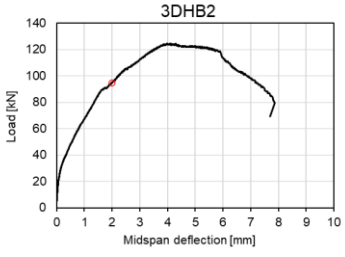
3DHB2
Load [kN]
Midspan deflection [mm]

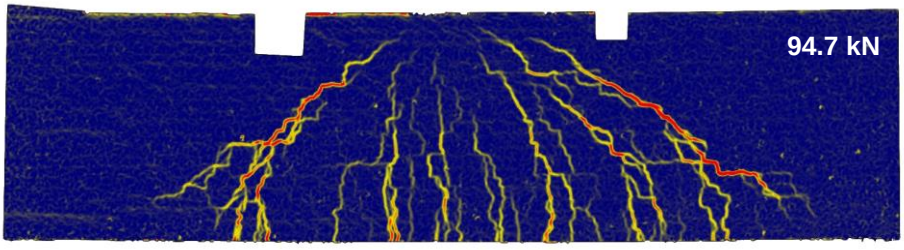
94.7 kN

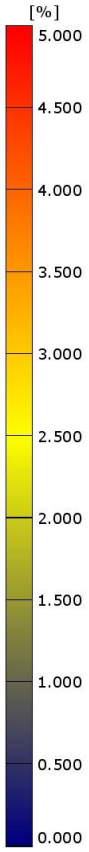
[%]
5.000
4.500
4.000
3.500
3.000
2.500
2.000
1.500
1.000
0.500
0.000

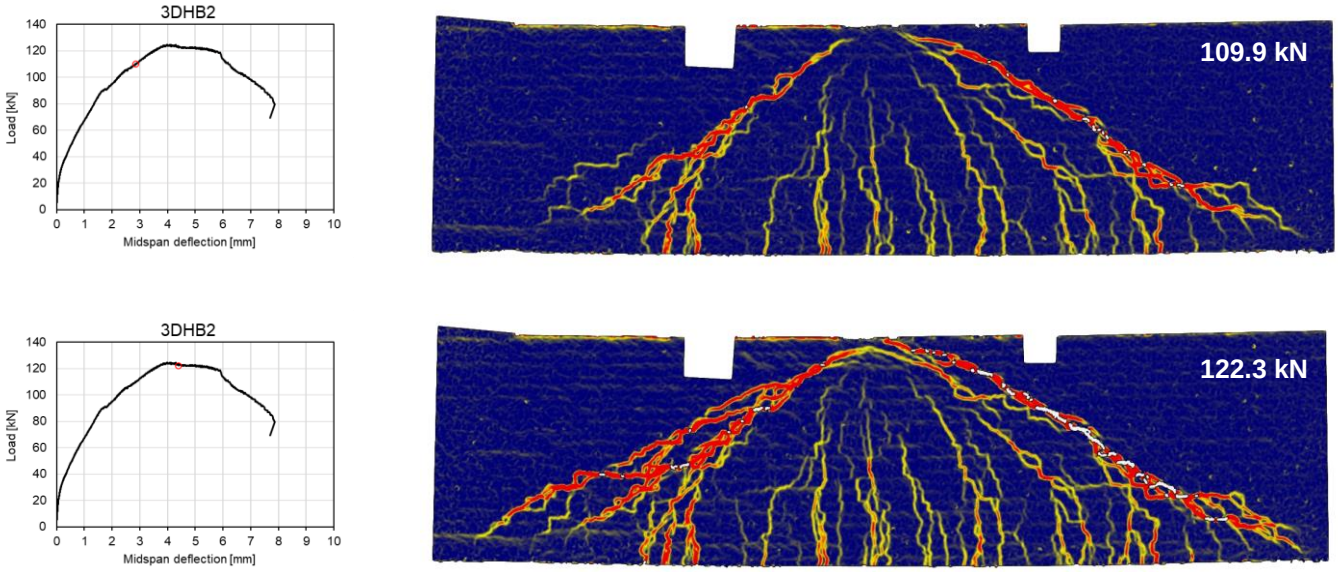

Figure 86. Development of cracks in 3DHB2.

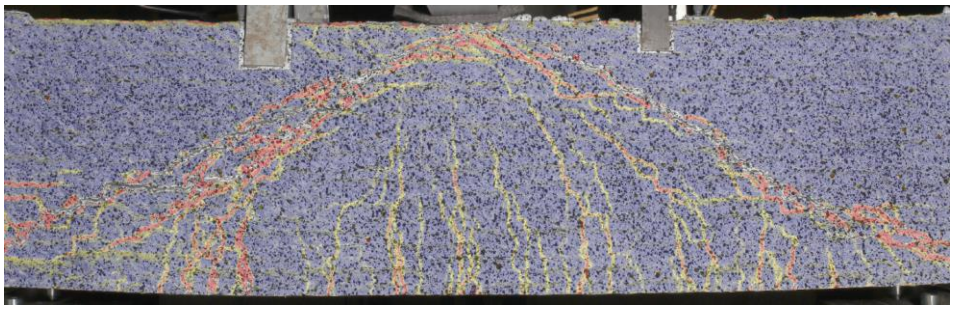

Figure 87. Dominant shear crack at failure of 3DHB2.

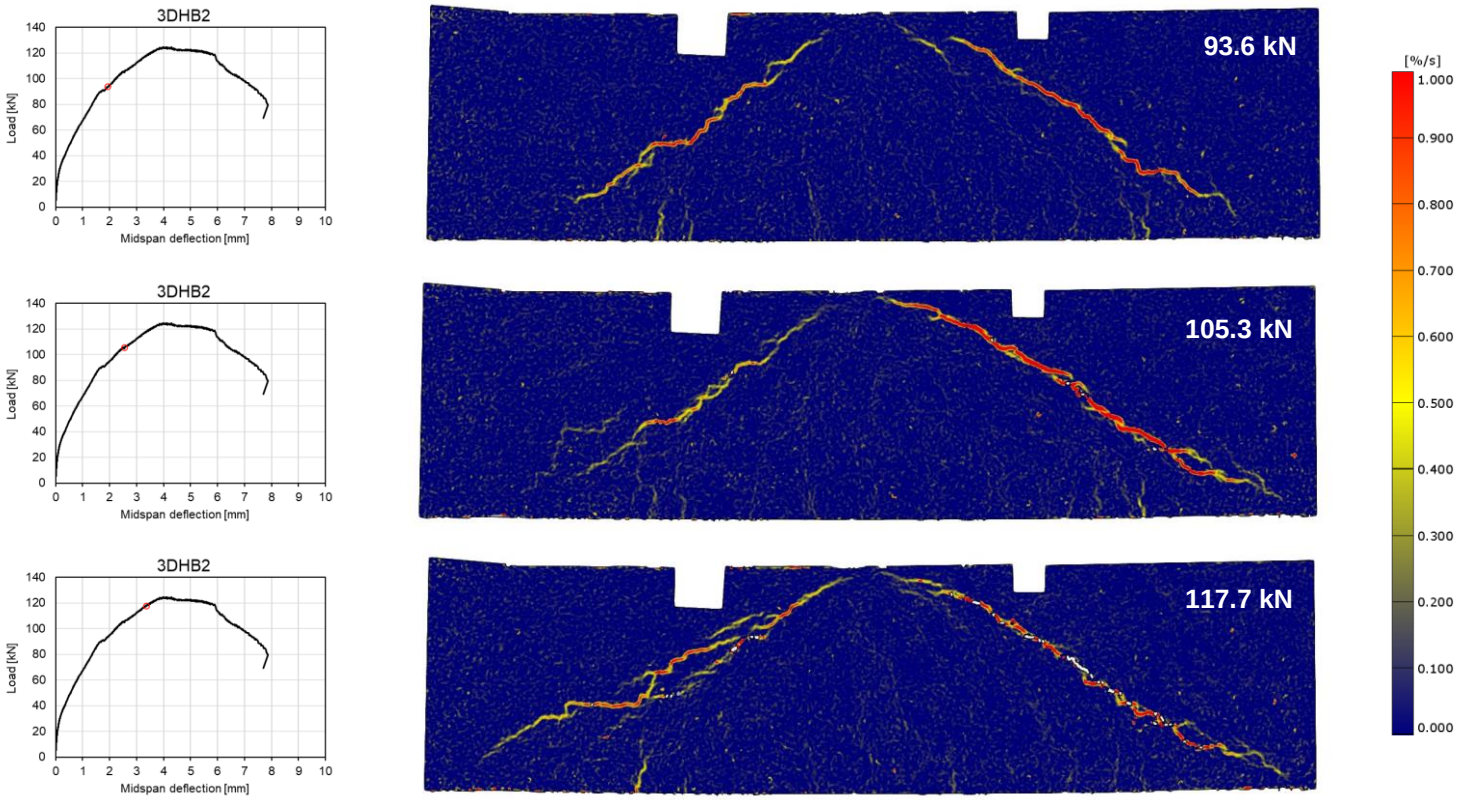

Figure 88. Growth rate major principal strain at several load steps.

5.2.2.4. Delamination

The opening between the SHCC and concrete was measured during testing with LVDTs. The position of the LVDTs is shown in Figure 51. The opening in specimen HBT2 was below 0.3 mm up to the peak load (Figure 89). The opening in beam HBTL2 had a slightly larger opening of 0.5 mm whilst 3DHB2 had almost no sight of debonding near the loading point (Figure 89 and Figure 90). The results indicate that there was no significant debonding of the SHCC formwork in all the beams.

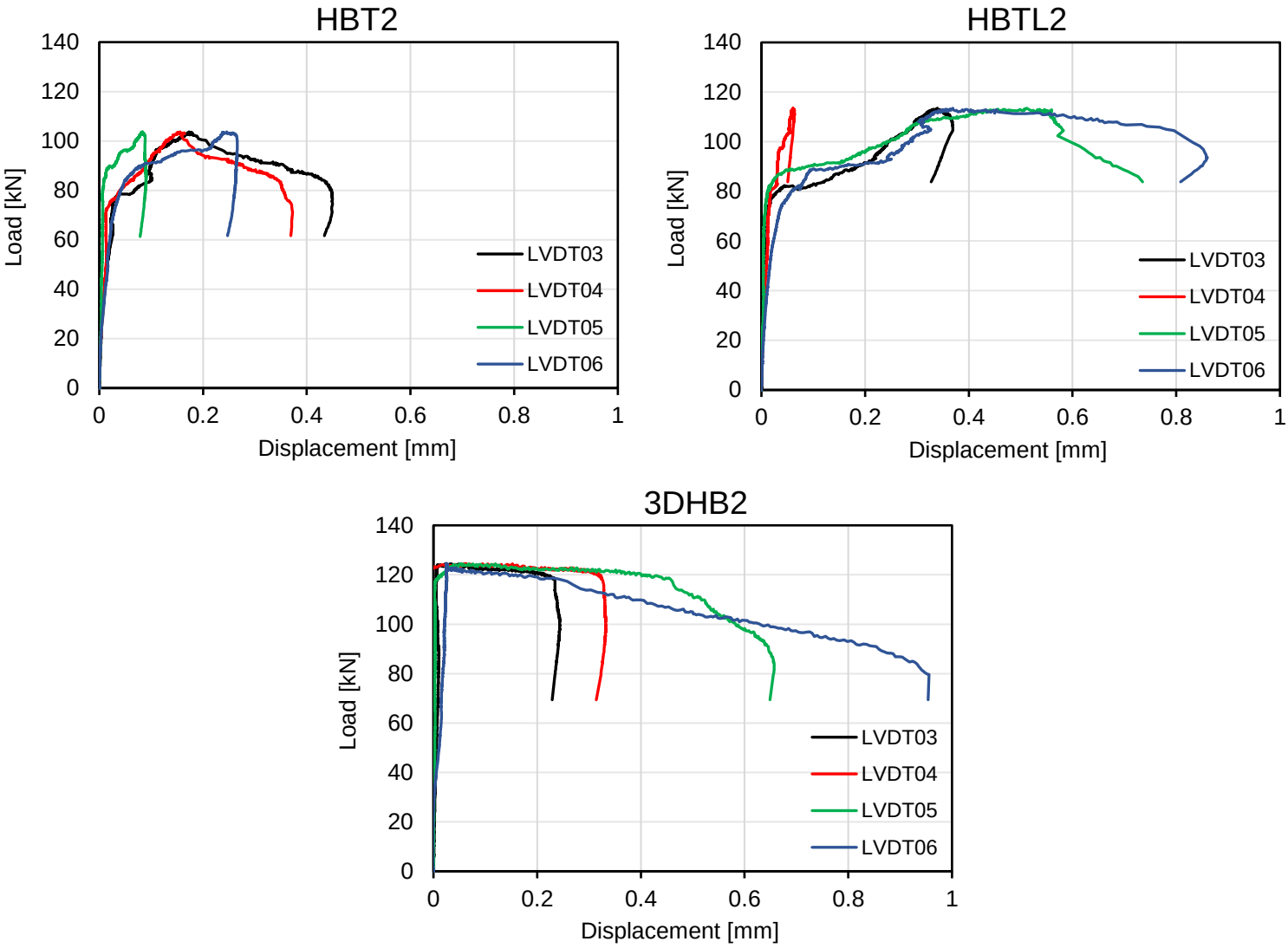

Figure 89. Opening between SHCC and concrete.

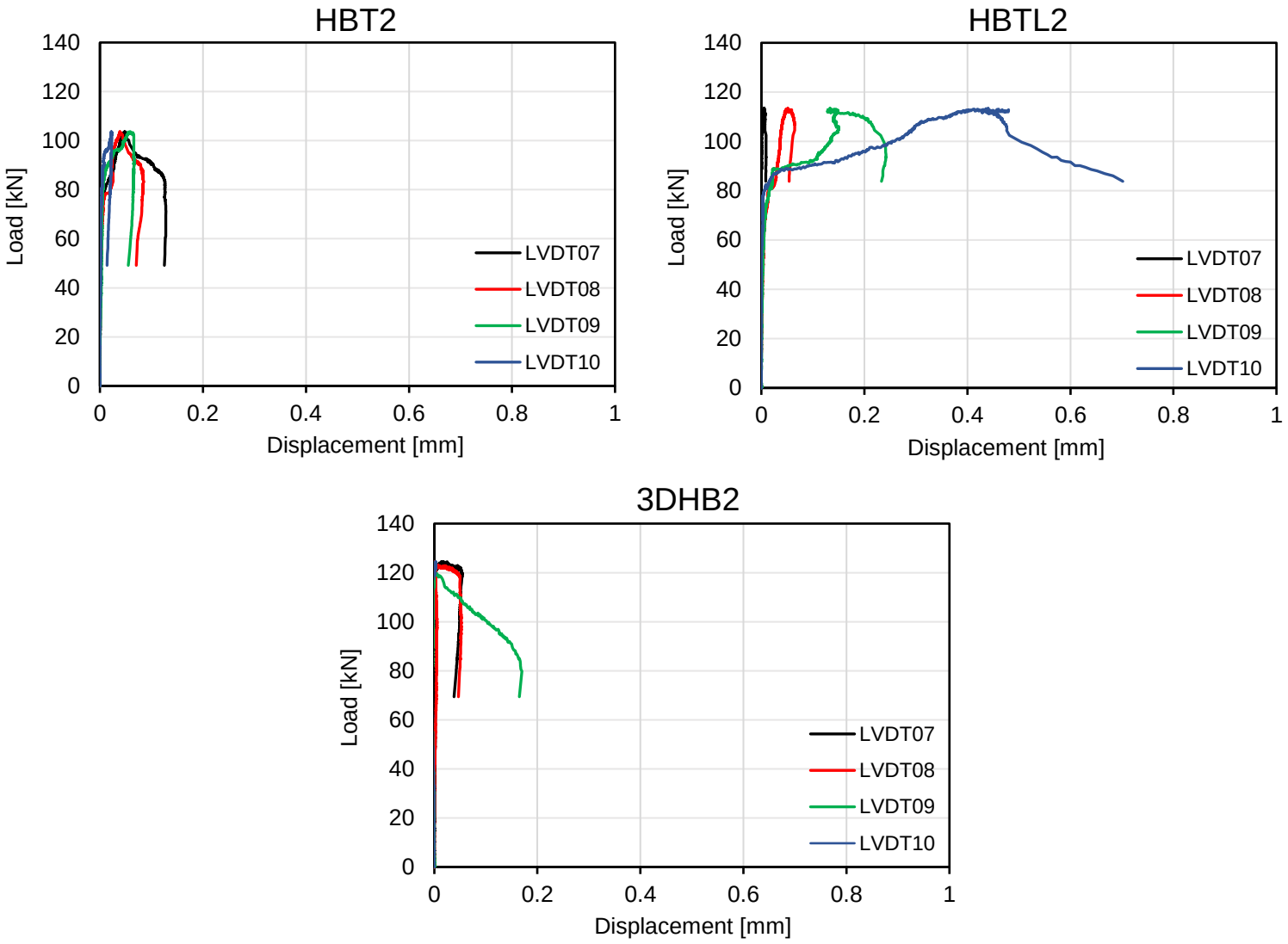

Figure 90. Sliding between SHCC and concrete.

6. Analytical model of shear carrying capacity

The direct strut-and-tie model (DSTM) for simply supported RC deeps beams proposed by Zhang and Tan [14] was used to analytically predict the shear capacity of the experimentally tested beams. Li, et al. [15] used a slightly modified version of this model to predict the failure load of shear-strengthened reinforced concrete deep beams with a PVA-SHCC jacket. The study verified the model by comparing predicted results with experimental results of strengthened beams, including experimental results from other relevant studies. The same model [15] was used to predict the shear carrying capacity of the control and hybrid beams with a precast U-shaped SHCC formwork. The force transmission mechanism of the model consists of compressive diagonal struts and a tensile tie (Figure 91).

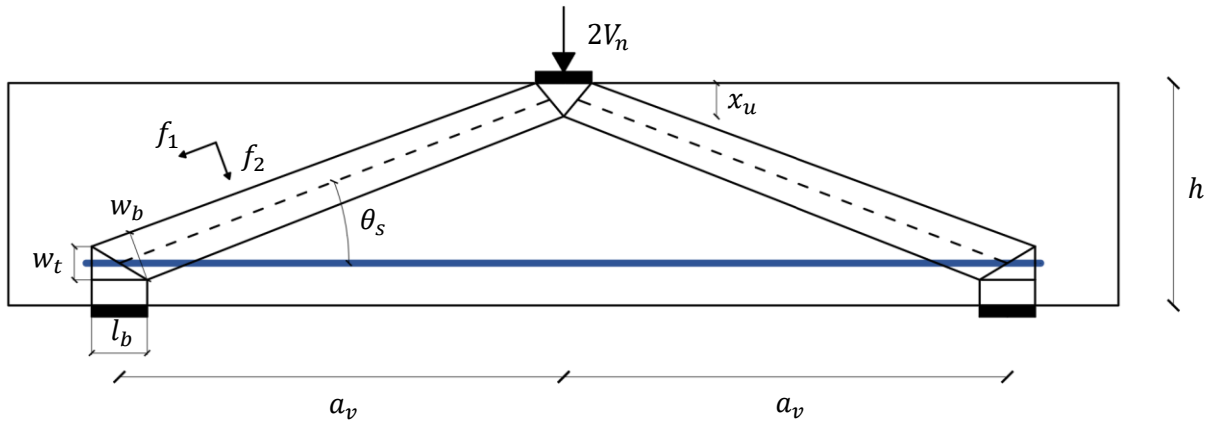

Figure 91. The DSTM model.

In the model, stress limits of the STM components and a linear failure criterion based on the Mohr-Coulomb theory for nodal zones (1) are defined in order to determine the ultimate shear capacity V_n. The principal compressive and tensile stresses f_1 and f_2 at the bottom nodal zone, the compressive capacity of the diagonal strut in the f_1 direction f_c and the tensile capacity in the f_2 direction f_t are evaluated at the bottom nodal zone.

$$\frac{f_1}{f_c} + \frac{f_2}{f_t} = 1 \tag{1}$$

For RC beams, f_c is taken as the compressive strength of concrete f_c'. The following relations hold at the bottom node due to force equilibrium:

$$F_c = \frac{V_n}{\sin(\theta_s)} \tag{2}$$

$$T_s = \frac{V_n}{\tan(\theta_s)} \tag{3}$$

F_c is the compressive force in the diagonal strut, T_s is the force in the tie and θ_s is the angle of the compressive strut. Perfect bond of the SHCC-concrete interface is assumed in the DSTM. Influence of delamination either by shrinkage or mechanical loading is not considered in the model.

6.1 DSTM for reinforced concrete beams

6.1.1 Cracked concrete tensile strength

For reinforced concrete beams without web reinforcement, the tensile capacity f_t depends on tensile strength of cracked concrete f_{ct} and dowel action f_{sl}, and can be calculated with (4).

$$f_t = f_{ct} + f_{sl} \tag{4}$$

The contribution of concrete f_{ct} is computed with (5), which is adopted from a study by Belarbi and Acun [85].

$$f_{ct} = 0.31\sqrt{f_c'}\left(\frac{\varepsilon_{cr}}{\varepsilon_2}\right)^{0.4} \tag{5}$$

The concrete cracking strain ε_{cr} and the principal tensile strain of the concrete strut ε_2 in (5) may be calculated with:

$$\varepsilon_{cr} = \frac{f_{ctm,fl}}{E_{cm}} \tag{6}$$

$$\varepsilon_2 = \varepsilon_s + (\varepsilon_s + \varepsilon_1)\cot^2\theta_s \tag{7}$$

The strain in the tension tie at failure ε_s is assumed to be equal to the steel yield strain $\varepsilon_{s,y}$, since it was observed that f_{ct} is very small compared to f_{sl}. The mean flexural tensile strength of concrete $f_{ctm,fl}$ and mean concrete elastic modulus are determined with (8) and (9) from Eurocode 2 [1].

$$f_{ctm,fl} = \max\left(0.3f_{ck}^{\frac{2}{3}}, \left(1.6 - \frac{h}{1000}\right)0.3f_{ck}^{\frac{2}{3}}\right) \tag{8}$$

$$E_{cm} = 22\left(\frac{f_{cm}}{10}\right)^{0.3} \text{ (in GPa)} \tag{9}$$

The inclined angle of the diagonal strut depends on the shear span a_v, effective depth d and height of the top nodal zone and is defined as:

$$\theta_s = \tan^{-1}\left(\frac{d-\frac{x_u}{2}}{a_v}\right)$$

In the DSTM, it is assumed that the height of the top nodal zone is equal to the height of the compression zone x_u which can be calculated by considering the horizontal force equilibrium of the tensile tie and horizontal concrete strut:

$$x_u = \frac{T_s}{\alpha f_c' b_w} \tag{10}$$

$$\alpha = \frac{\varepsilon_{c,u1} - \varepsilon_{c,3} + \frac{\varepsilon_{c,3}}{2}}{\varepsilon_{c,u1}} \tag{11}$$

α is a coefficient to transform the concrete bi-linear stress diagram to an uniform stress diagram. The tie force T_s depends on the shear capacity V_n according to (3). Thus, an iterative procedure is implemented to determine the height of the compression zone x_u. A good initial assumption is to take the height of the bottom and top nodal zone equal [14], i.e. $x_u = w_{t,max}$, where $w_{t,max}$ is calculated with (19).

6.1.2 Dowel action

Dowel action influences the shear carrying capacity of reinforced concrete. The contribution of dowel action to the shear strength is dominated by the strength of the surrounding concrete. According to research on dowel action [104], the maximum dowel force $V_{d,max}$ can be calculated with:

$$V_{d,max} = 1.27\emptyset_l^2\sqrt{f_{s,y}f_c'} \tag{12}$$

The contribution of the longitudinal reinforcement to the tensile capacity of the diagonal strut f_t is bounded by $V_{d,max}$, which depends on the rebar diameter $\emptyset_l$, reinforcing steel yield strain $f_{s,y}$ and concrete compressive strength f_c' . Using the equilibrium of forces at the bottom nodal zone, the ultimate force in the tensile tie $T_{s,max}$ when the component force of the bottom longitudinal reinforcement in the direction of the diagonal crack reaches $V_{d,max}$ can be computed with:

$$T_{s,max} = \frac{V_{d,max}}{\cos(\theta_s)} \tag{13}$$

The contribution of the longitudinal reinforcement to the tensile capacity of the diagonal strut can be related to the force in the tensile tie $T_{s,max}$ in the following manner:

$$f_{sl} = \frac{4T_{s,max}\sin(\theta_s)}{A_c/\sin(\theta_s)}$$

In (14), A_c represents the total cross-sectional area of the beam.

6.1.3 Principal stresses

Zhang and Tan [14] proposed expressions to determine the principal compressive stress f_1 (15) and principal tensile stress f_2 (16) at the bottom nodal zone.

$$f_1 = \frac{V_n}{A_{str}\sin(\theta_s)} \tag{15}$$

$$f_2 = \frac{4V_n\sin(\theta_s)\cos(\theta_s)}{A_c} \tag{16}$$

The cross-sectional area of the diagonal strut at the bottom nodal zone A_{str} can be calculated as follows:

$$A_{str} = b_w w_b \tag{17}$$

$$w_b = (l_b\cos(\theta_s) + w_t\sin(\theta_s)) \tag{18}$$

w_b is the width of the diagonal strut. The width of the tie w_t is generally taken as twice the distance from the centroid of the bottom longitudinal reinforcement to the extreme tension fibre of the beam. However, this assumption will lead to conservative results due to the relatively small beam height. Appendix A of ACI 318-08 [105] provides a practical upper limit of $w_{t,max}$ which corresponds to the width in a hydrostatic nodal zone (19).

$$w_{t,max} = \frac{A_s f_{s,y}}{f_{ce} b_w} \tag{19}$$

Many design standards provide expressions for the effective compressive strength of cracked concrete f_{ce} at CCT (compression-compression-tension) nodes. In this thesis, a different approach is used. The DSTM implicitly takes concrete softening into account due to the Mohr-Coulomb failure criterion (1). Concrete softening is expressed as a reduction of the compressive strength by a factor v which is defined as the ratio of the force in the diagonal strut F_c and strength of the strut (20).

$$f_{ce} = v f_c' \tag{20}$$

$$v = \frac{F_c}{A_{str} f_c'} \tag{21}$$

F_c depends on the shear capacity V_n (2), hence an iterative procedure is required to determine the final value of the reduction factor v.

6.2 DSTM for hybrid beams

The precast U-shaped SHCC formwork in the hybrid beams carry a part of the shear force. The contribution of the formwork to the shear capacity is incorporated in the DSTM through modifying the compressive and tensile stress limits f_c and f_t:

$$f_c = \frac{f_c' b_c h_c + \left(2t_w h_c + t_f b_w\right) f_{shcc}'}{b_w h} \tag{22}$$

$$f_t = f_{ct} + f_{sl} + f_{ht} \tag{23}$$

b_c is the inner width of the concrete, h_c is the inner height of the concrete, t_f is the thickness of the SHCC flange, t_w is the width of the SHCC webs and f_{shcc}' is the compressive strength of SHCC. The contribution of the longitudinal reinforcement and concrete to the tensile capacity of the diagonal strut, f_{ct} and f_{sl} respectively, is computed in a similar way as for a reinforced concrete beam. f_{ht} is the contribution to the tensile capacity of the diagonal strut from the SHCC webs and is computed based on an uniform rectangular distribution along the diagonal strut:

$$f_{ht} = \frac{2f_{shcc,t} t_w h / \sin(\theta)}{A_c / \sin(\theta)} = \frac{2f_{shcc,t} t_w h}{A_c} \tag{24}$$

Similarly as for the reinforced concrete beam, the height of the top nodal zone x_u for a hybrid beam can be determined with horizontal force equilibrium:

$$x_u = \frac{T_s}{\alpha f_c' b_c + 2\alpha_{shcc} f_{shcc}' t_w} \tag{25}$$

$$\alpha_{shcc} = \frac{\varepsilon_{shcc,u1} - \varepsilon_{shcc,3} + \frac{\varepsilon_{shcc,3}}{2}}{\varepsilon_{shcc,u1}} \tag{26}$$

6.2.1 Principal stresses

The principal compressive stress f_1 and principal tensile stress f_1 are computed with (15) and (16). The expressions for the maximum tie width $w_{t,max}$ and reduction factor v are modified:

$$w_{t,max} = \frac{A_s f_{s,y}}{f_{ce} b_c + 2f_{shcc,e} t_w} \tag{27}$$

$$f_{shcc,e} = v f_{shcc}' \tag{28}$$

$$f_{ce} = v f_c' \tag{29}$$

$$v = \frac{F_c}{w_b b_c f_c' + 2w_b t_w f_{shcc}'} \tag{30}$$

6.3 Prediction shear capacity

6.3.1 Material properties

A bi-linear stress-strain relationship is assumed for concrete, SHCC and reinforcing steel. The material properties are displayed in Table 21. In the DSTM the concrete compressive strength f_c' is equal to the mean cylinder compressive strength f_{cm}. The SHCC compressive strength f_{shcc}' is equal to the cube compressive strength $f_{shcc,cube}$, determined according to [106]. The dimensions of the beam and reinforcement details are taken from Figure 33 and Figure 34. The elastic modulus of SHCC was estimated using (31) which was adopted from a study by Ding, et al. [107] and relates the elastic modulus of PE-SHCC as a function of the cylinder compressive strength:

$$E_{shcc} = 686.5 f_{shcc}^{0.844} \tag{31}$$

The SHCC tensile strength $f_{shcc,t}$, ultimate strength $f_{shcc,tu}$, cracking strain $\varepsilon_{shcc,t}$ and ultimate tensile strain $\varepsilon_{shcc,tu}$ are obtained from uniaxial tensile tests (Table 11).

Concrete			SHCC			Reinforcing steel		
Class	C30/37		$f_{shcc,cube}$	60.6	MPa	$f_{s,y}$	550	MPa
f_{ck}	30	MPa	$f_{shcc,k}$	55	MPa	$f_{s,yk}$	500	MPa
f_{cm}	38	MPa	E_{shcc}	21930	MPa	E_s	200	GPa
$f_{ctm,fl}$	4.06	MPa	ε_{shcc3}	2.76	‰	$\varepsilon_{s,y}$	0.275	%
E_{cm}	32836	MPa	ε_{shcc1}	3.50	‰	$\varepsilon_{s,u}$	5	%
$\varepsilon_{c,3}$	1.16	‰	$f_{shcc,t}$	1.80	MPa			
$\varepsilon_{cu,1}$	3.50	‰	$f_{shcc,tu}$	2.64	MPa			
ε_{cr}	0.12	‰	$\varepsilon_{shcc,t}$	0.03	%			
			$\varepsilon_{shcc,tu}$	2.45	%			

Table 21. Material properties used in the DSTM.

6.3.2 Control beam

The input for the DSTM is depicted in Table 22. The height of the top nodal zone x_u is initially assumed to be equal to the height of the bottom nodal zone $w_{t,max}$, determined with (19). The shear capacity of

CB2					
α	0.83		d_l	12	mm
v	0.5		A_{sl}	226.2	mm^2
h	200	mm	a_v	400	mm
d	156	mm	A_c	30000	mm^2
b_w	150	mm			

Table 22. Input DSTM.

the control beam was calculated with the DSTM model and corresponding assumptions (Table 23). The calculated failure load F_{cal} was overestimated by 3% compared to the experimental value F_{exp}.

CB2						
Dimensions				**Principal stress**		
x_u	31.7	mm		v	0.44	
$w_{t,max}$	49.9	mm		w_b	64.0	mm
θ	19.3	°		A_{str}	9506	mm^2
Stress limit				f_1	16.7	MPa
ε_1	0.05	-		f_2	2.19	MPa
f_{ct}	0.17	MPa		**Shear capacity**		
$V_{d,max}$	26.4	kN		V_n	52.6	kN
$T_{d,max}$	28.1	kN		F_{cal}	105.1	kN
f_{sl}	3.74	MPa		F_{exp}	103.7	kN
f_t	3.91	MPa		F_{cal}/F_{exp}	1.03	
f_c	38	MPa				

Table 23. Calculated shear capacity of control beam with DSTM.

6.3.3 Hybrid beam with transverse shear keys

The shear capacity of HBT2 was determined according to the DSTM with the input given in Table 24. The shear capacity was overestimated by 6.7% compared to the experimental failure load F_{exp} of specimen HBT2.

HBT2					
α_{shcc}	0.61		t_f	15	mm
v	0.5		t_w	15	mm
h	200	mm	d_l	12	mm
h_c	185	mm	A_{sl}	226.2	mm^2
d	156	mm	a_v	400	mm
b_w	150	mm	A_c	30000	mm^2
b_c	120	mm			

Table 24. Input DSTM.

HBT2					
Dimensions			**Principal stress**		
x_u	32.2	mm	v	0.49	
$w_{t,max}$	41.0	mm	w_b	55.2	mm
θ	19.3	°	A_{str}	8278	mm²
ε_1	0.05	-	f_1	20.2	MPa
Stress limit			f_2	2.30	MPa
f_{ct}	0.17	MPa	**Shear capacity**		
$V_{d,max}$	26.4	kN	V_n	55.3	kN
$T_{d,max}$	28.0	kN	F_{cal}	110.6	kN
f_{sl}	3.73	MPa	F_{exp}	103.7	kN
f_{ht}	0.36	MPa	F_{cal}/F_{exp}	1.067	
f_t	4.27	MPa			
f_c	43.9	MPa			

Table 25. Calculated shear capacity of HBT2.

6.3.4 Hybrid beam with transverse and longitudinal shear keys

The influence of interface conditions is not considered in the DSTM. Therefore, the calculated shear capacity of HBT2 and HBTL2 are similar. It should be noted that the tensile stress-strain curve of SHCC in HBTL2 was different from the SHCC in HBT2 (Figure 59). The tensile properties of mixture PE1SF10-TL (Table 11) are implemented in the calculation of the shear capacity of HBTL2. The experimental shear capacity was underestimated by roughly 2.2% with the DSTM (Table 26).

HBTL2					
Dimensions			**Principal stress**		
x_u	32.4	mm	v	0.48	
$w_{t,max}$	40.4	mm	w_b	54.6	mm
θ	19.3	°	A_{str}	8195	mm²
ε_1	0.05	-	f_1	20.5	MPa
Stress limit			f_2	2.31	MPa
f_{ct}	0.17	MPa	**Shear capacity**		
$V_{d,max}$	26.4	kN	V_n	55.5	kN
$T_{d,max}$	28.0	kN	F_{cal}	111.0	kN
f_{sl}	3.73	MPa	F_{exp}	113.5	kN
f_{ht}	0.43	MPa	F_{cal}/F_{exp}	0.978	
f_t	4.33	MPa			
f_c	43.9	MPa			

Table 26. Calculated shear capacity of HBTL2.

7. Discussion

The SHCC in the hybrid beams influenced the structural behaviour in many ways. Some of the main findings and unexpected results will be discussed in this chapter.

7.1 Flexure

7.1.1 Load bearing capacity

The hybrid beams had 47.6-61.2% higher load bearing capacity compared to the reference beam. This result deviates a lot with results found in literature. The largest increase in peak load in the study of Qiao, et al. [88] on SHCC-RC hybrid beams with a U-shaped permanent formwork was 18.2%. The loading span was 1200 mm. Another similar small-scale experiment with a loading span of 300 mm found an increase in load bearing capacity of 63-93% depending on the surface roughness [87]. The large scatter in the relative increase of the load bearing capacity is a result of the difference in loading span. The loading span influences the increase of the load bearing capacity, because a 1% increase in load results in a higher absolute increase in bending moment for longer spans.

The unexpected load-displacement curve of the reference beam CB1 (Figure 62) indicates that maybe the results from CB1 are not accurate. A multi-layer model (MLM) proposed by A. Yassiri [9] was implemented for comparing and evaluating the accuracy of the load displacement curve of the control beam (Figure 62). The peak load could be predicted fairly accurately, but not the mid span deflection at peak load (Table 13). To better understand the unexpected results of the reference beam, the results are compared with similar studies conducted by Singh [33] and Huang [13] on slender beams. The reference beams in those studies have the same concrete mix, one extra steel bar, a longer span and slightly different effective depth. The load capacity of the beams is given in terms of bending moment to make the results comparable. The bending moment at yielding M_y and bending moment at failure M_u of the reference studies are normalized through reducing it by 33% since in this research only two longitudinal bars are used. Since CB1 can be regarded as a deep beam, part of the load is also transferred directly to the support, so the assumption is that the bending moment at failure of CB1 should be similar or even higher than the reference studies. However, the general trend is that yielding of the reinforcement and failure of the reference beam (CB1) happens at a lower bending moment compared to the reference beams of the reference studies, except the reference beam of Huang with a cover of 31 mm (Figure 92). CB1 has a concrete cover of 38 mm, i.e. a lower effective depth compared to the other beams, which may explain why there is a difference in bending capacity. However, the MLM is not accurate in predicting the load-displacement response of the hybrid beam (Figure 93). The predicted load at yielding of the reinforcement and failure load were 98.3 kN and 119.8 kN, respectively, whereas the experimental values for the hybrid beam with transverse profiled interface were 119.9 kN and 145.1 kN. This indicates that the MLM is very conservative in predicting the failure load of the deep beams. Thus, the load at yielding of the reinforcement F_y and F_{max} are overestimated by 22.0% and 21.1%, respectively.

The load-displacement response of CB1 definitely does not seem to be realistic. Nonetheless, the designed peak load of CB1 and peak load obtained from the MLM are both close to the peak load of CB1. In addition, the peak load of CB1 does not deviate a lot from the trend seen in the reference beams of Singh and Huang. Based on this finding, it is believed that the peak load of CB1 is accurate enough for a comparison with the hybrid beams.

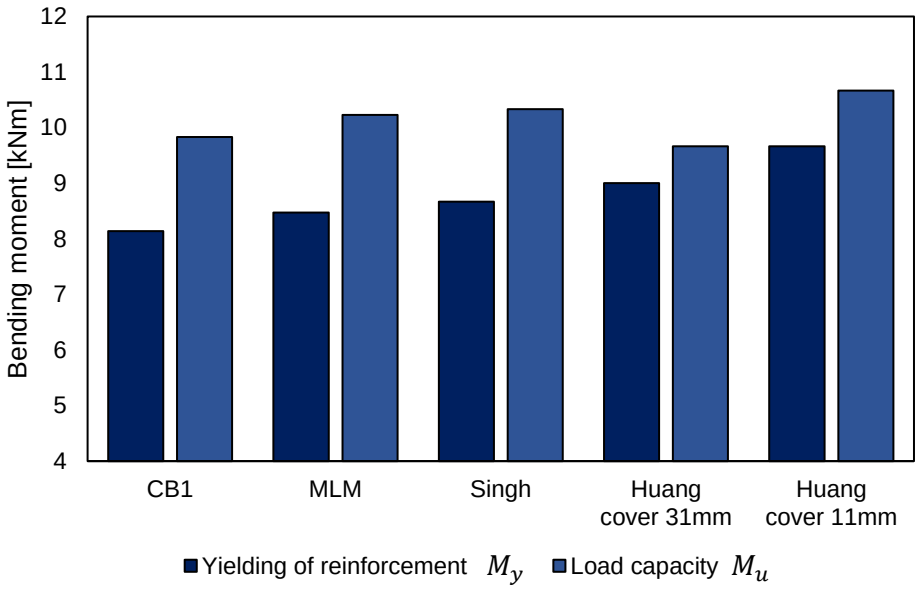

Figure 92. Normalized bending moment at yielding of reinforcement and failure.

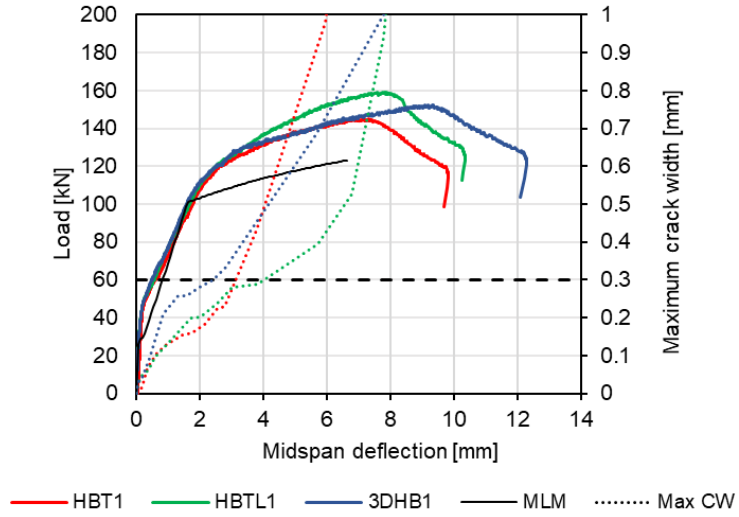

Figure 93. Load-deflection and maximum crack width response of the hybrid beams.

7.1.2 Cracking pattern and crack width

The SHCC-RC hybrid beams show superior crack width control compared to the reference beam. The cracking pattern of the reference beam consisted of a few large localised flexural cracks. In comparison, the hybrid beams with a U-shaped SHCC lost formwork exhibited multiple fine flexural cracks, uniformly distributed along the constant moment region. The hybrid beams with a precast SHCC U-shaped formwork had a similar number of cracks in the section located 7.5 mm above the bottom. The number of cracks along the section decreased with increasing height. Interestingly, this was not the case for the hybrid beam with a printed SHCC formwork. 3DHB1 had 60 cracks at section 2 located 25 mm above the bottom and section 1 located 7.5 mm above the bottom had only 46 cracks (Figure 70). This difference can be the result of the interfacial properties between the 3D printed SHCC and concrete at section 2. Since section 1 is not in direct contact with the concrete, the cracking pattern in the SHCC at section 1 is not as much affected by the concrete compared to section 2. The interface condition at section 2 is sufficient to prevent complete delamination, but at the same time also insufficient to allow large cracks in the concrete to localise early and propagate in the SHCC. This effect of the SHCC-

concrete interface condition on the cracking pattern of SHCC-RC hybrid beams and even retrofitted/repaired beams is also found in other studies [30, 33]. Partly debonding compared to no debonding of the SHCC is more beneficial for increasing the cracking zone in the SHCC.

The maximum crack width could be reduced significantly by utilising SHCC with concrete. The maximum crack width threshold of 0.3 mm localised at a load of 48.3 kN in the reference beam, whilst the threshold in the hybrid beams HBT1, HBTL1 and 3DHB1 was reached at 124.7 kN, 137.3 kN and 119.0 kN, respectively (Table 18). In section 5.2.1.1 it was explained that the load-deflection response, and hence the maximum crack width of the reference beam CB1, is likely inaccurate. To qualitatively access the accuracy of the crack width data of reference beam CB1, the load at which the crack width of 0.3 mm localised $F_{0.3}$ in the reference beam is compared with the MLM and the studies of Singh [33] and Huang [13] (Figure 94). The control beams of the reference studies have one extra reinforcement bar and a longer span, so in order to make the results more comparable, the load is given in terms of the bending moment. The bending moment corresponding to $F_{0.3}$, $M_{0.3}$, and the bending moment corresponding to the yielding of the reinforcement M_y of the reference studies are reduced by 33% to account for the additional reinforcing bar. Here it is assumed that the maximum crack width correlates linearly with the stress in the steel, i.e. the area of the reinforcement.

In all the reference beams the crack width of 0.3 mm localised before yielding of the reinforcement, except the concrete beam of Huang with a cover of 11 mm (Figure 94). The concrete cover (or effective depth) seems to have a big impact on the load at which the crack width of 0.3 mm first localises. The crack width of 0.3 mm localised in CB1 at the lowest bending moment. The concrete cover of CB1 is 38 mm and that partly explains why $M_{0.3}$ is lower compared to the reference beams of the Singh and Huang. Moreover, the MLM was implemented to predict $M_{0.3}$ of CB1. The MLM overestimated the bending moment in CB1 by 60%. In addition, the MLM model predicted that for the beam of Huang with a cover of 31 mm, crack width localisation would occur after yielding of the reinforcement, whilst in fact the crack width of 0.3 mm localised before yielding of the reinforcement [9]. In general, the maximum crack width obtained from the MLM deviates a lot from the experiment (Figure 95). However, when the comparing $M_{0.3}$ of CB1 with the beams of Singh and Huang, a trend is visible and hence, it can be argued that the obtained value of $M_{0.3}$ of CB1 is maybe not far off from the real value. It is possible that during testing of CB1, the movement and out-of-plane motion of the setup mostly occurred at a higher load. Thus, it would be justifiable to use the value of $F_{0.3}$ for the reference beam CB1 in Table 18 for the sake of comparison with the hybrid beams HBT1, HBTL1 and 3DHB1.

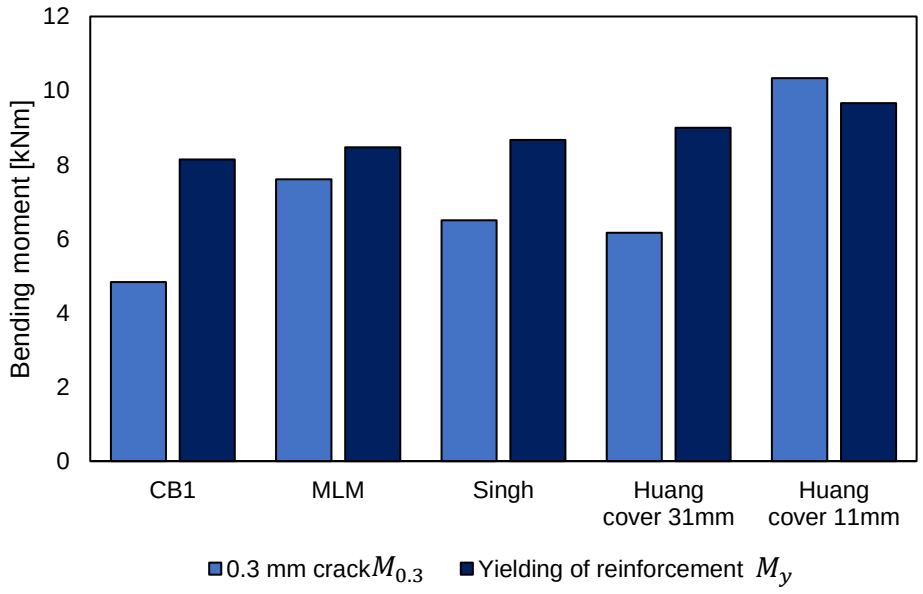

Figure 94. Normalized bending moment at yielding of reinforcement and when the crack width reaches 0.3 mm.

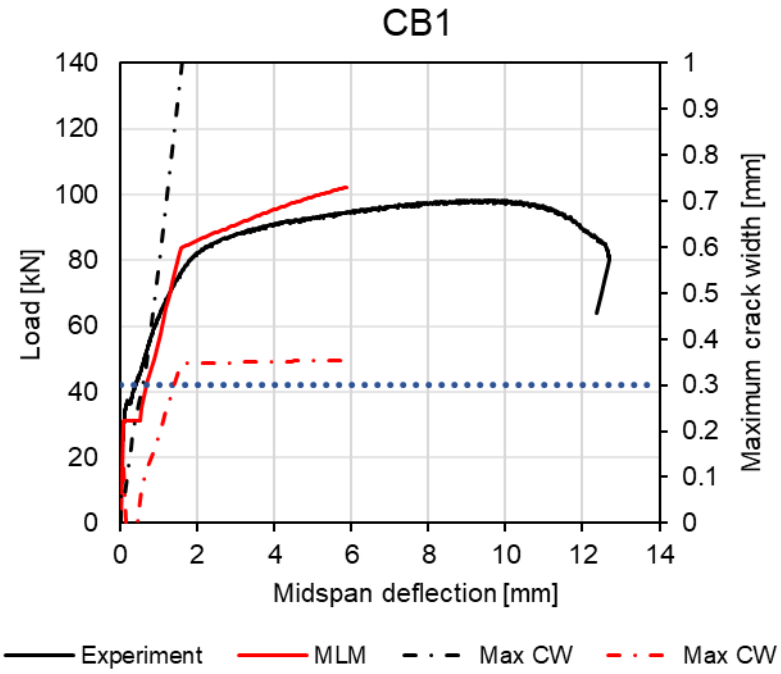

Figure 95. CB1 versus MLM.

The cracking behaviour in bending of the hybrid beam with a 3D printed formwork differs from the cracking pattern of the hybrid beams with a precast SHCC formwork. The number of cracks at section 2 located 25 mm above the bottom was higher compared to the number of cracks at section 1 located 7.5 mm above the bottom for the former beam. This was not the case for the beam with a precast SHCC formwork. It is believed that the higher number of cracks is related to the difference in interfacial properties. The surface texture of the 3D printed formwork allowed the development of sufficient debonding length. As a result, the strain generated could be distributed over a longer zone allowing the cracks to be distributed in the SHCC, without early localisation. Singh [33] found a similar effect. Singh investigated the influence of interface conditions on crack control in SHCC-concrete hybrid beams with SHCC in the tension zone. A smooth interface roughened with wire brush resulted in more cracks in the SHCC layer compared to a smooth interface, without excessive debonding. The cracking pattern of the hybrid beam with toothed grooves exhibited monolithic behaviour as some cracks in the SHCC directly propagated in the concrete. The toothed grooves functions similarly as the circular shear keys in this research. The profiled interface with circular shear keys enabled a small debonding length due to mechanical interlock at the interface. As a consequence, the generated cracks in the SHCC is concentrated over a smaller zone at the interface resulting in less cracks in the precast SHCC formwork compared to the hybrid beam with 3D printed formwork.

7.2 Shear

7.2.1 Load bearing capacity

The hybrid beams had an equal or higher shear resistance compared to the reference beam CB2. The failure load of the reference beam CB2 was 103.7 kN, whilst HBT2, HBTL2 and 3DHB2 failed at 103.7 kN, 113.5 kN and 124.5 kN, respectively. In general, this result can be attributed to the crack bridging force provided by the PE fibres and the higher compressive strength of SHCC. Surprisingly, the shear capacity of HBT2 was not higher compared to reference beam. Two factors could have caused this. Firstly, the difference in elastic modulus of concrete and SHCC. Generally, SHCC has a lower elastic modulus compared to concrete due to the absence of coarse aggregates. Secondly, the SHCC-RC profiled interface at the web prevented significant debonding and slip, hence the strain in the concrete and SHCC at the interface were similar. This leads to concrete attracting more load as opposed to the

SHCC webs. As a result, the SHCC was not activated to a full extent. A similar observation was described in the research of Budnik [97]. In that research the shear capacity of a hybrid SHCC-concrete beams with SHCC lamellas applied laterally and different interface conditions was investigated. From the fluctuating growth rate of the cracks in the hybrid beam with a smooth and profiled interface, it was concluded that a lot of redistribution of internal forces occurred due to the difference in the elastic modulus of concrete and SHCC. Thus, the SHCC could not be fully activated. However, Budnik [97] reported that the hybrid beams with a smooth and profiled interface had a 12.1 kN and 13.2 kN higher shear capacity compared to the reference beam, respectively. It is possible that the SHCC with polyethylene fibres in this study was activated to a lesser extent compared to the PVA-based SHCC in [97], because the PE-SHCC had a lower elastic modulus compared to the PVA-based SHCC.

The very high shear capacity of 3DHB2 is a result of the unintended deviation in SHCC formwork thickness. However, a larger SHCC formwork thickness does not necessarily result in a larger shear resistance. The reference beam of a similar study conducted by Zhang, et al. [12] on the shear behaviour of hybrid SHCC-RC slender beams without transverse reinforcement and with a precast SHCC U-shaped formwork failed at a load of 78.2 kN, whilst the failure load of the hybrid beams varied between 113.9-142.9 kN, depending on the interfacial properties and thickness of the formwork. The beams with a SHCC formwork thickness of 20 mm had a lower shear capacity compared to the beams with a formwork thickness of 15 mm. The interface conditions seem to have played an important role in the activation of the SHCC. The interface condition between the concrete and 3D printed beam in this research was sufficient to prevent a large debonding length and activate most of the SHCC, which resulted in a higher shear capacity compared to the other beams.

The hybrid beams have a significantly larger energy absorption capacity E_{abs} and post-cracking shear ductility compared to the control beam. The hybrid beam exhibited larger deformation capacity and the failure was more ductile compared to the control beam, due to the strain-hardening property of SHCC. The first diagonal crack $F_{diagonal}$ was higher for the hybrid beams, because the higher compressive strength of SHCC delayed the formation of shear cracks. The unintended larger SHCC formwork thickness of 3DHB2 and superior tensile properties of HBTL2 caused the first diagonal crack to appear at a slightly higher load compared to HBT2. When the post-cracking ductility is defined as the ratio of the deflection corresponding to the 85% post-peak load $u_{85\%}$ over the deflection at the first diagonal crack $u_{diagonal}$, then the ductility of the hybrid beams was found to be larger compared to the control beam. Especially $u_{85\%}$ of the hybrid beams is very large, because the load drops relatively slowly in post-peak compared to the control beam as a result of PE fibres still bridging the fine shear cracks and providing additional resistance.

7.2.2 Cracking pattern

The SHCC U-shaped formwork can turn the dominant shear cracks in the concrete into multiple fine cracks. This cracking behaviour improved the post-cracking ductility and energy absorption capacity in the hybrid beams. Moreover, the cracking behaviour of the hybrid beam with a 3D printed SHCC U-shaped formwork differentiates from the hybrid beams with a precast formwork. The diagonal cracks propagate with small jumps along the interface of the printed filaments towards the loading points. This is because the interface of the printed filaments is relatively weak, due to the low amount of fibres which bridge consecutive printed filaments. The unique cracking behaviour led to a smaller shear crack angle, thus the amount of PE fibres bridging the shear cracks increased. This will increase the post-crack shear resistance.

The growth rate of existing diagonal cracks did fluctuate as a result of redistribution of internal forces, especially in the hybrid beams. Sudden jumps in growth rate of cracks mainly occurred at the formation of new diagonal cracks, but were also visible in existing cracks. The fluctuation in the growth rate of cracks was also observed in literature. Budnik [97] investigated the shear behaviour of hybrid SHCC-RC beams with SHCC lamellas applied laterally. The lamellas had a profiled surface with circular shear keys. The major strain rate evolution of the dominant shear cracks in the hybrid beams without transverse reinforcement had sudden jumps which indicates quick redistribution of internal forces. The main diagonal cracks experienced accelerated growth in a short time period before reverting to slower growth rates. Hence, this indicates that a lot of the load was redistributed to the concrete and that the SHCC could not be activated to a full extent. It seems that the shear contribution and activation of SHCC in hybrid SHCC-RC beams is limited due to the difference elastic modulus of SHCC and concrete.

8. Conclusion

The main objective of this thesis is to find a method for effectively applying SHCC in new reinforced concrete structures. The method explored in this thesis consists of a SHCC U-shaped lost formwork for reinforced concrete beams. The influence of the hybrid configuration on the load capacity, cracking pattern, crack control and post-cracking shear ductility was investigated. The findings in this study indicate that SHCC can effectively improve the structural response of a RC beam. More specifically:

- Strain-hardening behaviour of fibre-reinforced cementitious materials is possible with a PE-fibre volume fraction of 1%.
- An U-shaped SHCC formwork enhances the bending capacity of a hybrid beam. The reference beam had a capacity of 98.3 kN, whilst the SHCC-RC hybrid beams failed at 145.1 kN, 152.4 kN and 159.1 kN.
- An U-shaped SHCC formwork can slightly improve the shear resistance of RC beams without transverse reinforcement, depending on the elastic modulus of SHCC. The SHCC-RC hybrid members with a precast formwork showed a 0% to 9.5% higher peak load than the control beam.
- The maximum crack width could be reduced significantly through utilising an U-shaped SHCC permanent formwork. A crack of 0.3 mm localised at 48.3 kN load in the control beam, before yielding of the reinforcement, whereas in the hybrid beams the largest crack exceeded 0.3 mm at 119.0 kN, 124.6 kN and 137.3 kN, either during or after yielding of the reinforcement. This means the steel reinforcement is used more efficiently.
- The post-cracking shear ductility and energy absorption capacity of RC beams is improved by applying SHCC as formwork. The DF of the reference beam was 8.54, whereas the DF of all the hybrid beams were above 11.
- A deliberately weak SHCC-concrete interface can increase the cracking zone in the SHCC and improve SHCC activation. The interface property of a 3D printed SHCC formwork has sufficient debonding length to promote the activation of SHCC. For comparison, in the 3D printed formwork, 60 cracks formed, 25 mm above the bottom, whereas only 46 cracks were formed in the precast formwork with profiled interface.
- The MLM could predict the failure load of the reference beam accurately. The experimental load was overestimated by 4.0%. However, the failure load of the hybrid beam with transverse shear keys was underestimated by 17.0%. Also, the experimental and predicted midspan deflections of the reference and hybrid beams deviate a lot. The MLM is based on beam theory and hence, not accurate in predicting the shear capacity of deep beams.
- The shear capacity of the beams with a precast SHCC U-shaped formwork could be predicted accurately with a strut-and-tie model, despite the model not taking interfacial properties into consideration. The experimental and predicted load of the hybrid beam was 103.7 kN and 110.6 kN, respectively. The downside of the model is that it is very sensitive to the value for the width of the diagonal strut.

9. Recommendation

The maximum crack width of concrete is correlated to the occurrence of concrete deteriorating mechanisms such as corrosion of embedded steel reinforcement, hence utilizing SHCC as formwork for RC structures can benefit the durability of concrete structures and potentially reduce the amount of reinforcement. However, the results of this study do not represent the effect of SHCC on real concrete structures, since the experimental tests were conducted on small specimens with a relative high amount of SHCC per unit of volume concrete. The benefit of SHCC on bending and shear capacity of larger concrete structures will be neglectable. The effectiveness of SHCC on the crack control and cracking pattern is highly dependent on the interfacial properties and elastic modulus, which are not addressed in this thesis. For this reason, it is recommended for future research to study the influence of interfacial properties and elastic modulus in hybrid SHCC-concrete structures. Additionally, further research can be done to design and optimize the SHCC mixture used in this thesis. An improvement in mechanical properties of SHCC will have a noticeable effect on the structural response. The effect of 3D printing could not be fully explored in this research, due to the unintended deviation in the SHCC formwork thickness. It is recommended to further investigate how 3D printing parameters affects the structural response of SHCC-RC hybrid structures.

Appendix A : Design of experiments

Bending test

Bending resistance

The control beam specimen is made of reinforced concrete. The beam is designed to prevent shear failure and achieve flexural failure. The occurring bending moment M_e on a simply supported beam with two concentrated point loads is equal to (A1).

$$M_e = \frac{F_b}{2} a_v \tag{A1}$$

The bending moment resistance of the beam can be determined by considering the equilibrium of forces in the beam at moment of failure (Figure A.1).

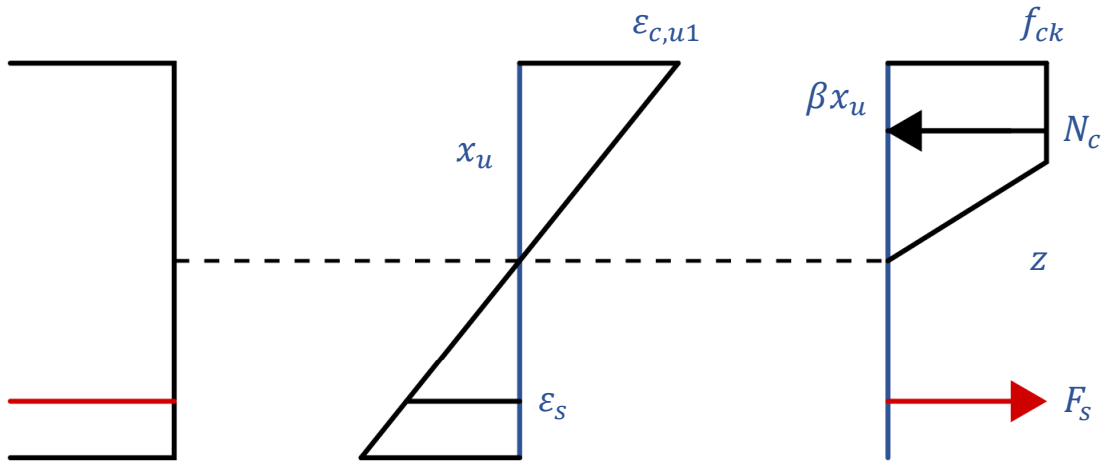

Figure A.1 Equilibrium of forces at bending failure.

When the force in the concrete compression zone N_c (A2) is set equal to the force in the reinforcing steel F_s (A5), the concrete compression zone x_u can be determined.

$$N_c = \alpha x_u f_{cm} b_w \tag{A2}$$

$$\varepsilon_s = \frac{\varepsilon_{c,u1}}{x_u}(h - x_u - c) \tag{A3}$$

$$\sigma_s = \frac{\varepsilon_s - \varepsilon_{s,y}}{\varepsilon_{s,uk} - \varepsilon_{s,y}}\left(f_{s,u} - f_{s,y}\right) + f_{s,y} \tag{A4}$$

$$F_s = A_{sl}\sigma_s \tag{A5}$$

With:

$$\alpha = \frac{\varepsilon_{c,u1} - \varepsilon_{c,3} + \frac{\varepsilon_{c,3}}{2}}{\varepsilon_{c,u1}}$$

$$A_{sl} = \frac{2}{4}\pi \emptyset_l^2$$

After the value of the compression zone is found, the stress in the steel σ_s is checked. The stress in the reinforcing steel cannot exceed the steel ultimate strength $f_{s,u}$.

$$\sigma_s \leq f_{s,u} \quad \text{(A6)}$$

$$M_y > M_{cr,c} \quad \text{(A7)}$$

With:

$$M_{cr,c} = f_{ctm,fl} * W$$

$$W = \frac{1}{6} b h^2$$

If condition (A6) is not satisfied, the input parameters are adjusted until this condition is satisfied. Also, it is of importance that the reinforcing steel does not yield immediately after the concrete has cracked to ensure a ductile failure mechanism (A7).

The lever arm between the concrete compression force N_c and steel force F_s can be computed with (A8).

$$z = d - \beta x_u \quad \text{(A8)}$$

With:

$$d = h - c - \emptyset_{sw} - \frac{1}{2}\emptyset_l$$

β is a coefficient which can be determined by calculating the centroid of the area under the stress diagram of concrete (Figure 27a). The bending moment resistance of the cross section is simply the product of the lever arm and the force $N_c = F_s$.

$$M_r = N_c z \quad \text{(A9)}$$

$$M_r = M_e \rightarrow \qquad F_b = \frac{2M_r}{a_v} \quad \text{(A10)}$$

The bending resistance in terms of the point load F_b can be determined by equating the occurring bending moment and bending moment resistance (A10).

Shear resistance

The four-point bending test is designed to prevent shear failure. Hence, the shear resistance should be larger than occurring shear force V_e when the point load is equal to F_b (A11).

The maximum shear force in the 4P bending setup depends on the bending resistance F_b

$$V_e = \frac{F_b}{2}$$

The shear resistance of concrete V_{rc} is determined with (A12).

$$V_{rc} = C_{rc} k (100 \rho_l f_{ck})^{\frac{1}{3}} b_w d \geq V_{min} \quad \text{(A12)}$$

Where:

$$k = 1 + \sqrt{\frac{200}{d}} \leq 2$$

$$\rho_l = \frac{A_{sl}}{b_w d} \leq 0.02$$

$$C_{rc} = 0.18$$

$$V_{min} = 0.035 k^{\frac{3}{2}} f_{ck}^{\frac{1}{2}} b_w d$$

The shear resistance of concrete has a minimum vale V_{min}. In case $V_e \geq V_{rc}$, shear reinforcement is necessary. The contribution of the concrete to the shear resistance is neglected when applying shear reinforcement. The shear resistance of the shear reinforcement is calculated with (A13).

$$V_{rs} = \frac{A_{sw}}{s_w} f_{ywk} \cot(\theta)\, z \leq V_{rmax} \quad \text{(A13)}$$

$$V_{rs} = V_e \quad \text{(A14)}$$

Where:

$$A_{sw} = 2 * \frac{1}{4} \pi \emptyset_{sw}^2$$

$$\theta = 45°$$

$$V_{rmax} = \frac{v_1 \alpha_{cw} b_w z f_{ck}}{\cot(\theta) + \tan(\theta)}$$

$$v_1 = 0.6$$

$$\alpha_{cw} = 1$$

The required amount of shear reinforcement A_{sw}/s_w to prevent shear failure in the control beam can be determined through equating the resistance of the shear reinforcement V_{rs} with V_e (A14).

Shear test

Bending resistance

The control beam specimen is designed to prevent flexural failure and achieve shear failure in ULS. The occurring bending moment M_e on a simply supported beam with one concentrated point load at mid span is equal to (A15). F_w is the total load on the beam specimen in the 3P bending test.

$$M_e = \frac{F_w}{2} a_v \quad \text{(A15)}$$

The bending moment resistance of the beam can be determined by considering the equilibrium of forces at moment of failure (Figure A.1). The force in the concrete compression zone N_c and force in the steel F_s are set equal to calculate the depth of the concrete compression zone x_u.

$$N_c = \alpha x_u f_{ck} b_w \quad \text{(A16)}$$

$$\varepsilon_s = \frac{\varepsilon_{c,u1}}{x_u} (d - x_u) \quad \text{(A17)}$$

$$F_s = \frac{A_{sl} \sigma_s}{\gamma_s} \quad \text{(A18)}$$

With:

$$\alpha = \frac{\varepsilon_{c,u1} - \varepsilon_{c,3} + \frac{\varepsilon_{c,3}}{2}}{\varepsilon_{c,u1}}$$

$$A_{sl} = \frac{2}{4}\pi\emptyset_l^2$$

σ_s (See (A4))

Again, conditions (A6) and (A7) should be satisfied. If these conditions are satisfied, the bending resistance of the cross section can be determined in a similar way as in the 4P bending test with (A8) and (A9). The characteristic resistance to bending in terms of the point load F_w is then determined with (A19).

$$M_r = M_e \rightarrow \qquad F_w = \frac{2M_r}{a_v} \tag{A19}$$

Shear resistance

The beam specimen needs to be underdesigned in shear to achieve shear failure in the 3P bending test. In other words, the shear resistance of the control beam needs to be lower than the occurring shear force V_e when the load is F_w (A20).

$$V_e = \frac{F_w}{2} \tag{A20}$$

The calculation of the shear resistance of the concrete cross section goes in a similar way as explained in the 4P bending test (A12).

In case $V_e > V_{rc}$, the beam will fail in shear.

Appendix B: Manufacturing of SHCC formwork

Some experiments are carried out in the lab to determine an appropriate method to manufacture the U-shaped SHCC formwork. The experiments are inspired by a previous graduation work [9]. In this study, small and medium scale experiments were performed to find a way of making an U-shaped formwork with smooth surface. In the experiments [9], different materials for the outer and inner formwork were tested. The best results were obtained with a steel outer formwork and inner formwork made of extruded polystyrene (XPS). XPS has a closed cell structure and is hence, stronger than other foam material such as expanded polystyrene (EPS). The Styrofoam inner mould was completely wrapped with tape to prevent the foam from sticking to the SHCC during demoulding. In this way it was possible to demould the inner mould with a crowbar without the need to demolish the Styrofoam after the whole mould was turned upside down. The outer and inner Styrofoam mould were attached with double-sided tape.

To a large extent, the same procedure as described in [9] is used for making a SHCC U-shaped formwork. However, some aspects are different. Creating shear keys at the web and flange surface of the SHCC formwork makes the process more complex. For this reason, some trial-based experiments were performed to uncover possible difficulties in the manufacturing of the formwork and find solutions for them.

First trial experiment

At this phase of the thesis, the final SHCC mix design was not determined yet, so an alternative mix design was adopted with PVA fibres (Table B.1). It should be noted that this SHCC mix design is not optimized in terms of printability, but in terms of ductility. An inner mould of low-quality Styrofoam (EPS60) was made with available material from the lab (Figure B.1). The inner mould consists of 10 mm thick foam plates which are taped together with continuous double-sided tape. The plates are manually sawn with a Stanley knife. In the outer plates of the Styrofoam, holes with a diameter of 25 mm were drilled to facilitate the shear keys. The Styrofoam was attached to the wooden mould with double-sided

CEM III/B 42.5R	Limestone Powder	Water	SP	PVA
1050	525	420	2.4	26

Table B.1 Mix composition 1st trial SHCC U-shaped formwork (Unit = kg/m3).

tape and the surface of the inner and outer mould were treated with oil to ease the demoulding (Figure B.2a). The inner mould was not placed symmetrically, but at an angle to create different thicknesses along the web. The wooden mould was demoulded after 4 days of hardening (Figure B.2c). It was observed that the inside Styrofoam did not float during casting. However, it seemed very difficult to detach the Styrofoam from the wooden mould with a chisel due to the amount of tape and tape's stickiness. Some other issues were encountered as well, during demoulding. After separating the wooden outer mould from the SHCC U-shape, hardened SHCC was found at the location of the double-sided tape. This indicates some leakage occurred during casting, likely because the height of the plates were not uniform. It was noticed that the fresh SHCC mix was not able to fill the shear key holes in the

Figure B.1. Inner Styrofoam mould used in the first trial U-shape experiment.

Styrofoam when the web thickness was less than 10 mm. In case of a higher web thickness, it was possible to fill the holes and create transverse shear keys (Figure B.3). The shear keys are very rough and have a low dimension conformity and consistency due to the relative low cell-density of the Styrofoam. The hypothesis is that with a higher quality Styrofoam, a higher dimension conformity and consistency of the shear keys can be achieved.

(a) (b) (c)

Figure B.2. Steps in the casting session: before casting (a), after casting (b) and after demoulding the outer formwork (c).

Figure B.3. Shear keys on the surface of the U-shaped SHCC formwork after removing Styrofoam.

Second trial experiment

A second trial experiment was performed to cast an inverted U-shaped beam with a flange/web thickness of 15 mm. This time the inner mould is made of vertical extruded polystyrene (XPS) plates. This type of Styrofoam has a higher compressive strength compared to EPS60. The hypothesis was that using a higher quality Styrofoam will allow the inner mould to be removed by applying an upward pressure, without needing to demolish the inner mould, in a similar way as was done in [9]. This will save a lot of time when demoulding the formwork. The inner mould consists of six XPS plates with a thickness of 20 mm, put side by side and wrapped with tape (Figure B.4). Holes with a diameter of 25 mm and a depth of 10 mm were drilled in the two outer plates to facilitate shear keys in the web.

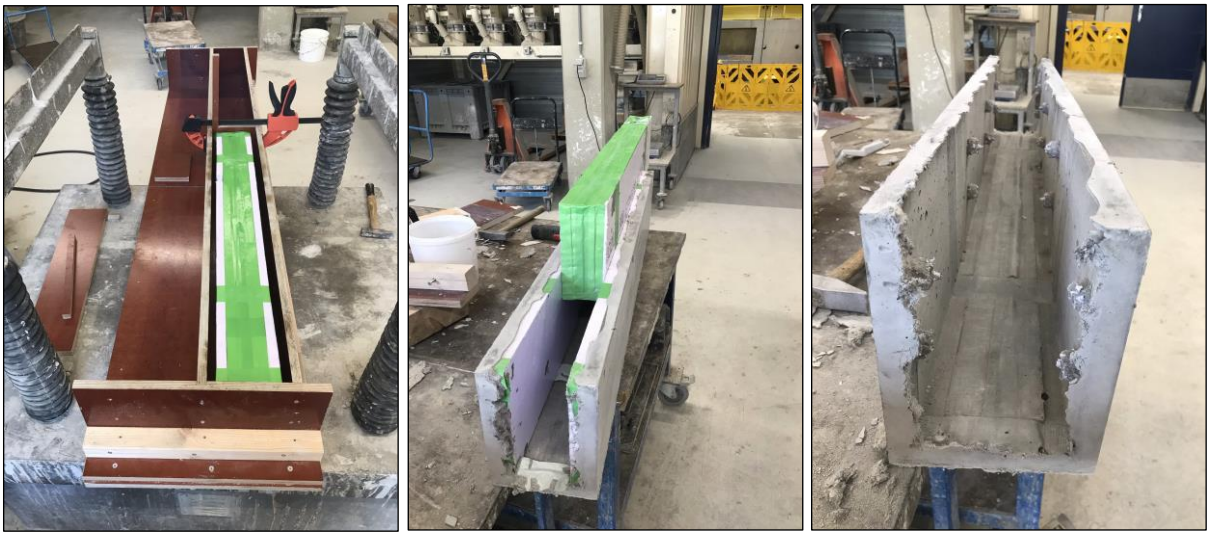

(a) (b) (c)

Figure B.4. Steps in the casting session: before casting (a), removing the inner mould (b) and final result (c).

A layer of silicon glue was applied on the interface between the inner mould and outer wooden mould to keep the inner mould stable during the casting phase. Lubricant spray was applied on the surface of the wooden mould and XPS mould to ease the demould process. In addition, Vaseline was applied on the interface between the outer and inner XPS plates in order to reduce the friction and easily

remove the Styrofoam mould with a crowbar (Figure B.4b) Compared to the first trial experiment, it became less complicated to separate the wooden mould from the SHCC formwork due to using silicon glue instead of tape. The rest of the Styrofoam could be removed intact (Figure B.4c).

Some minor problems occurred during the second trial experiment. It was noticed that during casting, the inner XPS mould moved due to the unevenly distribution of flowable material in the webs. This can be prevented if the casting is done more thoughtful. Another point of concern related to the casting is the presence of air bubbles at the surface of the webs. To reduce the amount of air bubbles, more time should be spent on the vibration process.

Appendix C: Elastic modulus of concrete

The concrete stabilized secant modulus of elasticity $E_{c,s}$ is determined according to method B of NEN-EN 12390-13 [93]. Three preloading cycles (Figure C.1) were carried out on two concrete prisms (Pr4P and Pr3P) with dimensions 100x100x400 mm at an age of 37 days. The composition of the concrete is mentioned in Table 5. Four LVDTs are placed on the sides of the prism to measure the vertical displacements (Figure C.2). The measuring zone is 135 mm. The prisms were sealed and cured in a dry environment at room temperature (20 ± 2 °C). This deviates from what is specified in NEN-EN 12390-2 [108] to make the curing conditions of the test specimens and beams similar. The compressive strength of the concrete prism f_c is based on destructive tests on concrete cubes of 150x150x150 mm with the same curing conditions as the prisms. A conversion factor of 1.0 is assumed.

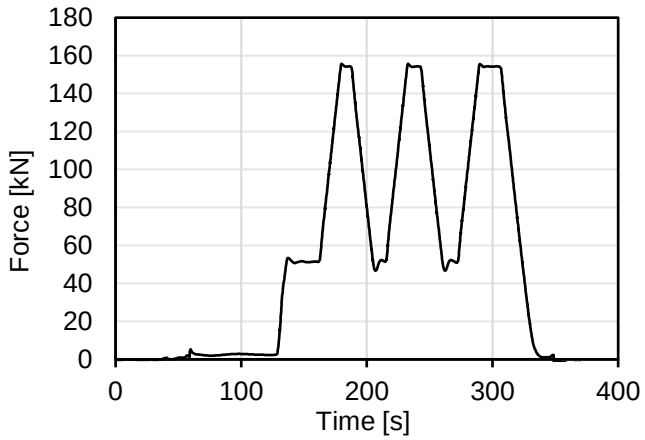

Figure C.1. Load cycles for the concrete prisms.

	C4P		C3P	
f_c	46	MPa	46	MPa
F_a	154	kN	154	kN
$F_{b,1}$	51	kN	51	kN
F_p	51	kN	51	kN
Load rate	6	kN/s	6	kN/s
$E_{c,s}$	38,638	MPa	38,192	MPa

Figure C.2. Non-destructive test setup and parameters used to determine the concrete elastic modulus.

Appendix D: Verification DIC results

Bending

The results of the DIC analysis from the bending test are verified with the LVDT data (Figure D.1). The DIC results of all the beams agree with the data from LVDT01.

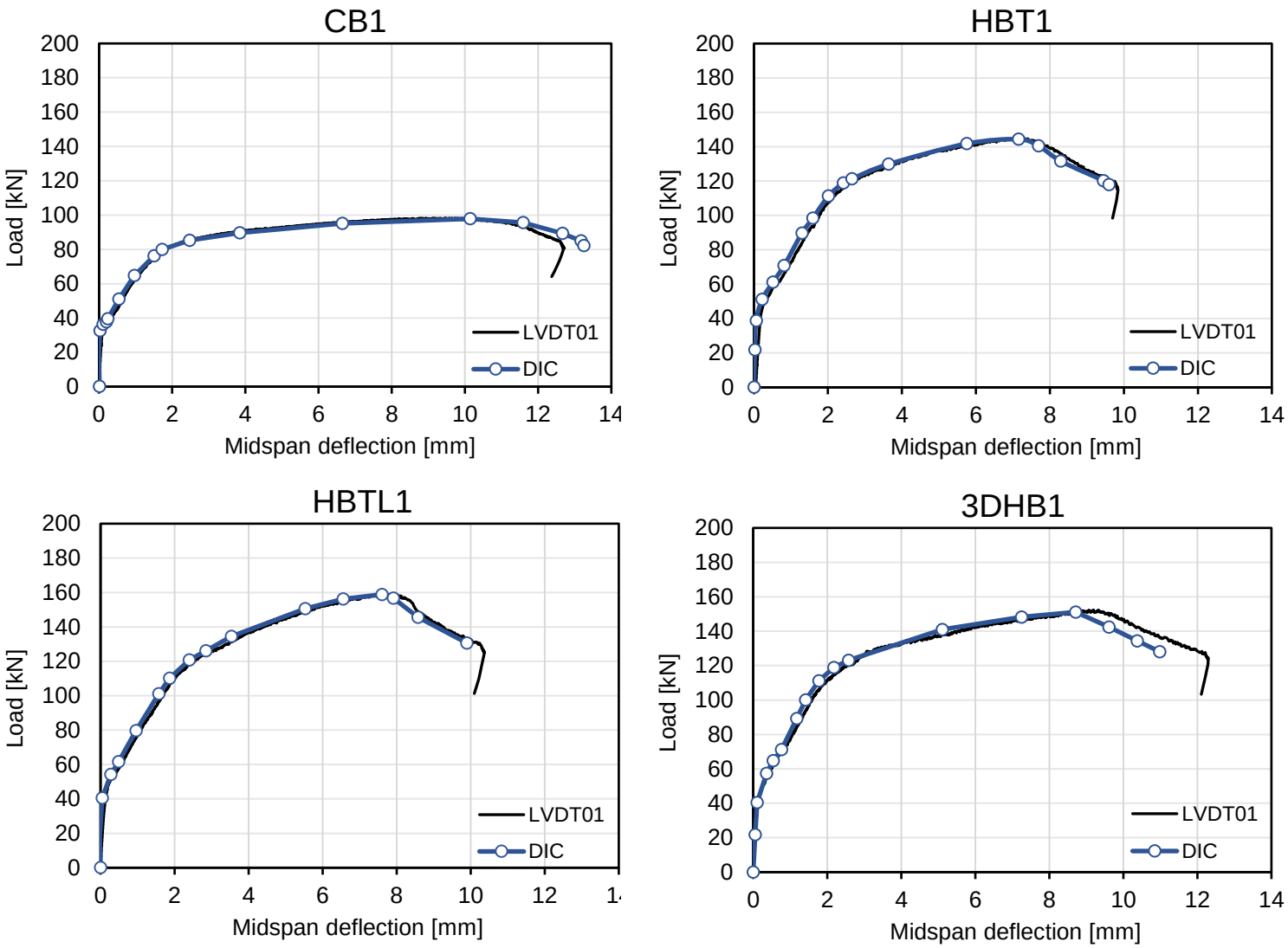

Figure D.1. Verification DIC results bending test.

Shear

The results of the DIC analysis are verified using the data from the LVDTs. The positions of LVDTs are displayed in Figure 51. The DIC results are in agreement with the data from LVDT01 (Figure D.2) and LVDT02 (Figure D.3), which measured the relative horizontal displacement in the compression zone The strange results from the DIC analysis and LVDT02 in beam 3DHB2 (Figure D.3) are caused by movement of the LVDT holders. The surface texture of the printed filaments made it difficult to glue the holders on the beam in a stable position.

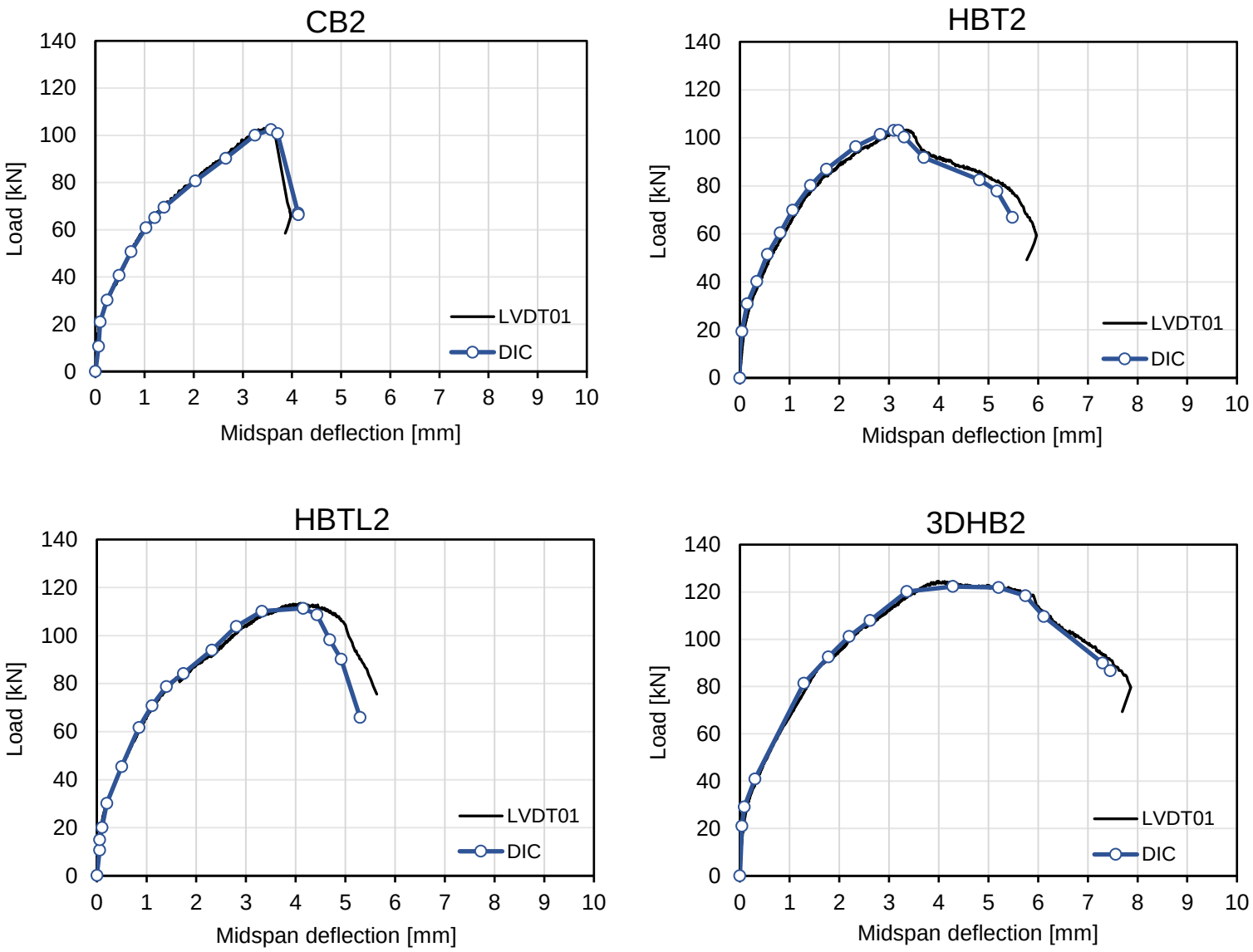

Figure D.2. Verification DIC results of shear test with data from LVDT01.

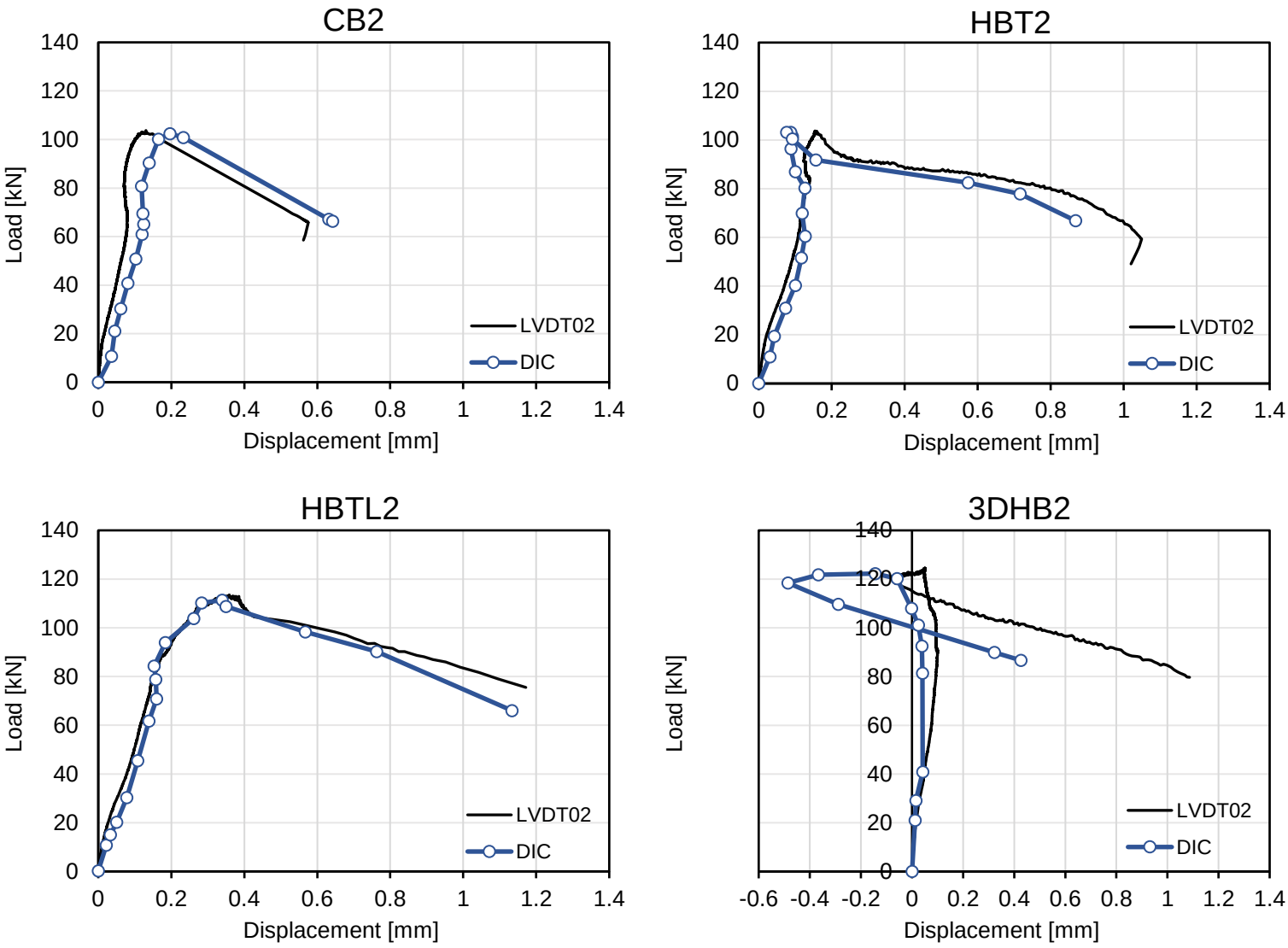

Figure D.3. Verification DIC results of shear test with data from LVDT02.

References

[1] *Eurocode 2: Design of concrete structures - Part 1-1: General rules and rules for buildings* NEN, Delft, 2005.

[2] S. Wang and V. C. Li, "Polyvinyl alcohol fiber reinforced engineered cementitious composites: material design and performances," in *Proc., Int'l Workshop on HPFRCC Structural Applications, Hawaii*, 2005: Citeseer.

[3] P. Jun and V. Mechtcherine, "Behaviour of strain-hardening cement-based composites (SHCC) under monotonic and cyclic tensile loading: part 1–experimental investigations," *Cement and Concrete Composites,* vol. 32, no. 10, pp. 801-809, 2010.

[4] M. Luković, D. Hordijk, Z. Huang, and E. Schlangen, "Strain Hardening Cementitious Composite (SHCC) for crack width control in reinforced concrete beams," *Heron,* vol. 64, no. 1/2, p. 181, 2019.

[5] J. Wei, C. Wu, Y. Chen, and C. K. Leung, "Shear strengthening of reinforced concrete beams with high strength strain-hardening cementitious composites (HS-SHCC)," *Materials and Structures,* vol. 53, no. 4, pp. 1-15, 2020.

[6] G. Wang *et al.*, "Shear behaviors of RC beams externally strengthened with engineered cementitious composite layers," *Materials,* vol. 12, no. 13, p. 2163, 2019.

[7] Y. Zhang, S. Bai, Q. Zhang, and X. Zhang, "Failure behavior of strain hardening cementitious composites for shear strengthening RC member," *Construction and Building Materials,* vol. 78, pp. 470-473, 2015.

[8] G. P. A. G. Van Zijl and F. H. Wittmann, *Durability of strain-hardening fibre-reinforced cement-based composites (SHCC)*. Springer Science & Business Media, 2010.

[9] A. Yassiri, "Reinforced hybrid concrete beams with a U-shaped SHCC mould: Developing the system and extending the multi-layer model to predict its bending behaviour," 2020.

[10] S. H. Bong, B. Nematollahi, V. Mechtcherine, V. C. Li, and K. H. Khayat, "3D Printed Engineered, Strain-Hardening Geopolymer Composite (EGC/SHGC) as Permanent Formwork for Concrete Beam Construction," 2022.

[11] J. Tian *et al.*, "Investigation of interface shear properties and mechanical model between ECC and concrete," *Construction and Building Materials,* vol. 223, pp. 12-27, 2019.

[12] R. Zhang, P. Hu, X. Zheng, L. Cai, R. Guo, and D. Wei, "Shear behavior of RC slender beams without stirrups by using precast U-shaped ECC permanent formwork," *Construction and Building Materials,* vol. 260, p. 120430, 2020.

[13] Z. Huang, "Flexural behaviour of reinforced concrete beams with a layer of SHCC in the tension zone: Experimental Study," 2017.

[14] N. Zhang and K.-H. Tan, "Direct strut-and-tie model for single span and continuous deep beams," *Engineering Structures,* vol. 29, no. 11, pp. 2987-3001, 2007.

[15] R. Li, M. Deng, Y. Zhang, and D. Wei, "Shear strengthening of reinforced concrete deep beams with highly ductile fiber-reinforced concrete jacket," *Journal of Building Engineering,* vol. 48, p. 103957, 2022.

[16] A. B. Shuraim and A. K. El-Sayed, "Experimental verification of strut and tie model for HSC deep beams without shear reinforcement," *Engineering Structures,* vol. 117, pp. 71-85, 2016.

[17] V. C. Li, S. Wang, and C. Wu, "Tensile strain-hardening behavior of polyvinyl alcohol engineered cementitious composite (PVA-ECC)," *Materials Journal,* vol. 98, no. 6, pp. 483-492, 2001.

[18] B. Y. Lee, J.-K. Kim, and Y. Y. Kim, "Prediction of ECC tensile stress-strain curves based on modified fiber bridging relations considering fiber distribution characteristics," *Computers & Concrete,* vol. 7, no. 5, pp. 455-468, 2010.

[19] A. V. Georgiou and S. J. Pantazopoulou, "Behavior of strain hardening cementitious composites in flexure/shear," *Journal of Materials in Civil Engineering,* vol. 29, no. 10, p. 04017192, 2017.

[20] P. S. Bhat, V. Chang, and M. Li, "Effect of elevated temperature on strain-hardening engineered cementitious composites," *Construction and Building Materials,* vol. 69, pp. 370-380, 2014.

[21] V. C. Li, C. Wu, S. Wang, A. Ogawa, and T. Saito, "Interface tailoring for strain-hardening polyvinyl alcohol-engineered cementitious composite (PVA-ECC)," *Materials Journal,* vol. 99, no. 5, pp. 463-472, 2002.

[22] K. Yu, Y. Wang, J. Yu, and S. Xu, "A strain-hardening cementitious composites with the tensile capacity up to 8%," *Construction and Building Materials,* vol. 137, pp. 410-419, 2017.

[23] K. Yu, L. Li, J. Yu, Y. Wang, J. Ye, and Q. Xu, "Direct tensile properties of engineered cementitious composites: A review," *Construction and Building Materials,* vol. 165, pp. 346-362, 2018.

[24] M. Li, "Multi-scale design for durable repair of concrete structures," University of Michigan, 2009.

[25] P. Nallathambi, B. Karihaloo, and B. Heaton, "Effect of specimen and crack sizes, water/cement ratio and coarse aggregate texture upon fracture toughness of concrete," *Magazine of concrete research,* vol. 36, no. 129, pp. 227-236, 1984.

[26] E.-H. Yang, Y. Yang, and V. C. Li, "Use of high volumes of fly ash to improve ECC mechanical properties and material greenness," *ACI materials journal,* vol. 104, no. 6, pp. 620-628, 2007.

[27] C. Jin *et al.*, "Mechanical properties of high-volume fly ash strain hardening cementitious composite (hvfa-shcc) for structural application," *Materials,* vol. 12, no. 16, p. 2607, 2019.

[28] V. Li and M. Lepech, "Engineered cementitious composites: Design, performance and applications," ed: ibidem Verlag, Stuttgart, Germany, 2005, pp. 99-120.

[29] P. Wang *et al.*, "Research on bonding and shrinkage properties of SHCC-repaired concrete beams," *Materials,* vol. 13, no. 7, p. 1757, 2020.

[30] M. Lukovic, "Influence of interface and strain hardening cementitious composite (SHCC) properties on the performance of concrete repairs," 2016.

[31] M. Luković, H. Dong, B. Šavija, E. Schlangen, G. Ye, and K. van Breugel, "Tailoring strain-hardening cementitious composite repair systems through numerical experimentation," *Cement and Concrete Composites,* vol. 53, pp. 200-213, 2014.

[32] G. P. Van Zijl and V. Slowik, *A framework for durability design with strain-hardening cement-based composites (SHCC): state-of-the-art report of the RILEM technical committee 240-FDS*. Springer, 2017.

[33] S. Singh, "Influence of Interface and Type of Strain Hardening Cementitious Composite (SHCC) on Crack Control in SHCC-Concrete Hybrid Beams," 2019.

[34] M. Kunieda and K. Rokugo, "Recent progress on HPFRCC in Japan," *Journal of Advanced Concrete Technology,* vol. 4, no. 1, pp. 19-33, 2006.

[35] V. Mechtcherine, V. Slowik, and P. Kabele, *Strain-hardening cement-based composites: SHCC4*. Springer, 2017.

[36] M. D. Lepech and V. C. Li, "Long Term Durability Performance of Engineered Cementitious Composites/Langzeitbeständigkeit systematisch entwickelter zusammengesetzter Zement gebundener Werkstoffe," *Restoration of Buildings and Monuments,* vol. 12, no. 2, pp. 119-132, 2006.

[37] K. Rokugo, M. Kunieda, and S. Lim, "Patching repair with ECC on cracked concrete surface," *Proceedings of ConMat,* vol. 5, pp. 22-24, 2005.

[38] J. Zhang, J. Wang, S. Dong, X. Yu, and B. Han, "A review of the current progress and application of 3D printed concrete," *Composites Part A: Applied Science and Manufacturing,* vol. 125, p. 105533, 2019.

[39] F. Asdrubali, S. Schiavoni, and K. Horoshenkov, "A review of sustainable materials for acoustic applications," *Building Acoustics,* vol. 19, no. 4, pp. 283-311, 2012.

[40] G. De Schutter, K. Lesage, V. Mechtcherine, V. N. Nerella, G. Habert, and I. Agusti-Juan, "Vision of 3D printing with concrete—Technical, economic and environmental potentials," *Cement and Concrete Research,* vol. 112, pp. 25-36, 2018.

[41] M. K. Mohan, A. Rahul, K. Van Tittelboom, and G. De Schutter, "Rheological and pumping behaviour of 3D printable cementitious materials with varying aggregate content," *Cement and Concrete Research,* vol. 139, p. 106258, 2021.

[42] C. Zhang *et al.*, "Mix design concepts for 3D printable concrete: A review," *Cement and Concrete Composites,* vol. 122, p. 104155, 2021.

[43] R. M. Andrew, "Global CO 2 emissions from cement production," *Earth System Science Data,* vol. 10, no. 1, pp. 195-217, 2018.

[44] J. Xiao *et al.*, "3D recycled mortar printing: System development, process design, material properties and on-site printing," *Journal of Building Engineering,* vol. 32, p. 101779, 2020.

[45] B. Panda, C. Unluer, and M. J. Tan, "Investigation of the rheology and strength of geopolymer mixtures for extrusion-based 3D printing," *Cement and Concrete Composites,* vol. 94, pp. 307-314, 2018.

[46] S. H. Bong, M. Xia, B. Nematollahi, and C. Shi, "Ambient temperature cured ‘just-add-water’geopolymer for 3D concrete printing applications," *Cement and Concrete Composites,* vol. 121, p. 104060, 2021.

[47] S. Muthukrishnan, H. W. Kua, L. N. Yu, and J. K. Chung, "Fresh properties of cementitious materials containing rice husk ash for construction 3D printing," *Journal of Materials in Civil Engineering,* vol. 32, no. 8, p. 04020195, 2020.

[48] S. Lim, R. A. Buswell, T. T. Le, S. A. Austin, A. G. Gibb, and T. Thorpe, "Developments in construction-scale additive manufacturing processes," *Automation in construction,* vol. 21, pp. 262-268, 2012.

[49] G. Ma and L. Wang, "A critical review of preparation design and workability measurement of concrete material for largescale 3D printing," *Frontiers of Structural and Civil Engineering,* vol. 12, no. 3, pp. 382-400, 2018.

[50] Y. Chen, S. He, Y. Gan, O. Çopuroğlu, F. Veer, and E. Schlangen, "A review of printing strategies, sustainable cementitious materials and characterization methods in the context of extrusion-based 3D concrete printing," *Journal of Building Engineering,* vol. 45, p. 103599, 2022.

[51] Y. W. D. Tay, Y. Qian, and M. J. Tan, "Printability region for 3D concrete printing using slump and slump flow test," *Composites Part B: Engineering,* vol. 174, p. 106968, 2019.

[52] *C1437 − 15* ASTM, West Conshohocken, 2015.

[53] R. A. Buswell, W. L. De Silva, S. Z. Jones, and J. Dirrenberger, "3D printing using concrete extrusion: A roadmap for research," *Cement and Concrete Research,* vol. 112, pp. 37-49, 2018.

[54] S. C. Figueiredo *et al.*, "An approach to develop printable strain hardening cementitious composites," *Materials & Design,* vol. 169, p. 107651, 2019.

[55] A. Perrot, D. Rangeard, V. N. Nerella, and V. Mechtcherine, "Extrusion of cement-based materials-an overview," *RILEM Technical Letters,* vol. 3, pp. 91-97, 2018.

[56] V. Mechtcherine, V. N. Nerella, F. Will, M. Näther, J. Otto, and M. Krause, "Large-scale digital concrete construction–CONPrint3D concept for on-site, monolithic 3D-printing," *Automation in construction,* vol. 107, p. 102933, 2019.

[57] A. Kazemian, X. Yuan, E. Cochran, and B. Khoshnevis, "Cementitious materials for construction-scale 3D printing: Laboratory testing of fresh printing mixture," *Construction and Building Materials,* vol. 145, pp. 639-647, 2017.

[58] B. Panda, G. B. Singh, C. Unluer, and M. J. Tan, "Synthesis and characterization of one-part geopolymers for extrusion based 3D concrete printing," *Journal of cleaner production,* vol. 220, pp. 610-619, 2019.

[59] X. Zhou and Z. Li, "Manufacturing cement-based materials and building products via extrusion: from laboratory to factory," in *Proceedings of the Institution of Civil Engineers-Civil Engineering*, 2015, vol. 168, no. 6: Thomas Telford Ltd, pp. 11-16.

[60] Q. Yuan, D. Zhou, K. H. Khayat, D. Feys, and C. Shi, "On the measurement of evolution of structural build-up of cement paste with time by static yield stress test vs.

small amplitude oscillatory shear test," *Cement and Concrete Research,* vol. 99, pp. 183-189, 2017.

[61] R. Wolfs, F. Bos, and T. Salet, "Hardened properties of 3D printed concrete: The influence of process parameters on interlayer adhesion," *Cement and Concrete Research,* vol. 119, pp. 132-140, 2019.

[62] A. Perrot, D. Rangeard, and Y. Mélinge, "Prediction of the ram extrusion force of cement-based materials," *applied rheology,* vol. 24, no. 5, pp. 34-40, 2014.

[63] Y. Chen *et al.*, "Improving printability of limestone-calcined clay-based cementitious materials by using viscosity-modifying admixture," *Cement and Concrete Research,* vol. 132, p. 106040, 2020.

[64] L. Patural, P. Marchal, A. Govin, P. Grosseau, B. Ruot, and O. Deves, "Cellulose ethers influence on water retention and consistency in cement-based mortars," *Cement and Concrete research,* vol. 41, no. 1, pp. 46-55, 2011.

[65] D. Marchon, S. Kawashima, H. Bessaies-Bey, S. Mantellato, and S. Ng, "Hydration and rheology control of concrete for digital fabrication: Potential admixtures and cement chemistry," *Cement and Concrete Research,* vol. 112, pp. 96-110, 2018.

[66] J. He, C. Cheng, X. Zhu, and X. Li, "Effect of Silica Fume on the Rheological Properties of Cement Paste with Ultra-Low Water Binder Ratio," *Materials,* vol. 15, no. 2, p. 554, 2022.

[67] D. Jiao, C. Shi, Q. Yuan, X. An, Y. Liu, and H. Li, "Effect of constituents on rheological properties of fresh concrete-A review," *Cement and concrete composites,* vol. 83, pp. 146-159, 2017.

[68] M. Rubio, M. Sonebi, and S. Amziane, "3D printing of fibre cement-based materials: fresh and rheological performances," *Academic Journal of Civil Engineering,* vol. 35, no. 2, pp. 480-488, 2017.

[69] R. S. Ahari, T. K. Erdem, and K. Ramyar, "Thixotropy and structural breakdown properties of self consolidating concrete containing various supplementary cementitious materials," *Cement and Concrete Composites,* vol. 59, pp. 26-37, 2015.

[70] R. S. Ahari, T. K. Erdem, and K. Ramyar, "Effect of various supplementary cementitious materials on rheological properties of self-consolidating concrete," *Construction and Building Materials,* vol. 75, pp. 89-98, 2015.

[71] B. Zhu, J. Pan, B. Nematollahi, Z. Zhou, Y. Zhang, and J. Sanjayan, "Development of 3D printable engineered cementitious composites with ultra-high tensile ductility for digital construction," *Materials & Design,* vol. 181, p. 108088, 2019.

[72] H. Ogura, V. N. Nerella, and V. Mechtcherine, "Developing and testing of strain-hardening cement-based composites (SHCC) in the context of 3D-printing," *Materials,* vol. 11, no. 8, p. 1375, 2018.

[73] Y. Bao *et al.*, "Three-dimensional printing multifunctional engineered cementitious composites (ECC) for structural elements," in *RILEM International Conference on Concrete and Digital Fabrication*, 2018: Springer, pp. 115-128.

[74] W. Zhou, Y. Zhang, L. Ma, and V. C. Li, "Influence of printing parameters on 3D printing engineered cementitious composites (3DP-ECC)," *Cement and Concrete Composites,* vol. 130, p. 104562, 2022.

[75] B. Felekoglu, K. Tosun-Felekoglu, R. Ranade, Q. Zhang, and V. C. Li, "Influence of matrix flowability, fiber mixing procedure, and curing conditions on the mechanical performance of HTPP-ECC," *Composites Part B: Engineering,* vol. 60, pp. 359-370, 2014.

[76] M. Li and V. C. Li, "Rheology, fiber dispersion, and robust properties of engineered cementitious composites," *Materials and structures,* vol. 46, no. 3, pp. 405-420, 2013.

[77] B. Panda, S. C. Paul, and M. J. Tan, "Anisotropic mechanical performance of 3D printed fiber reinforced sustainable construction material," *Materials Letters,* vol. 209, pp. 146-149, 2017.

[78] S. Chaves Figueiredo *et al.*, "Mechanical behavior of printed strain hardening cementitious composites," *Materials,* vol. 13, no. 10, p. 2253, 2020.

[79] W. McGee, T. Y. Ng, K. Yu, and V. C. Li, "Extrusion nozzle shaping for improved 3DP of engineered cementitious composites (ECC/SHCC)," in *RILEM International Conference on Concrete and Digital Fabrication*, 2020: Springer, pp. 916-925.

[80] B. Panda, S. C. Paul, N. A. N. Mohamed, Y. W. D. Tay, and M. J. Tan, "Measurement of tensile bond strength of 3D printed geopolymer mortar," *Measurement,* vol. 113, pp. 108-116, 2018.

[81] B. Panda, N. A. Noor Mohamed, S. C. Paul, G. Bhagath Singh, M. J. Tan, and B. Šavija, "The effect of material fresh properties and process parameters on buildability and interlayer adhesion of 3D printed concrete," *Materials,* vol. 12, no. 13, p. 2149, 2019.

[82] T. C. Triantafillou, "Shear strengthening of reinforced concrete beams using epoxy-bonded FRP composites," *ACI structural journal,* vol. 95, pp. 107-115, 1998.

[83] M. Leone, S. Matthys, and M. A. Aiello, "Effect of elevated service temperature on bond between FRP EBR systems and concrete," *Composites Part B: Engineering,* vol. 40, no. 1, pp. 85-93, 2009.

[84] H. A. Toutanji and W. Gomez, "Durability characteristics of concrete beams externally bonded with FRP composite sheets," *Cement and Concrete Composites,* vol. 19, no. 4, pp. 351-358, 1997.

[85] A. Belarbi and B. Acun, "FRP systems in shear strengthening of reinforced concrete structures," *Procedia Engineering,* vol. 57, pp. 2-8, 2013.

[86] Y. Zhang, S. Bai, and Q. Zhang, "Investigation of localised behaviour of strain-hardening cementitious composites for RC strengthening," *Advances in Cement Research,* vol. 28, no. 6, pp. 414-421, 2016.

[87] H. Li, C. K. Leung, S. Xu, and Q. Cao, "Potential use of strain hardening ECC in permanent formwork with small scale flexural beams," *Journal of Wuhan University of Technology-Mater. Sci. Ed.,* vol. 24, no. 3, pp. 482-487, 2009.

[88] Z. Qiao, Z. Pan, W. Xue, and S. Meng, "Experimental study on flexural behavior of ECC/RC composite beams with U-shaped ECC permanent formwork," *Frontiers of Structural and Civil Engineering,* vol. 13, no. 5, pp. 1271-1287, 2019.

[89] C. K. Leung and Q. Cao, "Development of pseudo-ductile permanent formwork for durable concrete structures," *Materials and Structures,* vol. 43, no. 7, pp. 993-1007, 2010.

[90] P. Duxson, J. L. Provis, G. C. Lukey, and J. S. Van Deventer, "The role of inorganic polymer technology in the development of 'green concrete'," *cement and concrete research,* vol. 37, no. 12, pp. 1590-1597, 2007.

[91] *NEN-EN 12390-3*, NEN, Delft, 2019.

[92] *NEN-EN 206+NEN 8005:2017 nl*, NEN, Delft, 2017.

[93] *NEN-EN 12390-13*, NEN, Delft, 2021.

[94] S. He, S. Zhang, M. Luković, and E. Schlangen, "Effects of bacteria-embedded polylactic acid (PLA) capsules on fracture properties of strain hardening cementitious composite (SHCC)," *Engineering Fracture Mechanics,* vol. 268, p. 108480, 2022.

[95] *C1437 − 20* ASTM, West Conshohocken, 2020.

[96] N.-E. 196-1, "Beproevingsmethoden voor cement - Deel 1: Bepaling van de sterkte," 2016.

[97] B. Budnik, "Shear capacity of innovative hybrid concrete structures with SHCC lamellas applied laterally," 2023.

[98] M. George, D. Sathyan, and K. Mini, "Investigations on effect of different fibers on the properties of engineered cementitious composites," *Materials Today: Proceedings,* vol. 42, pp. 1417-1421, 2021.

[99] Y. Wang, F. Liu, J. Yu, F. Dong, and J. Ye, "Effect of polyethylene fiber content on physical and mechanical properties of engineered cementitious composites," *Construction and Building Materials,* vol. 251, p. 118917, 2020.

[100] O. M. Elbasir, A. Araba, M. B. Miskeen, S. Nser, and N. Fathi, "Effect of Addition Silica Fume to the workability, Strength and Permeability of Concrete," *Journal of Pure & Applied Sciences,* vol. 18, no. 4, 2019.

[101] S. Barbhuiya and M. Qureshi, "Effects of silica fume on the strength and durability properties of concrete," *Age,* vol. 3, no. 7, p. 28, 2016.

[102] A. Hassan, K. Hossain, and M. Lachemi, "Strength, cracking and deflection performance of large-scale self-consolidating concrete beams subjected to shear failure," *Engineering Structures,* vol. 32, no. 5, pp. 1262-1271, 2010.

[103] K. Hossain, S. Hasib, and T. Manzur, "Shear behavior of novel hybrid composite beams made of self-consolidating concrete and engineered cementitious composites," *Engineering Structures,* vol. 202, p. 109856, 2020.

[104] H. Dulacska, "Dowel action of reinforcement crossing cracks in concrete," in *Journal Proceedings*, 1972, vol. 69, no. 12, pp. 754-757.

[105] A. Committee, "Building code requirements for structural concrete (ACI 318-08) and commentary," 2008: American Concrete Institute.

[106] *Methods of test for mortar for masonry - Part 11:*

Determination of flexural and compressive

strength of hardened mortar E. 1015-11, 2019.

[107] Y. Ding, K. Yu, and W. Mao, "Compressive performance of all-grade engineered cementitious composites: Experiment and theoretical model," *Construction and Building Materials,* vol. 244, p. 118357, 2020.

[108] *NEN-EN 12390-2*, NEN, Delft, 2019.